1400

Thomas Hessler

Continuous-Relief Diffractive Optical Elements:

Design, Fabrication and Applications

Université de Neuchâtel
Institut de Microtechnique

Continuous-Relief Diffractive Optical Elements: Design, Fabrication, and Applications

Thèse

Présentée à la Faculté des sciences
pour obtenir le grade docteur ès sciences
par

Thomas Hessler

Neuchâtel, décembre 1997

IMPRIMATUR POUR LA THÈSE

Continuous-Relief Diffractive Optical Elements: Design, Fabrication and Applications

de M. Thomas Hessler

UNIVERSITÉ DE NEUCHÂTEL

FACULTÉ DES SCIENCES

La Faculté des sciences de l'Université de Neuchâtel sur le rapport des membres du jury,

MM. R. Dändliker (directeur de thèse),
H.-P. Herzig, M. Rossi (CSEM, Zürich) et
H . Tiziani (Uni. Stuttgart)

autorise l'impression de la présente thèse.

Neuchâtel, le 27 janvier 1998

Le doyen:

F. Stoeckli

Abstract

In this thesis we investigate new design- and optimization methods for diffractive optical elements (DOEs) with continuous-relief structures fabricated by direct laser beam writing and subsequent replication into polymer materials.

A fast and accurate method is developed for the surface relief calculation of DOEs with large deflection angles (6° - 30°). The influence of the fabrication tolerances and the limitations on the optical performance are analyzed and quantitatively related to the diffraction efficiency. For lenses with low Fresnel numbers, relaxed tolerances were observed. Using robust optimization methods we could double the resolution of the laser beam writing technology.

Optical systems can profit enormously from the implementation of micro-optical and diffractive optical elements. This is demonstrated for applications in metrology, wavefront sensing and optics in computing. Taking full advantage of the flexibility of direct laser beam writing, we demonstrate lens arrays with a spatially variation of the optical function. They offer a new field of applications in optical interconnects and imaging on non-planar surfaces.

List of Publications

This thesis is an overview of the author's work in the field of diffractive optical elements. The thesis includes the following selection of the author's publications in this field.

I Th. Hessler and R.E. Kunz, *"Relaxed fabrication tolerances for low Fresnel number lenses,"* J. Opt. Soc. Am. A **14**, 1599-1606 (1997).

II Th. Hessler, M. Rossi, R. E. Kunz, and M. T. Gale, *"Analysis and optimization of fabrication of continuous-relief diffractive optical elements,"* submitted to Applied Optics.

III H.J. Tiziani, R. Achi and R.N. Krämer; Th. Hessler, M.T. Gale, M. Rossi and R.E. Kunz *"Microlens arrays for confocal microscopy"* Optics & Laser Technology 29, 85-91 (1997).

IV Th. Hessler, M. Rossi, J. Pedersen, M.T. Gale, M. Wegner, D. Steudle and H.J. Tiziani, *"Microlens arrays with spatial variation of the optical functions"*, JEOS A, Pure & Appl. Opt. **6**, 673-681 (1997).

Throughout the overview, these papers will be referred to by Roman numerals.

Contents

1. Introduction

The development of small optoelectronic components such as semiconductor lasers or detector arrays imposes the wish to combine these new devices with optical components on the same scale.
The conventional optical fabrication techniques like grinding and polishing are no longer applicable for elements with sizes in the sub-millimeter range. Over the last years, several fabrication methods for micro-optical elements have been developed [e.g. Gal 97, Ste 97]. They are often based on a lithographic process and are - up to a certain degree - compatible with the fabrication technologies for optoelectronic devices. With these new technologies, refractive lenses can not only be fabricated with aperture sizes down to a few micrometers, they can also be aligned with sub-micron accuracy and they can be combined to form arrays of identical elements [NPL]. The applications of such microlens arrays are numerous. With its high level of parallelism, lens arrays are the basis for optical interconnects or optical metrology systems like Shack-Hartmann wavefront sensors [Yoo 96] or parallel scanning confocal microscopy [Tiz 94]. Lens arrays are also used to enhance the performance of optoelectronic smart pixel arrays by collecting the incident light on the photosensitive area. In combination with a pinhole array, microlens arrays can be used to restrict the viewing angle in projection displays or anti-counterfeiting devices.

In addition to the miniaturization of classical optical elements, also the manufacturing of diffractive optical elements (DOEs) as a new type of optical elements became possible. Typically they are realized as thin surface relief phase-only elements. These micro-structured surfaces change the phase of an incident wave by the variation of the optical path length across the element. DOE's offer high diffraction efficiency and are suitable for low cost replication into polymer materials. Geometrical optics, the language of classical optical elements assuming the wavelength of light to be infinitely small is not adequate for the DOE description. The choice of the theory to be used for the DOE design and the DOE analysis depends on the feature size. Rigorous solutions of Maxwell's equation are needed for DOEs with features in the order of the wavelength of light; for DOEs with larger features approximate methods neglecting the vector character of can be used.

The use of DOEs helps the optical designer to access optical functions which are impossible or difficult to realize with classical optical elements. Typical functions include the focusing, splitting and shaping of light. These different functions can also be combined in one single element. Beam shaping applications include the transformation of a Gaussian intensity distribution into a flattop distribution or into image plane distributions with a given geometrical shape such as circles or lines. DOEs can correct for wavefront distortions in optical systems. An application of this kind is their use in laser cavities to act as mode filter or to correct for thermal induced aberrations in high power solid state laser systems [Leg 97]. Since the DOE performance is based on the wave nature of light, DOEs behave very different and often more sensitive to changes in the illumination conditions compared to refractive optical elements. This special feature of DOEs is used for the correction of chromatic aberrations in hybrid diffractive/refractive elements.

Most applications of DOE's require a high diffraction efficiency combined with a surface relief whose feature size can be at the limit of the fabrication technology. Therefore, efficient design tools and advanced fabrication techniques are needed for a successfully implementation of DOEs into applications.

In this thesis we investigate new design and optimization methods for DOEs with continuous-relief structures fabricated by direct write methods, taking specific fabrication tolerances and fabrication limitations into account. With direct write methods and especially with direct laser beam writing, a wide range of optical elements is accessible. Using the same technology, small refractive lenses and diffractive lenses with low (0.003) and high numerical apertures (< 0.5) are fabricated. The aperture shape of individual elements can be chosen nearly arbitrary, lens arrays are realized with practically zero dead space between the lenslets and the optical function can vary from lens to lens.

The thesis is organized as follows: Chapter 2 treats the design and the theoretical analysis of continuous-relief diffractive optical elements. A new approach for the surface relief calculation for DOEs with high deflection angles (6° - 30°) is presented. It combines the simplicity of an existing model with the accuracy of solutions based on iterative phase-sensitive ray tracing calculations [Ros 93]. The refractive and diffractive properties of lenses with low Fresnel numbers and of lenses with a deep surface relief structure are investigated in a theoretical analysis.

Direct laser beam writing in photoresist and the subsequent replication into polymer material, are summarized in the first part of Chapter 3. The influence of the tolerances and limitations of direct laser beam writing on the optical performance of DOEs is analyzed in the second part of Chapter 3.

This knowledge is used in Chapter 4 to optimize the surface profile of a given DOE to obtain a maximum of diffraction efficiency while keeping the fabrication tolerances relaxed.

In the final chapter, Chapter 5, we demonstrate how applications in the fields of microscopy, wavefront sensing, and information technology profit from the implementation of diffractive optical elements as single elements or arranged in arrays. We use our new approach for the surface relief calculation from Chapter 2 and take advantage of the flexibility of direct laser beam writing to realize a novel kind of lens array where every lens can have a different optical function.

2. Design and analysis of continuous-relief diffractive optical elements

This chapter contains the theoretical part of this thesis. It deals with the design, modeling, and analysis of continuous-relief diffractive optical elements. The design is separated into three steps. In the first step (Sec. 2.1), we calculate a phase function which defines the optical function of the diffractive optical element. In the second step, the phase function is wrapped in intervals of multiples of 2π to form the diffractive phase function. The solution for the diffractive phase function is not unique and leaves room for free design parameters. They are presented in Section 2.2. In the third step, the diffractive phase function is transformed into a surface relief, the diffractive optical element (Sec. 2.3). This can be done either in a very simple manner (Sec. 2.3.1) or in a more sophisticated way (Sec. 2.3.2 and Sec. 2.3.3). The modeling of diffractive optical elements (DOEs) based on a combined theory of phase-sensitive ray tracing and free space propagation is presented in Section 2.4. Finally, we investigate the refractive and diffractive properties of continuous-relief optical elements in Section 2.5.

The diffractive optical element design is illustrated at the example of a lens. However, the results can also be applied to most other optical elements. For the phase function calculation of other DOEs, such as transmissive [e.g. Han 83] or reflective diffractive beam shaping elements [Hes 95, Tsc 95], or computer generated holograms [e.g. Lee 78] we refer to the literature.

2.1 Phase function calculation

A DOE transforms an incident wave ϕ_{in} into an output wave ϕ_{out} [Her 97] by adding a locally varying phase shift $\phi(x,y)$:

$$\phi_{out}(x,y) = \phi_{in}(x,y) + \phi(x,y). \qquad (2.1)$$

In general, ϕ depends on the x and y coordinate which is reduced to a one-dimensional radial dependence with $r = \sqrt{x^2 + y^2}$ for circular symmetrical elements. In the case of a diffractive lens with plane wave illumination, the phase function can be derived in analytical form and is given by [Bur 89]:

$$\phi(r) = -2\pi \frac{\sqrt{r^2 + f^2} - f}{\lambda_0}, \tag{2.2}$$

where f is the focal length and λ_0 the design wavelength. This reduces in the paraxial approximation ($f >> r$) [Goo 96] to the parabolic form:

$$\phi(r) = -\pi \frac{r^2}{\lambda_0 f}. \tag{2.3}$$

For lenses with F-numbers less than $F/10$ ($F/\# = f/D$, D = lens aperture), a design without using the paraxial approximation is required in order to obtain DOEs with small aberrations [Bur 89]. In contrast to the classical fabrication methods of bulk refractive, spherical lenses, nearly any arbitrary surface relief can be generated (within the fabrication system resolution) with modern micro-machining fabrication methods. A non-paraxial design does not complicate the fabrication. However, for more complicated DOEs than simple lenses, the phase function calculation can be considerably simplified by using the paraxial approximation. If not explicitly stated otherwise, throughout the following a non-paraxial lens design is used.

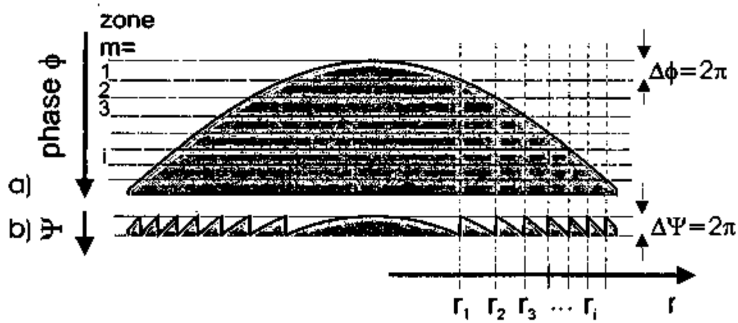

Fig. 2.1: Construction of the wrapped phase function. The phase profile is cut into slices of 2π (a). The resulting segmented phase is shown in b).

Since we are interested in a thin optical element, we take advantage of the 2π ambiguity of the optical phase and wrap the phase function ϕ into slices of 2π (cf. Fig. 2.1) and obtain the diffractive phase function Ψ:

$$\Psi(r) = \phi(r) \bmod (2\pi). \tag{2.4}$$

The radial position of the m-th zone boundary is given by [e.g. Nis 87]

$$r_m = \sqrt{2m\lambda f + m^2 {\lambda_0}^2}\,. \tag{2.5}$$

In the paraxial approximation, Eq. 2.4 is reduced to

$$r_{m_{paraxial}} = \sqrt{2m\lambda_0 f}\,. \tag{2.6}$$

The design of a diffractive lens can be seen in the principle of holography. The lateral pattern of the wrapped phase function as given by Eq. 2.4 is the same as the interference pattern of a spherical wave with a plane wave.

2.2 Design freedoms

Before we transform the phase function into a surface relief, we discuss additional design freedoms for the calculation of the DOE wrapped phase function Ψ. Using these design freedoms results in different diffractive phase functions Ψ and finally in different surface profiles. Under ideal conditions, elements based on these different phase functions will show an identical optical behavior within the validity of the scalar theory. However, under real conditions, differences in their performance will appear. Non-ideal conditions include the illumination with a wavelength $\lambda \neq \lambda_0$ and deviations of the fabricated profile from the desired shape. These design freedoms are used to optimize the DOE surface relief with respect to specific applications or fabrication parameters (c.f. Sec. 4.1).

2.2.1 Phase-matching number

Since the optical phases are only defined modulo 2π, the phase function ϕ can also be wrapped in slices of multiples of 2π:

$$\Psi(r) = \phi(r) \bmod (M_m 2\pi) \tag{2.4a}$$

The thickness of the m-th slice (cf. Fig. 2.1) is $M_m 2\pi$, the positive integer M_m is referred to as the phase-matching number [Kun 93]. This phase-matching number M_m can vary from zone to zone or have a constant value for the whole element ($M = M_m$). If M_m is constant over a few zones, it is the diffraction order this part of the element is designed to work in [Fut 92, Fak 95, Mar 90].

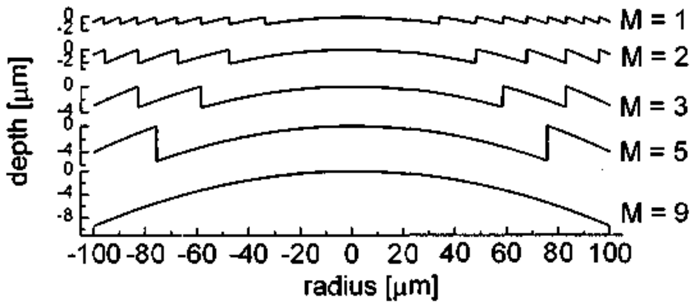

Fig. 2.2: Surface profile of lenses based on phase function with increasing phase-matching number *M*.

Fig. 2.2 shows the surface relief profile of lenses with a constant phase-matching number *M* for different values of $M = 1...9$. A higher *M* reduces the total number of zones, the remaining zones are wider and deeper. The phase-matching number *M* is a very powerful design parameter. It is used to tune the refractive/diffractive properties of the optical elements (Sec. 2.5) and to optimize the surface relief for the element fabrication (Sec. 4.1). Further, it is used to design diffractive lenses with a modified chromatic behavior [Fak 95].

2.2.2 Constant phase offset

The position of the zones can be laterally shifted (see Fig. 2.3) by adding a constant phase term φ_0 to the phase function ϕ before wrapping it [Ehb 95]:

$$\Psi(r) = \left[\phi(r) + \varphi_0\right] \bmod \left(M_m\, 2\pi\right). \tag{2.4b}$$

Fig. 2.3 shows the resulting surface relief for a lens with a varying phase offset. The local curvature of the phase is not altered by this "breathing" of the wrapped phase function. We demonstrated the use of this design freedom to increase the diffractive behavior for low Fresnel number lenses (Sec. 2.4 and Pub. I) and to reduce effects arising from the fabrication process (Sec. 4.1 and Pub. II). We find that the influence of adding a phase offset is especially pronounced for lenses with a small number of zones. Thus, it is of special interest for the design of microlens arrays, as they often only have few zones due to their small aperture.

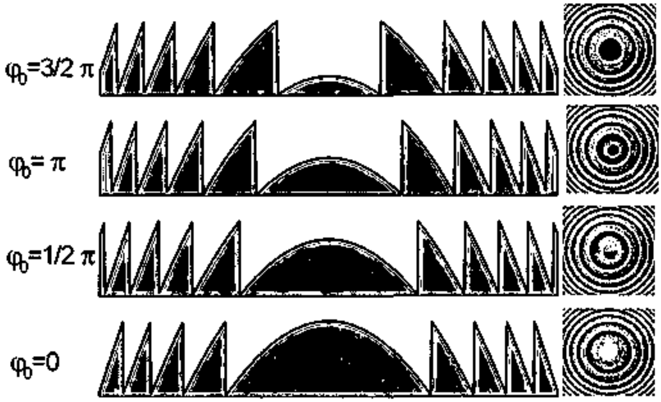

Fig. 2.3: Phase offset φ_0 as design freedom, illustrated for a lens with $M = 1$, $N_F = 10$ and $NA = 0.16$.

2.2.3 Zone position and size

We can also change the size and the position of the segments [Hes 97]. In fact, when wrapping the phase function (Eq. 2.4) the only constraint is to keep the phase difference between two neighboring segments to a multiple of 2π. The phase difference for a thicker or thinner slice can be compensated by lifting or lowering the phase profile. We rewrite Eq. 2.4b to:

$$\Psi(r) = \left[\phi(r) + \varphi_m + \varphi_0\right] \bmod \left(M_m\, 2\pi\right) - \varphi_m, \qquad (2.4c)$$

where we introduced φ_m as the phase offset for the m-th zone. It can be varied from segment to segment independently and is subtracted after the wrapping to retain constructive interference between rays emanating from different segments. As a result, the size and the lateral position of the segments are changed. This is shown in Fig. 2.4 for a diffractive lens.

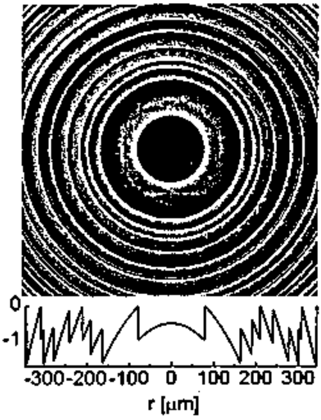

Fig. 2.4: Diffractive lens with arbitrary zone positioning.

The φ_m are randomly distributed within a reasonable interval and the regular pattern of the diffractive lens disappears. However, we still have the optical function of a *normal* diffractive lens under design conditions. The situation changes for non-design conditions, such as for illumination with a different wavelength. The main diffraction order shows still the same chromatic behavior as a normal diffractive lens. However, the remaining light is broadly distributed, additional unwanted diffraction orders are not well defined as it is the case for a normal diffractive lens (cf. Sec. 4.1).

2.3 Surface relief calculation

In the third step of our design process, we have to structure a dielectric material in a way that it produces the desired phase delay ϕ. This is done by transforming the wrapped phase function $\Psi(r)$ into a surface relief $h(r)$. We discuss three different approaches to perform this transformation.

2.3.1 Thin layer approximation

The standard approach [Nis 87, Her 97] for the transformation of the wrapped phase $\Psi(x,y)$ into a surface relief $h(r)$ is to multiply $\Psi(r)$ by a constant depth d_{TL}:

$$h(r) = d_{TL} \frac{\Psi(r)}{M\,2\pi}. \tag{2.7}$$

The depth d_{TL} is given by:

$$d_{TL} = \frac{M\,\lambda_0}{n_1 - n_0}, \tag{2.8}$$

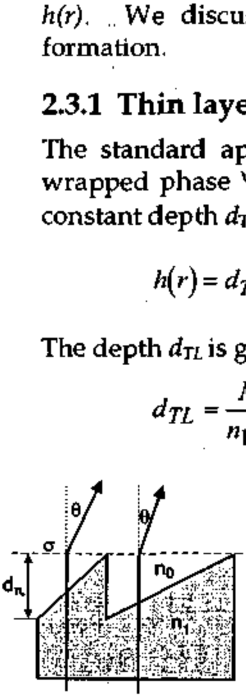

Fig. TL: In the thin layer approximation the rays are deflected in the tangential plane σ.

and is the distance corresponding to a phase delay of $M2\pi$ for light of the design wavelength λ_0. The refractive indices of the substrate and ambient medium are denoted by n_1 and n_0, respectively.

For the transformation given by Eq. 2.7, we made the assumption that the rays are traveling vertically though the structured layer (cf. Fig. 2.5). In other words, we assumed that the phase delay occurs in an infinitely thin layer [Mag 78] (thin layer approximation). This approximation is justified for small deflection angles θ or for materials with very high refractive indices. First introduced by Sweatt [Swe 77], it allows to model DOEs in standard ray tracing programs. A great advantage of the thin layer approximation is its simplicity in terms of computational effort.

2.3.2 Phase-sensitive ray tracing

If we use a ray tracing picture, we expect the rays to be refracted at the local interface. This is the basis for a more accurate way to calculate the surface relief.

Employing phase-sensitive ray tracing, we use Fermat's principle [Bor 80] to calculate the surface relief such that the optical path length fulfills the design requirements given by the wrapped phase function $\Psi(x,y)$ [Bur 89, Ros 95a]. The surface relief is adjusted on a microscopic level in a iterative way. In this approach, geometrical optical principles are employed with the use of rays defined as surface normals of the traveling waves; physical or wave optics is accounted for by taking the phase into account. The main difference to the thin layer approximation is, that the propagation of the rays within the structured layer is considered. As a typical result of the propagation of the rays in the structured layer, the surface profile for a diffractive lens becomes shallower towards the aperture edge.

For large deflection angles, the feature sizes become smaller. A design based on a rigorous diffraction theory would be needed [Nop 93, Fin 95]. However, such solutions require a large computational effort if they are available at all. For simple structures such as blazed gratings, it can been shown that the optimum depth becomes shallower for larger deflection angles.

2.3.3 Direct transformation

The phase-sensitive ray trace approach is very accurate but the solution for the surface relief needs to be calculated in an iterative algorithm. We combine the simplicity of the thin layer approximation with the accuracy of the phase-sensitive ray trace approach. This results in the *direct transformation,* a fast and accurate method for the surface relief calculation.

First, we present an analytical description for the transformation of the phase function into a surface relief which is equivalent to the numerical phase-sensitive ray trace approach. Making a small approximation, we obtain the direct transformation. The solution still accounts for the propagation of the rays in the structured layer but it is simpler to calculate. We demonstrate this approach for an incident plane wave, but the results can be extended for an arbitrary incident wave.

For simplicity, we consider a radially symmetrical phase function. The normal vectors of the phase function $\Psi(r)$ point in the direction in which the incident rays are deflected. A local deflection angle $\theta(r)$ for the rays is calculated from the phase function Ψ by:

$$\theta(r) = \arcsin\left(\frac{\lambda_0}{2\pi}\nabla\Psi(r)\right). \tag{2.9}$$

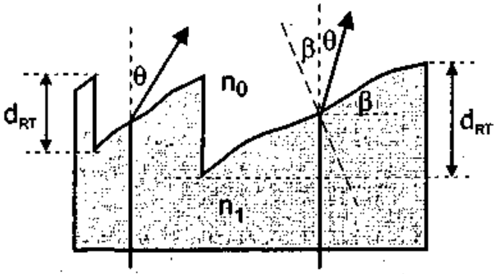

Fig. 2.6: Snell refraction at the local interface of DOE surface relief with varying blaze angle.

The underlying assumption for the surface relief calculation is that the rays are *refracted* at the local interface into the directions $\theta(r)$ required by the phase function Ψ (cf. Eq. 2.9) as indicated in Figure 2.6. The local blaze angle β is related to the deflection angle θ by Snell's law of refraction:

$$n_1 \sin(\beta) = n_0 \sin(\beta + \theta), \tag{2.10}$$

and by rewriting Eq. 2.10 it is given by:

$$\beta(r) = \arctan\left(\frac{n_0 \sin(\theta(r))}{n_1 - n_0 \cos(\theta(r))}\right). \tag{2.11}$$

The surface profile $h(r)$ in the m-th zone is obtained by integrating the local blaze angle $\beta(r)$ along the radius:

$$h(r) = \int_{r_{m-1}}^{r} \tan(\beta(r'))\, dr' = \int_{r_{m-1}}^{r} \frac{n_0 \frac{\lambda_0}{2\pi}\nabla\Psi(r')}{n_1 - n_0\cos(\theta(r'))}\, dr'. \tag{2.12}$$

We used Eq. 2.9 to replace the $\sin(\theta)$ term in Eq. 2.11. The lower bound of the integral r_m is the zone radius for arbitrary phase-matching number M and is for $\varphi_0 = 0$ given by:

$$r_m = \sqrt{2mM\lambda_0 f + (mM\lambda_0)^2}\,. \tag{2.13}$$

The surface profile described by Eq. 2.12 is equivalent to the numerical ray tracing approach. For the evaluation of Eq. 2.12 the integration has to be performed and the lower integration bound has to be determined.

We are interested in a direct local transformation of Ψ into $h(r)$ without the necessity to calculate the surface relief at positions $r' \neq r$. For small $\nabla\theta$ and $n_1 > n_0$ we make the following approximation in the integral of Eq. 2.12:

$$h(r) \approx \frac{n_0 \frac{\lambda_0}{2\pi}}{n_1 - n_0 \cos(\theta(r))} \int_{r_{m-1}}^{r} \nabla\Psi(r')\,dr'\,. \tag{2.14}$$

We neglected the variation of the deflection angle θ in the denominator for the integration. In other words, we calculate the values of the deflection angle θ in the tangential plane σ instead at the local interface.

The surface relief $h(r)$ is then obtained by integrating Eq. 2.14. Using the fact that the wrapped phase function Ψ is identical to zero at the zone boundaries, we obtain

$$h(r) = d_{DT}(r)\,\frac{\Psi(r)}{M\,2\pi}\,. \tag{2.15}$$

This result looks very similar to Eq. 2.7. The direct transformation (*DT*) depth d_{DT} is given by

$$d_{DT}(r) = \frac{M\,\lambda_0}{n_1 - n_0 \cos(\theta(r))}, \tag{2.16}$$

and corresponds to a phase delay of $M2\pi$. d_{DT} is a continuous function and may vary within one zone of the resulting surface structure (cf. Fig. 2.7). For small deflection angles ($\cos(\theta) \approx 1$), Eq. 2.16 is reduced to Eq. 2.8 and Eq. 2.15 is reduced to the thin layer approximation (Eq. 2.7).

With Eq. 2.15, we have a possibility of locally transforming the phase into a surface relief. This direct transformation can be applied directly for phase functions given in cartesian coordinates, simply by replacing ∇ with $\vec{\nabla} = (\nabla_x, \nabla_y)$ in Eq. 2.9. The transformation can be performed for the individual positions (x,y) in arbitrary order. The propagation of the rays within the structures layer is still accounted for by the dependence of d_{DT} on the deflection angle θ.

The error introduced through the approximation in Eq. 2.14 is very small and is only present for varying θ. In Fig. 2.7 we show the surface profile for a diffractive lens ($M = 8$, $f = 50$ μm) calculated with the three approaches, the "*exact*" phase-sensitive ray trace, the direct transformation and the thin layer approximation. As can be seen, the difference between the two ray tracing based techniques to the thin-layer approximation is significant, whereas the direct transformation is close to the exact ray tracing solution.

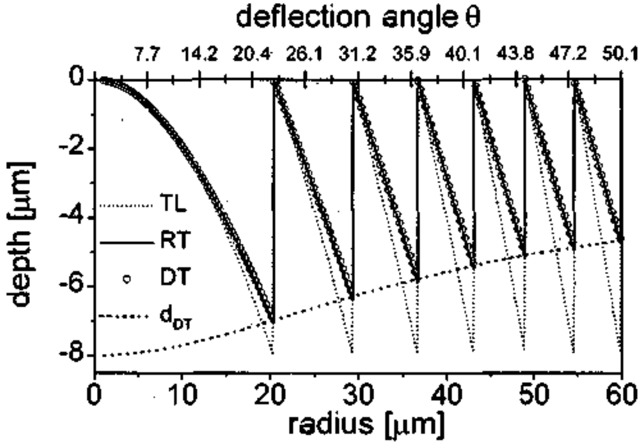

Fig. 2.7: Surface relief of a lens with ($M = 8$, $f = 50$ μm, $\lambda = 0.5$ μm) obtained by the thin layer (TL) approximation (dotted line), ray-tracing (RT) (solid line) and approximate direct transformation (DT) method (circles). The depth d_{DT} is shown as well.

This direct transformation technique was successfully applied for the work of Publication IV. We fabricated lens arrays consisting of individual lenses with high numerical apertures. The optical function (e.g. the focal length) changed from lens to lens. In the fabrication process, the surface relief and the exposure data had to be calculated at real time to avoid data files too large to be handled. With this direct transformation of the phase-function into a surface relief, an efficient data generation and thus the realization of these novel type of lens arrays was made possible.

For DOEs where the paraxial approximation ($\sin(\theta) \approx \theta$) for the phase function calculation is valid, the thin layer approximation ($\cos(\theta) \approx 1$) can be used for the relief structure calculation. The direct transformation technique is of interest especially for optical elements having large deflection angles and a phase function given in a form which allows the calculation of its gradient. This is fulfilled for phase functions which are given in an analytical form, e.g. as polynomial approximation or in the form of differential equations, e.g. as for certain types of beam shaping elements [Rho 80, Han 83].

The design procedure of the DOEs is complete with the surface relief calculation. In the next sections, we analyze theoretical limitations and refractive / diffractive properties of the DOEs.

2.4 Modeling of continuous-relief DOEs

The modeling of DOEs is of interest to test the optical design, the influence of external parameters such as temperature or wavelength change or the influences of deviations of the fabricated profiles from the desired shape. A modeling tool based only on pure phase-*insensitive* ray tracing is not sufficient since it can not account for diffraction effects or predict the diffraction efficiency. A possible approach to model DOEs is to calculate a complex phase distribution with the thin layer approximation and then employ a fast Fourier transformation to obtain the far-field diffraction pattern. This is often referred to as scalar theory. This approach breaks down for feature sizes below $20\,\lambda$ [Pom 94]. Calculations based on rigorous diffraction theory for complicated structures are very time consuming or are not yet available. To fill this gap, we use a combined method of phase-sensitive ray tracing and scalar free space propagation. Using Snell's refraction formula, a set of rays is traced through the structured layer. A complex amplitude distribution $u_1(x_\sigma, y_\sigma)$ is obtained in the tangential plane σ to the surface relief by calculating the optical path length of the rays. The near-field or far-field diffraction pattern of the DOE is obtained by evaluating the Rayleigh-Sommerfeld diffraction formulas numerically. The complex amplitude distribution $u_2(x,y)$ in the observation plane (x,y) is given by [Gas 78]:

$$u_2(x,y)=\int\int_{-\infty}^{\infty} u_1\left(x_\sigma,y_\sigma\right)\left(\frac{z_{12}}{i\lambda r_{12}^2}\right)\exp\left(ikr_{12}\right)dx_\sigma\, dy_\sigma\,. \tag{2.17}$$

Here z_{12} is the distance between the tangential plane σ and the observation plane and $r_{12}=\sqrt{{z_{12}}^2+\left(x-x_\sigma\right)^2+\left(y-y_\sigma\right)^2}$. This method is still based on a scalar diffraction theory, but it accounts for the propagation of the rays in the structured layer and is therefore also called extended scalar theory [Swa 91]. The concept is illustrated in Fig. 2.8, showing the wavefront at three different positions behind a lens (f = 400 µm, λ = 0.5µm and aperture radius a = 60 µm) having the wrong depth and rounded profile steps.

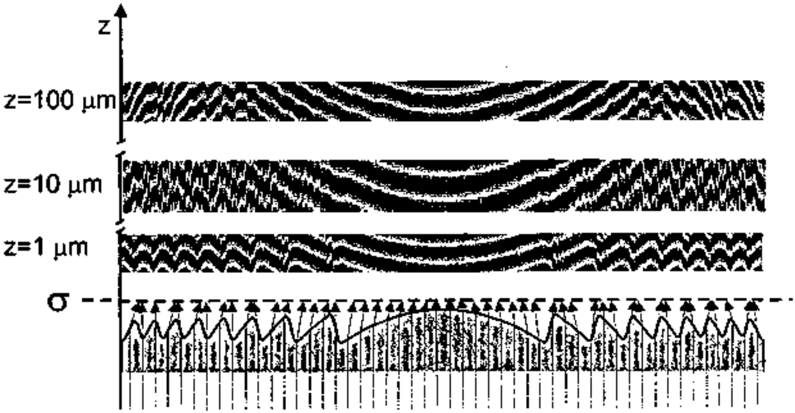

Fig. 2.8: Method of combined phase-sensitive ray tracing and free space propagation.

Diffraction efficiency calculations based on this model also show the decrease of diffraction efficiency for small periods as seen in rigorous calculations for blazed gratings [Nop 93]. Based on the phase-sensitive ray tracing approach, a simple qualitative model can be constructed to obtain an intuitive picture of the efficiency drop for small periods. Fig. 2.9 shows a set of rays traced through a blazed structure. The propagation of the rays in the structured layer leads to a so called "*shadow*" effect in the tangential plane. The resulting intensity modulation gives rise to diffraction during further propagation. In Pub. II a formula for the diffraction efficiency η_S is obtained (cf. Fig 2.9):

$$\eta_S = \left(\frac{\Lambda'}{\Lambda}\right) = \left(1 - \frac{\delta}{\Lambda}\right). \tag{2.18}$$

Eq. 2.18 is a simple relation that helps to estimate the theoretical limit of the diffraction efficiency for DOEs such as lenses with high numerical aperture (*NA*). A good agreement of this approach with rigorous calculations has been shown in [Ros 96].

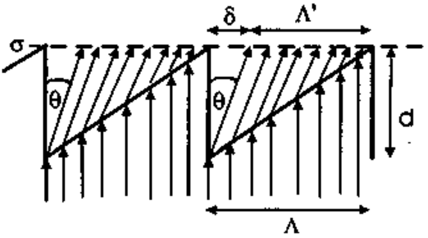

Fig. 2.9: Shadow effect for large deflection angles θ.

Effect of shadowing on optimum depth

The derivation of the optimum profile depth in Chapter 2.3.3 was based on the assumption that the refraction angle θ_r is equal to the deflection angle θ given by the phase function Ψ. However, the shadow effect influences the values of the optimum depth.

In the ray tracing picture, the shadowed region is given by $\delta = d\tan(\theta_r)$ where d is the depth of the structure. A depth $d < d_{RT}$ reduces the shadowed region and therefore the negative influence of the shadow effect on the diffraction efficiency [Kat 95]. However, for a depth $d < d_{RT}$, the blaze angle is no longer *correct*, the rays are deflected into directions $\theta_r \neq \theta$. This "*depth error*" will reduce the diffraction efficiency and counteract the gain obtained from the reduced shadow effect. In order to find the optimum depth, we rewrite Eq. 2.18 for the diffraction efficiency for a blazed grating with period Λ by including the dependence on the profile depth *d*.

$$\eta = \frac{\Lambda - d\tan(\theta_r)}{\Lambda}\operatorname{sinc}^2\left\{\frac{\Lambda - d\tan(\theta_r)}{\Lambda}\left(M - \frac{d}{d_{RT}}N\right)\right\}. \tag{2.19}$$

Eq. 2.19 reduces to Eq. 2.18 for $d = d_{RT}$. Note the additional implicit depth dependence of the refraction angle θ_r which is calculated with the blaze angle β:

$$\beta = \arctan\left(\frac{d}{\Lambda}\right) \tag{2.20}$$

and Snells law of refraction to:

$$\theta_r = \arcsin\left(\frac{n_1}{n_0}\sin(\beta)\right) - \beta\,. \tag{2.21}$$

The depth d which maximizes the diffraction efficiency according to Eq. 2.19 is calculated numerically and the result is shown in Fig. 2.10. Additionally, the depth d_{RT} is shown for comparison. As can be seen from the figure, the deviation of the optimum depth from d_{RT} is less significant for the higher phase-matching numbers. For $M = 1$, the additional gain in efficiency due to this depth correction is approximately 1/5 of the gain obtained in diffraction efficiency by using the direct transformation instead of the thin layer approximation. In practice, due to fabrication reasons (see Chapter 3 and Chapter 4), structures with small grating periods are preferably fabricated with higher phase-matching numbers. The above additional correction to the depth is then not critical and the direct transformation can be used.

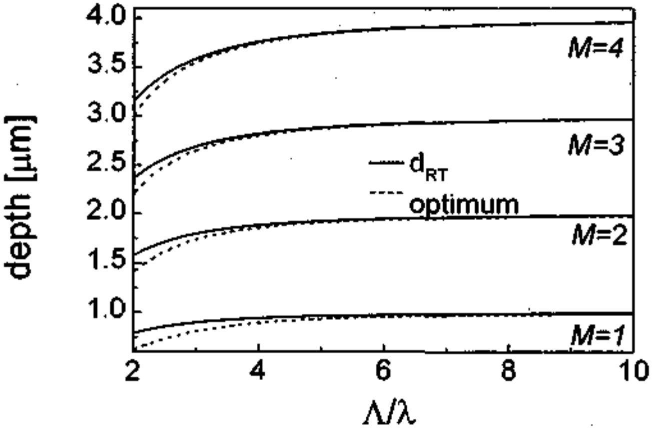

Fig. 2.10: Optimum depth for blazed gratings ($\lambda = 0.5$ µm, $n_0 = 1.0$, $n_1 = 1.5$) as function of the reduced grating period Λ/λ for different phase-matching numbers M.

2.5 Refractive / diffractive behavior

The optical behavior for purely refractive and purely diffractive lenses is well understood. A lens showing a purely refractive behavior has no profile steps and an aperture large enough that diffraction effects can be neglected. A lens with a purely diffractive behavior consists of a number of zones large enough to be considered as infinite and the phase delay occurs in a thin layer.

Lenses with low Fresnel numbers or lenses with deep relief structures [Ros 97] have surface profiles which cannot simply be put into one of these two categories.

In the following we investigate the requirements for a lens to show a behavior which can be classified as a purely refractive or purely diffractive and we will also outline the effects of the intermediate regime. This is of special interest for designs, where the peculiarities of refractive / diffractive lenses are used to counterbalance chromatic aberrations, thermal aberrations or to obtain a design which is robust against fabrication tolerances. The flexibility of some fabrication technologies such as direct laser beam writing often allows to fabricate the elements with enhanced refractive or diffractive properties [Ehb 95].

By considering the influence of shrinkage errors on the diffraction pattern of a blazed grating with a limited number of illuminated periods, the difference between its diffractive and refractive properties have recently been discussed by Herzig [Her 97]. Sinzinger and Testorf [Sin 95] investigated the chromatic behavior of a blazed grating with varying blaze depth in the limit of many illuminated segments using a Fourier-optics approach. They discussed the transition from a low order to a higher order blazed grating and found for higher orders an oscillating behavior of an overall refractive type. In numerical calculations, Rossi et. al. [Ros 95] found indications of an early onset of diffractive behavior when the number of illuminated zones is increased.

We investigate the influence of depth errors on lenses with a low Fresnel number which show strong aperture diffraction effects. The thermal properties for diffractive and refractive lenses are different in nature, the transition between a refractive and a diffractive behavior is investigated in Section 2.5.2. Finally, an intuitive picture based on Fourier optics is presented (Sec. 2.5.3).

2.5.1 Low Fresnel number lenses

Advances in fabrication technology [Völ 97, NPL] as well as new fields of applications such as smart masks for optical lithography [Völ 95] or Shack-Hartmann wavefront sensors [Art 92] lead to lenses usually arranged in an array where aperture diffraction effects cannot be neglected. A suitable parameter to describe the aperture diffraction effects is the Fresnel number N_F which is defined as [Li 84]:

$$N_F = \frac{a^2}{\lambda f}, \tag{2.22}$$

where f is the geometric optical focal length, λ the wavelength and a the lens aperture radius. It describes the maximum phase deviation from a plane wave in units of $\lambda/2$ over the aperture, i.e. N_F is twice the number of Fresnel zones for $M = 1$. Aperture diffraction effects become more important for smaller N_F. Typically, a low Fresnel number lenses have low NA. However, microlenses with an aperture as low as 3 µm have been fabricated recently [Völ 97], giving a low N_F even for very high numerical apertures.

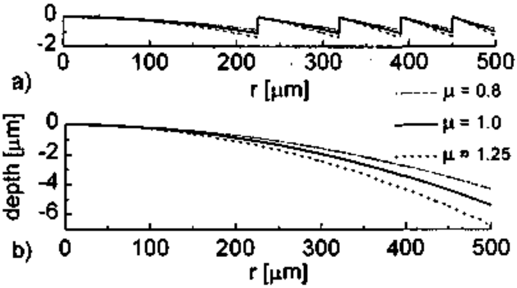

Fig. 2.11: Surface relief profile of the (a) diffractive and (b) refractive lens investigated (f_0 = 40 mm). The surface profile of the depth-scaled lenses (depth-scaling μ) is indicated by the dotted and dashed lines.

A field of applications for low Fresnel number lenses and the motivation for the work in Pub I is their use in lens arrays for Shack-Hartmann wave front sensing [Yoo 96]. These lenses typically have a small aperture (e.g. a = 125 - 250 µm) and a very low NA (e.g. NA = 0.01 - 0.003) at the same time. As for most microlens array applications, the incident intensity across one microlens aperture can be considered as constant. In Pub. I, we investigated the profile relief tolerances of coherently illuminated lenses having Fresnel numbers below 10 with respect to etching errors originating from the fabrication process (cf. Chapter 3). We compared lenses with a surface profile based on a wrapped phase function ($M = 1$) and lenses with a surface profile based on a non-wrapped phase function (cf. Fig. 2.11). We use the terms diffractive and refractive lens to distinguish these two types of lenses. In order to simulate the etching errors, we scaled the surface profile with a constant depth scaling factor μ. The surface relief for a diffractive and a refractive lens for $\mu = 0.8$, 1.0 and 1.25 is shown in Fig. 2.11.

Neglecting any aperture diffraction effects (large N_F), an etching error will change the radius of curvature for a refractive lens and thus the focal length in the paraxial approximation to [Pub I]:

$$\tilde{f} = {}^{f}\!/_{\mu}. \qquad (2.23)$$

For a first order diffractive lens with many segments illuminated ($N_F >> 1$), the focal length is not affected by the depth scaling, but additional foci will appear.

For low N_F, the aperture diffraction effects cannot be neglected any longer. For the non depth scaled lens ($\mu = 1.0$), the maximum of the on-axis intensity is found towards the aperture and no longer in the geometrical optical focal plane. This aperture diffraction effect is independent of the coding scheme used and is called focal shift [Li 81]. The on-axis diffraction pattern for a depth scaled paraxial refractive lens with Fresnel number N_F and a geometric optical focal length f_0 is derived in Pub. I to:

$$\tilde{I}(z,\mu) = \left(\frac{f_0\,\pi\,N_F}{z}\right)^2 \operatorname{sinc}^2\!\left(\frac{N_F}{2}\left(\frac{f_0}{z} - \mu\right)\right), \qquad (2.24)$$

with $\operatorname{sinc}(x) = \sin(\pi x)/(\pi x)$. The focal length f is defined as the value z for which the on-axis intensity has its maximum and is obtained numerically from Eq. 2.24. Fig. 2.12 shows the focal length f for the depth scaled refractive lens as a function of N_F.

For low Fresnel numbers, the focal length of the unscaled lens ($\mu = 1.0$) shows the focal shift and reaches the geometrical optical focal length f_0 for $N_F > 10$. For large N_F, the depth scaled lenses ($\mu \neq 1.0$) show the behavior expected by Eq. 2.23. For low N_F, the aperture diffraction starts to dominate, the focal length is no longer strongly affected by the depth scaling.

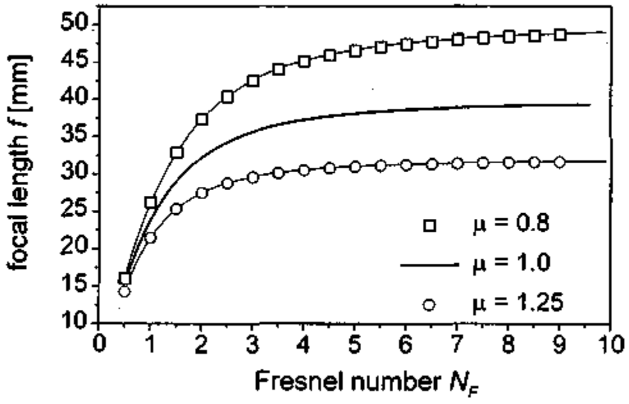

Fig. 2.12: Influence of depth scaling on the focal length for different Fresnel numbers (of the unscaled lens) for a refractive design (f_0 =40 mm).

This relaxed depth tolerance for low N_F is explained, as follows: The depth-scaled, refractive lens can be thought for $\mu < 1$ as being a lens with a longer geometric optical focal length (Eq. 2.23) leading to a smaller Fresnel number $\tilde{N}_F = \mu N_F$. This results in a larger focal shift which counterbalances the focal length change due to (Eq. 2.23). For $\mu > 1$, the opposite argument holds. The focal length of the depth-scaled refractive lenses for low Fresnel numbers is therefore stabilized by the focal shift due to the diffraction at the lens aperture.

The results for the diffractive lens are shown in Fig. 2.13. The diffractive lens shows the same behavior for $N_F \leq 2$, since the two lenses are then identical. With the illumination of the second segment ($N_F > 2$) the interference of the waves emanating from the different segments already stabilizes the focal length. The appearance of each additional segment results in a pronounced oscillation of the focal length in Fig. 2.13. For large N_F, the focal length is not affected by the depth errors. An analytical formula for the on-axis diffraction pattern for the diffractive lens is given in the last section.

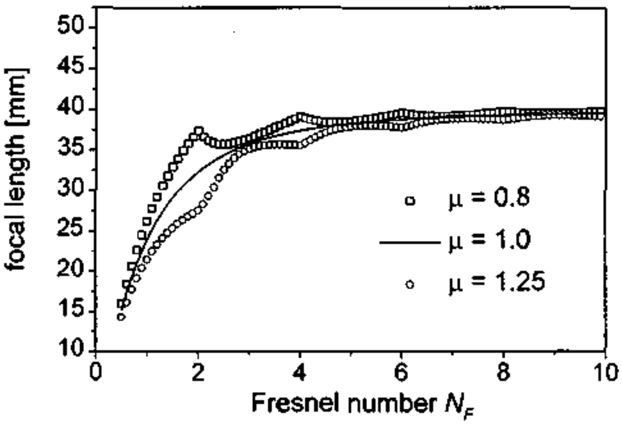

Fig. 2.13: Influence of depth-scaling on the focal length for different Fresnel numbers for a diffractive design.

2.5.2 Thermal behavior

An important property of diffractive lenses is their thermal behavior. It is characterized by the optothermal expansion coefficient χ [Jam 81]:

$$\chi = \frac{1}{f}\frac{df}{dT} \tag{2.25}$$

which is a measure for the relative change of the focal length f with temperature T. For a refractive lens, the focal length change is mainly due to changes of the refractive index n and due to the thermal expansion of the lens material which leads to an increase of the radius of curvature. The optothermal coefficient is given by [Jam 81]:

$$\chi_{f,r} = \alpha - \frac{1}{n-1}\frac{dn}{dT}, \tag{2.26}$$

where α is the linear thermal expansion coefficient. For polycarbonate, χ is given to $\chi_{f,r} = 250 \cdot 10^{-6}\,K^{-1}$.

For a diffractive lens, changes of the refractive index and profile height influence the diffraction efficiency but not the focal length f. The thermal expansion of the substrate material however changes the position of the Fresnel zones according to:

$$r_m(T) = (1 + \alpha\,\Delta T)\,r_m. \tag{2.27}$$

This leads to an optothermal expansion coefficient for a paraxial diffractive lens given by [Beh 93]:

$$\chi_{f,d} \approx 2\alpha\,, \tag{2.28}$$

and $\chi_{f,d} = 131\cdot 10^{-6}\,K^{-1}$ for a polycarbonate diffractive lens.

This principal difference in the optothermal expansion coefficient for refractive and diffractive lenses can be used to design athermal lenses by combining diffractive and refractive power appropriately [Beh 93]. The combined optothermal expansion coefficient χ of the hybrid:

$$\chi = \frac{f}{f_r}\chi_r + \frac{f}{f_d}\chi_d\,, \tag{2.29}$$

must vanish or it must compensate any other thermal expansions. f, f_r, and f_d are the focal length of the hybrid, the refractive and the diffractive part, respectively. For such a hybrid refractive / diffractive lens, the diffractive part was designed with a relatively large phase-matching number M for fabrication reasons. However, Eq. 2.28 is strictly valid only for a purely diffractive lens such as a binary zone plate.

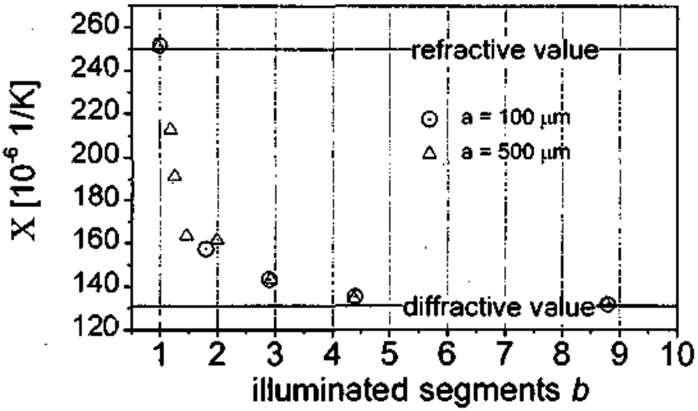

Fig. 2.14: Optothermal expansion coefficient as function of the number of illuminated segments *b*.

Therefore, we tested the validity of Eq. 2.28 for continuous-relief lenses with higher phase-matching numbers ($M > 1$). We simulated the thermal expansion of the surface relief in the radial and the z-direction and the

change of refractive index. The optothermal expansion coefficient was extracted from the temperature dependence of the diffraction pattern. The phase-matching number was increased from $M = 1$ to $M = 9$ (cf. Fig. 2.2), thus reducing the number of segments b, $b = N_F/2M$, from $b = 9$ to $b = 1$. This calculation was repeated with a set of lenses having the same NA but an aperture five times as big, resulting in $M = 1$ to $M = 45$.
Fig. 2.14 shows the optothermal expansion coefficient as a function of the number of segments illuminated.
Independent of the absolute value of the phase-matching number M, the transition from a refractive to a diffractive thermal behavior sets in with the illumination of the second segment. As a consequence, Eq. 2.28 can be used for the design of athermal hybrid lenses with higher phase-matching numbers as long as the diffractive structure consists of more than 5-10 illuminated segments.
Besides the changes of the lateral pattern, the thermal expansion of the diffractive structure in the vertical direction changes the profile height and can thus influence the diffraction efficiency. This change in depth can be described as a depth scaling μ which is given by $\mu = 1 + \alpha\,\Delta T$. For a thermal expansion coefficient as for polycarbonate ($\alpha = 65 \cdot 10^{-6}\, 1/K$) and a temperature range of $\Delta T = 50$ °C, the depth scaling is $\mu = 1.003$ and thus negligible compared to fabrication tolerances. Similar holds for the change in phase delay due to changes in the refractive index.

2.5.3 Fourier treatment

The onset of diffractive behavior with the illumination of the second zone can be understood in terms of interference of the two waves emanating from the two segments. In Pub. I an intuitive picture based on Fourier optics is given for blazed gratings and is then extended to cylindrical and circular diffractive lenses. It is here that we sketch the basics for the blazed grating and present the results for circular diffractive lenses to show the transition between diffractive and refractive behavior.
The transmission function of a partially illuminated blazed grating [Hut 82] can be expressed as:

$$t(x) = \left\{ \frac{1}{\Lambda} \mathrm{comb}\left(\frac{x}{\Lambda}\right) \otimes \left[\exp\left(i2\pi\mu \frac{x}{\Lambda} \right) \mathrm{rect}\left(\frac{x}{\Lambda}\right) \right] \right\} \mathrm{rect}\left(\frac{x}{b\Lambda}\right), \quad (2.30)$$

where Λ denotes the grating period, b the number of illuminated periods, μ the depth scaling factor and $\otimes$ stands for the convolution operation. The *comb* and *rect* functions are defined in [Gas 78]. The geometrical size of the illumination beam is taken into account by the last *rect* function.

We are interested in the intensity distribution in the Fourier plane. The Fourier transformation of the transmission function is [see Chap. 7 of Gas 78] evaluated to:

$$g(\nu) = b\Lambda^2 \underbrace{\operatorname{sinc}\left(\left(\nu - \frac{\mu}{\Lambda}\right)\Lambda\right)}_{g_{blaze}} \underbrace{\sum_{n=-\infty}^{\infty} \operatorname{sinc}\left(\left(\nu - \frac{n}{\Lambda}\right)b\Lambda\right)}_{g_{grat}}. \qquad (2.31)$$

The diffraction pattern is given by $I(\nu) = |g(\nu)|^2$. Its shape is determined by a laterally shifted *sinc* function (g_{blaze}), multiplied by g_{grat}. This factor g_{grat} consists of a series of *sinc* functions with finite widths determined by the number of illuminated segments b, each centered at a position given by the grating equation. The corresponding width w_g (cf. Fig. 2.15) of a peak in g_{grat} is a measure for the resolving power of the grating. For an infinite number of illuminated segments b, g_{grat} becomes the *comb* function.

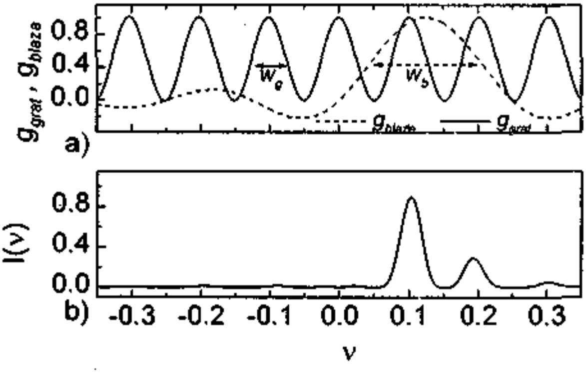

Fig. 2.15: (a) The grating and blaze contribution for $b = 2$ and a depth scaling of $\mu = 1.25$. The width w_g of the peaks is already much narrower than the width w_b of the envelope function g_{blaze}. (b) Precursors of the diffraction orders are already formed in the resulting angular intensity distribution $I(\nu)$, $\nu = \lambda / \Lambda$.

A depth error μ changes the blaze angle and therefore the refraction angle. This leads to a displacement of the g_{blaze} *sinc* function. Its width w_b is determined by the diffraction at one single segment and is therefore much wider than the width of the *sinc* functions forming g_{grat}. It acts as an envelope of the allowed angular spectrum. Fig. 2.15 shows the blaze and grating contributions (Fig. 2.15 a) and the resulting intensity (Fig. 2.15 b) for $b = 2$. As can be seen, already for two illuminated segments, w_g is much narrower than w_b. As a result, the intensity distribution shows "precursors" of the individual diffraction orders for $\mu \neq 1$. A depth error shifts the envelope and results in a non-vanishing intensity in the other orders. For low b the maxima of these precursors of the individual orders are not exactly at the position given by the grating equation, but they approach this value with increasing b and therefore decreasing w_g.

Formulas for the on-axis diffraction pattern of depth scaled cylindrical and circular diffractive lenses are derived in Pub I. The result for the circular lens of Pub I, Eq. 21, is here generalized to phase-matching numbers $M \geq 1$. The resulting on-axis intensity distribution is then given by:

$$I(z) = \left(\frac{f\pi\ N_F}{z}\right)^2 \underbrace{\mathrm{sinc}^2\left(\left(\frac{f}{z} - \mu\right)M\right)}_{g_{blaze}{}^2} \underbrace{\left[\sum_{n=-\infty}^{\infty} \mathrm{sinc}^2\left(\frac{N_F}{2}\left(\frac{f}{z} - \frac{n}{M}\right)\right)\right]^2}_{g_{grat}{}^2}, \qquad (2.32)$$

where N_F is the Fresnel number of the lens and is related to the number of segments b by $N_F = 2Mb$. Eq. 2.32 predicts the focal shift and is also valid for low Fresnel numbers. As in Eq. 2.31, it can be separated into a grating (g_{grat}) and a blaze (g_{blaze}) term. For $N_F = 2M$ we have one segment, Eq. 2.32 reduces to Eq. 2.24. With Eq. 2.32, the transition from a diffractive to a refractive lens can be analyzed. A refractive behavior is seen, if the width w_g of the peaks of g_{grat} is equal to the width w_b of the envelope g_{blaze}. This is the case if the lens has only one segment. In the previous Sections, we investigated the transition by increasing the phase-matching number M (Sec. 2.5.2) and the evolution of the diffractive behavior by increasing the Fresnel number (Sec. 2.5.1). For increasing M, the width w_b of the refractive envelope g_{blaze} reduces until $w_g = w_b$ for $M = N_F/2$, whereas w_g remains constant. For the case of increasing Fresnel numbers, the peaks in g_{grat} become narrower and are $w_g < w_b$ for $N_F > 2$, thus beginning to show a diffractive type behavior.

We can conclude that a diffractive type of behavior is also present for DOEs with deep relief structures working in high diffraction orders if more than one segment is illuminated. This type of diffractive behavior for DOEs with deep relief structures (large M) is not necessarily the same as that of a first order DOE.

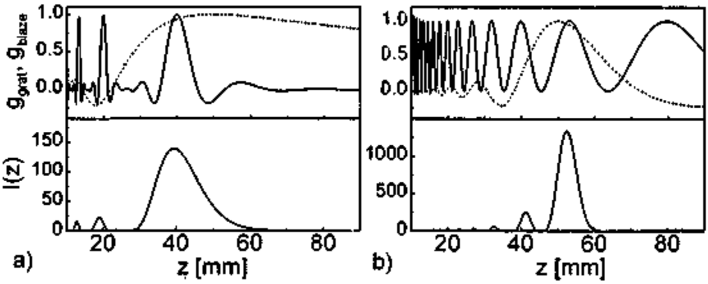

Fig. 2.16: Grating (solid line) and blaze (dashed line) contribution to the on-axis diffraction pattern I(z) of depth scaled lenses ($\mu = 0.8$) with two segments illuminated for a) $N_F = 4$, $M = 1$ and b) $N_F = 16$ and $M = 4$.

To illustrate this fact, Fig. 2.16 shows the grating and blaze contribution and the on-axis diffraction pattern for two depth scaled lenses ($f_0 = 40$ mm, $\mu = 0.8$) with two zones for $M = 1$ and $M = 4$. Even if both lenses have diffractive properties, their on-axis intensity behaves differently. For the lens with $M = 1$ and $N_F = 4$, the focal length is practically unchanged (cf. 2.5.1), for the lens with $M = 4$ and $N_F = 16$, the focal length changed to $f = 53$ mm, due to a change of the active diffraction order from 4 to 3. A refractive lens would show a similar focal length change for the same parameters. This example shows, that for specific parameters, a diffractive lens can show a similar behavior as a refractive lens. However, the underlying mechanism is different for the two types of lenses.

We can summarize the optical performance of a diffractive lens as follows. The lateral pattern, given by the zone boundaries defines the allowed directions for the diffracted light. This is described by the term g_{grat} that acts like a *structure factor*. The phase profile within the grating lines distributes the light among these allowed orders. It is described by g_{blaze} that acts like a *form factor*.

A depth scaling will affect the form factor but will not affect the structure factor. It therefore only changes the intensity distribution between the individual orders. Illumination with a wavelength $\lambda \neq \lambda_0$ affects the structure factor and the form factor since both, the phase delay (cf. Eq. 2.8) and the grating diffraction equation, depend on the wavelength.

A change in focal length and intensity distribution is the consequence. The same statement holds for the thermal behavior.
For DOEs working in high diffraction orders ($M > 1$), the free spectral range is reduced [Fle 97], the allowed diffraction orders are less separated. As a consequence, a quasi refractive behavior is observed [Sin 95] and is used for the design of diffractive lenses with reduced chromatic aberrations [Swe 95, Fak 95, Ron 95].

This completes the theoretical treatment of the continuous-relief diffractive lenses. In the next Chapter, we focus on the practical realization of these diffractive elements.

3. Fabrication

Micro-optical elements are manufactured by many different technologies, leading to different physical implementations of the phase function. Each form of realization and each fabrication technology has its own strength in terms of turn around time, flexibility, suitability for low cost mass fabrication and integration of the micro-optical element into opto-mechanical microsystems.

The main technologies for the fabrication of micro-optical elements include binary and multilevel technologies [Ste 97], reflow techniques for refractive lenslets [Dal 90, Völ 97], gray tone lithography [Osh 95, Sul 95, Rei 97, Opp 95], and ion exchange techniques [Saa 94]. These parallel technologies, requiring one or a set of exposure masks, can profit from advances in very large scale integration (VSLI) developments of microelectronics.

A second group of technologies are direct write or serial technologies and include single point diamond turning [Blo 97], electron beam writing [Fuj 82, Däs 95], and laser beam writing [Gal 94, Kor 95, Bow 94 , Lan 92]. An extensive overview over these direct write technologies is given by Gale [Gal 97].

Our approach of DOE fabrication can be divided into two steps. First, a master is fabricated by direct laser beam writing. From this original, copies at low cost are obtained in the second step by replication techniques. In the first two sections of this chapter, we describe briefly the master generation by direct laser beam writing and the replication techniques used. Finally, the fabrication parameters of direct laser beam writing are analyzed and their influence on the optical performance investigated. This gives us the basis for the optimization and modeling procedures of Chapter 4.

3.1 Laser beam writing

Development work on the laser writing technology has a long tradition at PSI Zurich (formerly RCA Labs. and now CSEM) [Gal 83, Gal 94, Gal 97]. The basic working principle of a laser writer consists of a raster scan of a photoresist coated substrate under an intensity-modulated focused laser beam. The surface relief is obtained after development of the exposed resist.

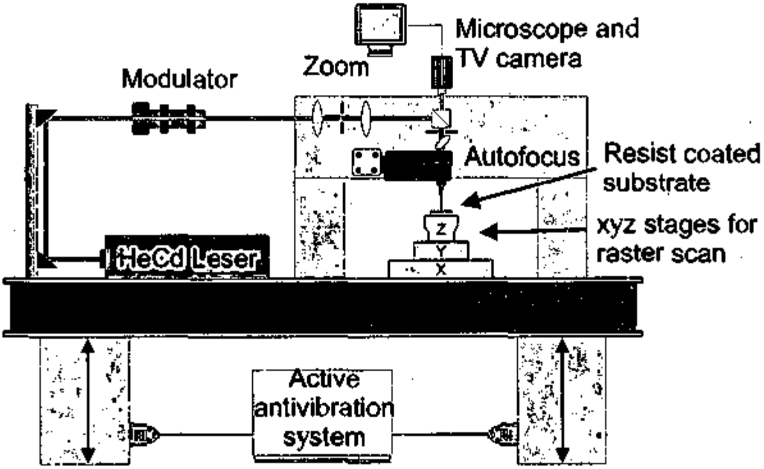

Fig. 3.1: Schematic of the 3rd generation laser writing system (LW3) developed at the PSI.

In the following, we describe briefly the main features of the 3rd generation laser writing system (LW3) which was developed at the PSI over the last years (Fig. 3.1). A HeCd laser, operating at a wavelength of $\lambda = 0.442\ \mu m$ is used as light source. Beam pointing instabilities and intensity fluctuations of this gas laser are corrected for by adequate means. The stabilized laser beam is modulated by an acousto-optical modulator with 8-bit resolution. A modified compact disk (CD) autofocus system controls the focus position on the substrate. The vertical range of this autofocus system is rather large (± 500 μm), which also allows its use on non-planar substrates. A TV camera enables an on-line monitoring of the writing spot. Additionally, the intensity distribution of the focused writing spot is routinely measured in the two scanning directions with a knife edge technique. An amplitude grating ($\Lambda = 80\ \mu m$) is mounted on a detector and scanned by the translation stages under the focused beam. The intensity distribution is obtained by taking the derivative of the detector signal and is then fitted with a Gaussian function:

$$I(x) = I_0 \exp\left\{-2\left(\frac{x}{w}\right)^2\right\} \qquad (3.1)$$

The waist *w* of the beam is referred to as the writing spot size and is typically adjusted in the range of 0.8 - 2.0 µm.

The raster scan is performed at a velocity of 50 mm/s by roller bearing translation stages (Newport PM500) with a specified resolution of 25 nm. A proper control of the scan movement is essential for obtaining high quality surface structures with high resolution. The stages are shown in Fig. 3.2 together with a 50 × 50 mm² substrate on the circular substrate holder and the autofocus system above.

Fig. 3.2: Photo of the scanning stages and autofocus system of the LW3.

For the scan, the depth values of the desired surface relief have to be converted into a two-dimensional bitmap of exposure intensities, taking into account the sensitivity of the photoresist and the raster scan geometry. The exposure data values are loaded line by line into a buffer and are clocked out by the translation stage pulses during each line scan. The interscan distance Δy - the distance between two subsequent line scans - is Δy = 400 nm or multiples of it. The bitmap of the exposure data has a minimum pixel size of $p_x = p_y = 400$ nm, corresponding to 12.5 Megabyte of exposure data per mm². For elements with large areas, the exposure data is calculated line by line to avoid large data files. At a writing speed of 50 mm/s, the exposure data rate is 125 kHz. The modulator and the PC hardware for the digital-analog conversion of the modulator input voltage must have a bandwidth considerably larger than this value in order to reproduce even sharp intensity changes required for the profile steps.

The writing time for large area DOEs such as lens arrays can be many hours, therefore a stable environment is an important requirement for the writing system. In order to reduce the effect of vibrations, the whole table is mounted on an active anti-vibration system.

The photoresist originals are usually not directly used for the application. They do not have the required mechanical and chemical stability. If only one single element is needed, the structure can be transferred into quartz to meet the stability requirements. However, for some investigations in this thesis (cf. Chapter 4), we used directly the photoresist originals. This gives us a test of the laser lithographic structuring process without the influence of additional process steps.

3.2 Replication

Continuous-relief diffractive structures are well suited for low-cost mass production by replication techniques. An extensive overview over replication techniques for micro-optical elements can be found in [Gal 97a].

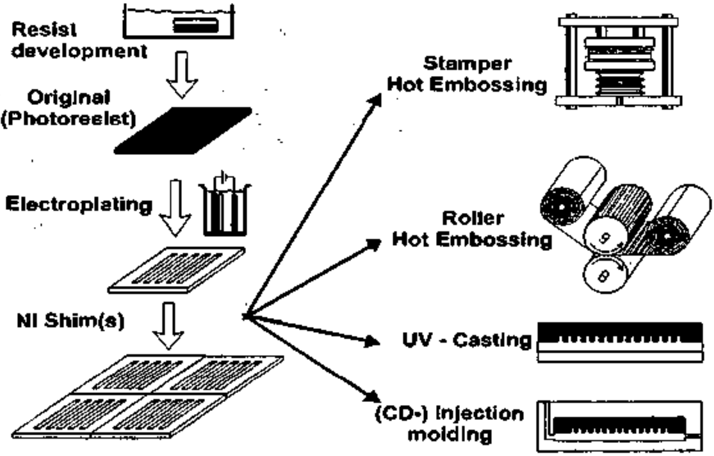

Fig. 3.3: Replication process: A negative copy is formed from the original structure in an electroplating process. This Ni shim can be used for various replication methods, such as hot embossing, casting or injection molding [Gal 97].

Fig. 3.3 shows an overview of the major replication technologies. From the original resist structure, a Ni shim is formed by electroplating the gold-coated resist relief. From this first Ni shim, second and third generation shims may be formed by additional electroplating steps. They can also be combined [3DLtd] for hot embossing using large area, industrial roller machines. Structures with deeper reliefs (2-5 μm) are replicated by UV-casting or injection molding techniques. For small volume or prototype production, stamper hot embossing is used. The choice of the replication technology depends on the requirements on the substrate flatness, the mechanical stability, the number of replicas and the integration of additional alignment or housing features.

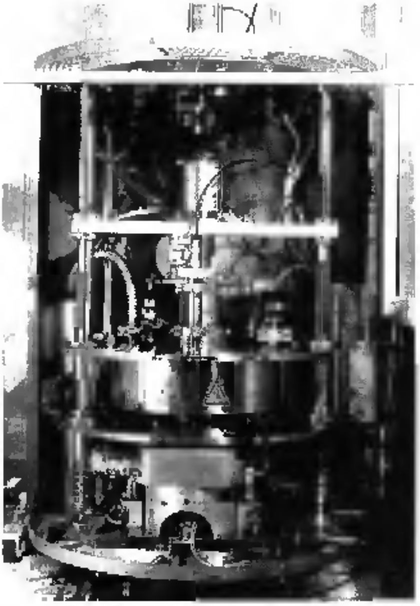

Fig. 3.4: Hot embossing machine for the replication on a laboratory scale.

For the replication work in this thesis, we used hot embossing in polycarbonate and UV-casting onto glass. Both technologies are routinely used at the PSI Zurich. Fig. 3.4 shows a hot embossing machine suitable for the replication on a laboratory scale. At temperatures above the glass temperature T_G of polycarbonate, the Ni-shim is pressed into a thin (typically 250 µm to 1 mm) polycarbonate foil for approx. 4 min. The pressure is then removed and the shim and replica are cooled below T_G before they are separated. The microscopic replication fidelity for typical structures investigated here is very high, additional surface roughness due to the replication process is negligible [Gal 94].

The planarity of the replicated substrates is much more difficult to control. The embossing process itself can be performed without introducing additional waviness [Jun 96]. However, it is a challenge to obtain Ni shims with a high degree of planarity. The galvanoform process can introduce stress in the metal shim which leads to a certain degree of waviness. This can become a limitation for applications with high requirements on the surface planarity (cf. Sec. 5.3). In a recent development, the galvanoform process could be optimized to overcome this problem. An alternative way is to transfer the photoresist directly into quartz and use this master for UV embossing onto glass. As industrial replication technique, injection molding was used for the fabrication of refractive / diffractive hybrid lenses in collaboration with an industrial partner [Phi].

3.3 Characterization

To control the development process of an exposed substrate, a calibration structure is written with the DOE structure and measured with a profilometer. If the desired depth is not reached, a subsequent development is performed. With such a stepwise development, a depth control within 2 % can be achieved.

The surface topological characterizations of the fabricated elements were performed by atomic force microscopy (AFM) and scanning electron microscopy (SEM). For the optical characterization of the fabricated elements we measured the intensity in the diffraction orders with a masked photo detector. The whole diffraction pattern in a given plane is measured with a CCD camera or alternatively with a scanning detector and pinhole to obtain a higher resolution in intensity. For the diffraction efficiency measurements of the blazed gratings, the substrate with the photoresist layer was attached to a prism with an index matching fluid. This reduces errors introduced by interference effects due to a wedge of the substrate.

3.4 Tolerances and limitations

A fabricated microstructure may differ in certain ways from the desired surface profile. Reasons for this deviation are mostly found in the limited resolution of the fabrication technology and in its tolerances. The proximity scattering in the resist is a major limitation for electron beam writing [Ekb 94, Nik 95, Däs 95]. Multilevel binary optics fabrication can suffer from etching and alignment tolerances [Cox 91, Far 90, Ric 93].

For laser beam writing, especially the sharp profile steps in DOE can not be reproduced exactly, this is mainly due to the finite extension of the writing spot size. Furthermore, the whole fabrication process includes several mechanical (scan movements) and chemical (exposure, development) processes. Their respective tolerances will also influence the final result.

The fabrication of diffractive structures, which are the front edge of today's technology capabilities, requires a quantitative understanding of these limitations and tolerances. For direct laser beam writing, the main topics to be considered are etching tolerances, positioning tolerances of the scanning stages, and the resolution limitations given by the finite size of the writing spot. An analysis of their influence on the optical performance of continuous-relief diffractive optical elements is given in this Section 3.4.

3.4.1 Etching tolerances

The key to a reproducible fabrication process is a calibration that connects the exposure values to the etching depth of the micro structure. Typically, the etching depth is well controlled within ± 5 %. With more calibration effort and more sophisticated photoresist process control an accuracy of ± 2 % can be achieved. The influence of etching errors on the diffraction efficiency of continuous-relief diffractive optical elements has been studied by Rossi et al. [Ros 95]. We define the etching error as a depth scaling value

$$\mu = d/d_0 . \tag{3.2}$$

d being the measured and d_0 the desired depth. The diffraction efficiency of the Nth diffraction order of a continuous-relief diffractive lens designed to work in the Mth order is given by [Ros 95]:

$$\eta_D = \mathrm{sinc}^2(\mu M - N). \tag{3.3}$$

Equation 3.3 also follows directly from Eq. 2.32. Changes in the incident wavelength can also be described by replacing μ by $\mu\alpha$ where α is the relative wavelength shift [Ros 95]. The diffraction efficiency η_D is plotted for various phase-matching numbers in Fig. 3.5. As can be seen from the Figure, the tolerances become significantly tighter for higher phase-matching numbers M.

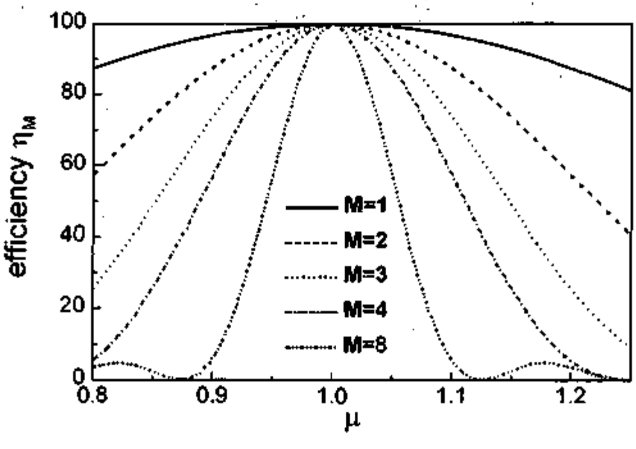

Fig. 3.5: Increasing the phase-matching number reduces the tolerances to etching errors.

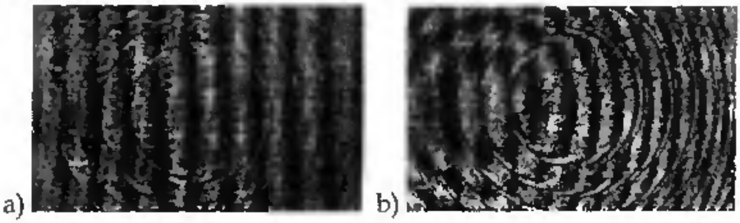

Fig. 3.6: Interferogram of a second order diffractive lens with a) correct depth and b) 20 % depth scaled.

Figure 3.6 shows an interferogram of a section of a diffractive lens with a correct depth (a) and a wrong depth (b) where the interference fringes are not matched at the profile steps. To illustrate the effect of the missing phase-matching on the wavefront, we calculated the wavefront behind a diffractive lens with the simulation technique described in Chapter 2.4. The resulting distorted phase is shown in Fig. 3.7. During further propagation, additional diffraction orders are developing from this distorted phase. For $\mu > 1$, the light missing in the desired focus is mainly found in diffraction orders $N > M$ and for $\mu < 1$, the light is mainly found in diffraction orders $N < M$.

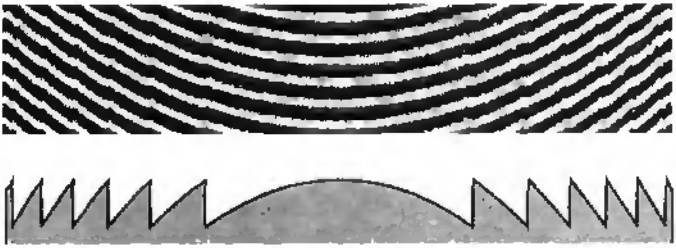

Fig. 3.7: Phase calculated 1 µm behind a diffractive lens, illuminated with a plane wave ($\lambda = 0.5$ µm). The parameters of the F/4 lens are $M = 1$, aperture radius $a = 50$ µm and $\mu = 1.1$.

3.4.2 Spot convolution

In order to reduce the effect of variations in the interscan distance and other tolerances of the scanning stages, a large writing spot is desired [Gal 83]. On the other hand, a large spot limits the resolution of the writing system. Mathematically, the profile obtained by the writing process is given by the convolution of the input surface relief with the point spread function of the writing spot. This results typically in a rounded profile as sketched in Fig. 3.8. A part of the relief has the wrong local slope, this is also referred to as *dead blaze* ε.

In Pub. II a formula for the diffraction efficiency for convoluted profiles was derived:

$$\eta_C = \left(\frac{\tilde{\Lambda}}{\Lambda}\right)^2 = \left(1 - \frac{\varepsilon}{\Lambda}\right)^2, \tag{3.4}$$

where ε is the "dead blaze" as defined in Fig. 3.8. A similar result was obtained by [Fuj 82].

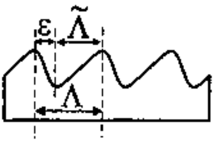

Fig. 3.8: The finite size of the writing spot leads to rounded profile steps. Part of the grating is considered as dead blaze ε .

The derivation of Eq. 3.4 simply assumes a fixed part of the structure to have the wrong blaze and light passing through this part as lost. This is a rough approximation to the real convoluted profile. In numerical simulations (cf. Sec. 2.4) of convoluted blazed gratings, we found that the diffraction efficiency follows very well the Eq. 3.4 for varying ε/Λ. Furthermore, we could relate the dead area ε to the writing spot w size by $\varepsilon = a_M w$ which modifies Eq. 3.4 to:

$$\eta_C = \left(1 - \frac{a_M w}{\Lambda}\right)^2. \tag{3.5}$$

The coefficient a_M depends on the phase-matching number M. For an illuminating wavelength $\lambda = 0.633$ µm and refractive indices $n_1 = 1.64$ and $n_0 = 1.0$ the values $a_1 = 1.466$, $a_2 = 1.794$, $a_3 = 1.948$, and $a_4 = 2.094$ were obtained. With Eq. 3.5, we are now able to relate the diffraction efficiency calculation directly to an important fabrication parameter, the writing spot size.

Equation 3.5 gives us an integral information of the influence of the convolution effect on the diffraction efficiency. To illustrate the effects on the phase distribution in the near field, Figure 3.9 shows the calculated optical phase behind the convoluted surface profile of a diffractive lens illuminated with a plane wave. A typical diffraction spectrum for a convoluted blazed grating is shown in Fig. 5 of Pub. II. The main part of the light missing in the desired diffraction order M is found in orders $N < M$. This is already indicated in the phase plot of Fig. 3.9.

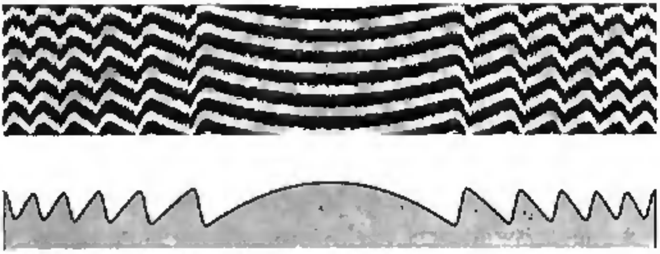

Fig. 3.9: Calculated phase 1.0 μm behind a lens with a convolution effect ($w = 1.0$) and correct depth ($\mu = 1.0$). The other parameters are as in Fig. 3.7.

In Section 2.4, we presented the *shadow effect* as a model to explain the theoretical limitation on the diffraction efficiency for blazed gratings with small periods. In this Section we have seen that the diffraction efficiency of fabricated blazed structures with small periods is strongly influenced by the convolution effect (cf. Eq. 3.5). The two effects, the *shadow effect* and the *convolution effect* are different in nature. The convolution leads to a distorted phase with unit amplitude, whereas the shadowing modifies the amplitude distribution and leaves the phase unchanged, i.e. correct. In Pub. II we obtained the following relation for the diffraction efficiency for the combination of both effects [Pub II]:

$$\eta_{CS} = \eta_C \, \eta_S \, . \qquad (3.6)$$

This indicates that a loss of the *active area* at the profile steps does not reduce the shadow effect contribution to the diffraction efficiency.

3.4.3 Interference effects

In Sec. 3.4.1 and in Sec. 3.4.2 we discussed how the etching tolerances and the convolution effect influence the efficiency of the diffraction orders. It depends on the type of DOE in which way a redistribution of the power among the diffraction orders influences the optical performance.

For a focusing element the main effect is a lower irradiance in the focal spot. The irradiance of the unwanted (non-focused) diffraction orders in the focal plane is very low compared to the irradiance of the desired, focused diffraction order. Thus, depending on the application, the existence of the remaining light does not necessarily degrade the overall performance.

However, the situation is different for non-focusing elements, such as beam shaping elements or for lenses at distances $z \neq f$. The power of the wanted diffraction orders is then distributed over a much larger area than it is the case for a focusing DOE. This situation is typically more sensitive with respect to light in unwanted orders. We consider for simplicity the case of a diffractive lens in a observation plane at $z \neq f$. For a lens with uniform illumination and 100% efficiency in the desired diffraction order, we obtain a uniform irradiance distribution in the observation plane. If other diffraction orders are active, the uniformity is destroyed due to the interference of these diffraction orders. This situation is schematically indicated in Fig. 3.10.

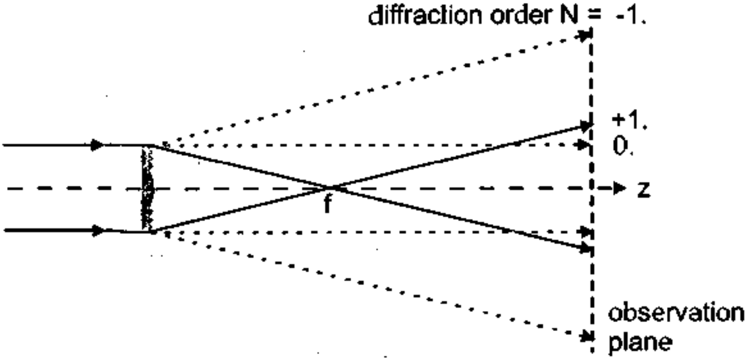

Fig. 3.10: Etching errors and convolution activate unwanted diffraction orders. The intensity pattern in a plane behind the lens is then given by the interference of these orders.

The contrast of the interference pattern is determined by the power of the contributing diffraction orders and the area occupied by these orders. The area A of a given diffraction order N for a circular diffractive lens with a constant phase-matching number M at a distance $z > f$ is given by (cf. Fig. 3.10):

$$A_{M,N}(z)=\pi\left[\left(z-\frac{M}{N}f\right)\tan\left(\left|\frac{N}{M}\right|\theta\right)\right]^2, \qquad (3.7)$$

where $\theta=\arcsin(NA)$. In the paraxial approximation ($sin(x) \approx tan(x) \approx x$) this reduces for $z >> f$ to $A_{M,N}(z)\approx\pi\, z^2\theta^2(N/M)^2$. The ratio of the two areas occupied by two different diffraction orders N_1 and N_2 is then given by $(N_1/N_2)^2$ and stays constant with propagation. That implies that for a lens with $M = 1$, the first divergent order ($N = -1$) occupies approximately the same area as the desired order ($N = 1$) at any distance $z >> f$.

To obtain a feeling for the sensitivity of the uniformity of the irradiance pattern on fabrication errors, we consider the interference of two orders with the efficiencies η_1 and η_{-1} at a distance $z >> f$. The coherent addition of the amplitudes of the two contributing waves leads to an irradiance given by:

$$I = \left|\sqrt{\eta_1}e^{i\phi_1} + \sqrt{\eta_{-1}}e^{i\phi_{-1}}\right|^2 . \tag{3.8}$$

Using $\eta_1 + \eta_{-1} = 1$ and setting $\phi_1 = 0$ and $\phi_{-1} = \phi$ we obtain for the irradiance:

$$I = 1 + 2\sqrt{\eta_{-1}(1-\eta_{-1})}\cos(\phi) . \tag{3.9}$$

The uniformity error σ of the irradiance pattern is calculated by:

$$\sigma = \frac{I_{\max} - I_{\min}}{I_{\max} + I_{\min}} . \tag{3.10}$$

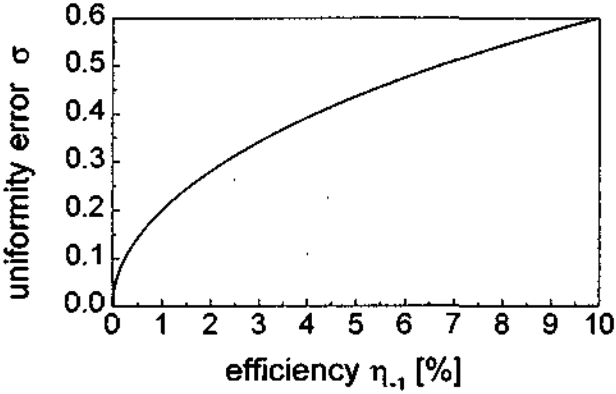

Fig. 3.11: Upper limit for the uniformity error as function of the -1. order diffraction efficiency.

An upper limit for the uniformity error σ is plotted in Fig. 3.11, assuming a maximum phase difference of $\phi = \pi$. Due to the coherent addition of the contributing waves, the resulting interference pattern is very sensitive on the existence of non-desired diffraction orders. Already a diffraction efficiency of $\eta_{-1} = 1$ % in the (-1)st order leads to a uniformity error of $\sigma = 20$ %.

Fig. 3.12 shows the intensity pattern for a diffractive lens ($M = 1$) with an intentional depth scaling and convolution effect in a plane $z >> f$. The lens is illuminated with a Gaussian beam to avoid aperture diffraction effects. The spot in the center is the zeroth-order contribution. The circular, non-homogenous irradiance pattern is the due to the interference of the desired order ($N = 1$) with unwanted orders (mainly $N = -1$). The intensity of the second order is too low to be resolved by the CCD camera and image acquisition system but could be seen in the experiment as additional circular pattern.

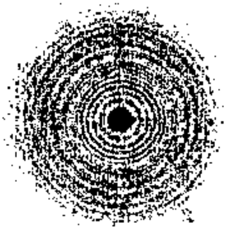

Fig. 3.12: Measured irradiance distribution for a depth scaled and convoluted lens ($z >> f$). The spot in the middle is the zeroth order, the other spots originate from surface roughness due to stage positioning errors.

In practice, this interference between the active diffraction orders can significantly reduce the performance of beam shaping elements. Similar observations have recently been reported by Leger [Leg 97].

For an application [Kun 97] requiring a high degree of uniformity in the intensity, the use of a diffractive beam shaping element for edge emitting semiconductor laser diodes was investigated. The beam shaper consists of two elements, following the design approach of Rhodes and Shealy [Rho 80] with an additional collimation function integrated in the first DOE. The distance between the DOEs is used as a design parameter to maximize the product of the diffraction efficiencies of both elements. The optimized DOE separation was found to be 12 mm, resulting in a very compact illumination module. However, this leads to small local grating periods which makes the fabrication challenging in order to avoid the interference effects discussed above. Bengtsson [Ben 96] has also recently reported on uniformity problems of a beam shaper for a semiconductor laser, fabricated by e-beam lithography. Most diffractive beam-shaping elements which have been reported up to now are designed for the infrared or have only low deflection angles, resulting in a non-compact overall design [Gol 96].

We can conclude that not only in terms of diffraction efficiency, a convolution effect as small as possible is desirable for the fabrication of DOEs with small grating periods. In Publication II (cf. Fig. 12 in Pub. II), we also compared the absolute influence of typical etching tolerances with typical convolution effects for high *NA* elements. We found, that the convolution influences the diffraction efficiency considerably stronger than etching tolerances.

3.5 Considerations on writing parameters

Additional fabrication parameters which have to be considered to obtain optimum performance are discussed in the following.

3.5.1 Depth of focus

The Gaussian writing beam is focused onto the photoresist air interface. In the photoresist layer the beam will expand during propagation. If we take the Rayleigh range $z_R = \pi\, w^2/\lambda$ [Ger 75] as a measure for the depth of focus, a spot size $w = 1.0\,\mu m$ results in $z_R = 12\,\mu m$ for the HeCd laser wavelength $\lambda = 0.442\,\mu m$. For the typically structures considered here (depths $d = 1 - 5\,\mu m$), the variation of the spot size is negligible. For the fabrication of very deep relief structures [Ros 97] or for smaller writing spot sizes w, the depth of focus has to be taken into account.

3.5.2 Interscan distance

Since the exposure is generated by overlapping Gaussian beams, a modulation in the profile with a grating period of the interscan distance is created. Gale and Knop [Gal 83] found that an interscan distance of $\Delta y = w$ keeps the modulation amplitude below 1 % of the average relief depth. However, if the interscan distance varies due to stage positioning errors, this modulation can become significant and the resulting grating structure leads to stray light and a reduction in the optical efficiency of the element

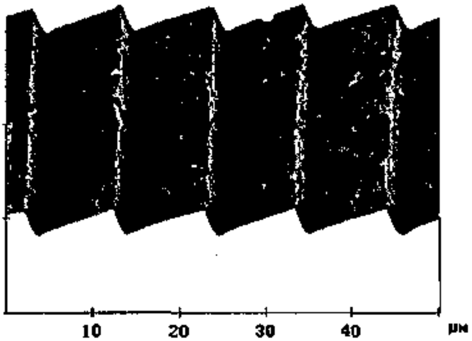

Fig. 3.13: AFM micrograph of a blazed structure. The scanning direction was perpendicular to the grating lines.

(cf. Fig. 3.13). Accurate control of the stage movements is essential to minimize this effect. It can only partly be reduced by a reduction of the interscan distance. Therefore the writing spot size for a specific element is chosen as large as possible to reduce the statistical or regular surface roughness. However, a large spot limits the resolution of the writing system. For the current system, the dynamic positioning accuracy is approximately ± 30 nm. The fraction of the scattered light $\eta_{Scatter}$ is in the order of a few percent.

3.5.3 Exposure pixel size

The exposure pixel size p has to be chosen small enough to allow for an adequate sampling of the diffractive structure. However, a large pixel size is desired to limit the amount of exposure data. The following two rules are given for a proper choice of the pixel size for a given set of fabrication parameters.

Blaze smoothing

First, we consider the case of a one-dimensional blazed grating. The intensity of the exposure data is given in quasi continuous values. The resolution of the data value quantization is only limited by the resolution of the modulator and the PC hard- and software. In most cases it can be regarded as continuous. Lateral however, the exposure data values are quantized in pixels of size p.

The writing of continuous-relief structures can, be regarded as the smoothing of the multilevel exposure data set (cf. e.g. Fig. 6 in Pub. II) with a Gaussian function of width w [Kui 95]. The ratio w/p has to be sufficiently large to smooth the multilevel exposure data and to obtain a continuous-relief blaze. In simulations we found that the requirement on the pixel size p is rather relaxed, a ratio $w/p \approx 1$ is usually sufficient, smaller pixel sizes do not lead to improvements in diffraction efficiency. However, the situation changes if the exposure data pixels are individually optimized as done in Sec. 4.3.

Sampling effects

The exposure data values have to be sampled in the coordinate system of the scan. If the optical element does not have the same symmetry as the scan process, sampling effects occur. For high numerical aperture lenslets sampled in a cartesian coordinate system, spurious lenslets appear if the pixel size is in the order of the minimum zone extension or above

[Car 94]. This effect can be reduced for a fixed pixel size by using higher phase-matching numbers [Hes 97].

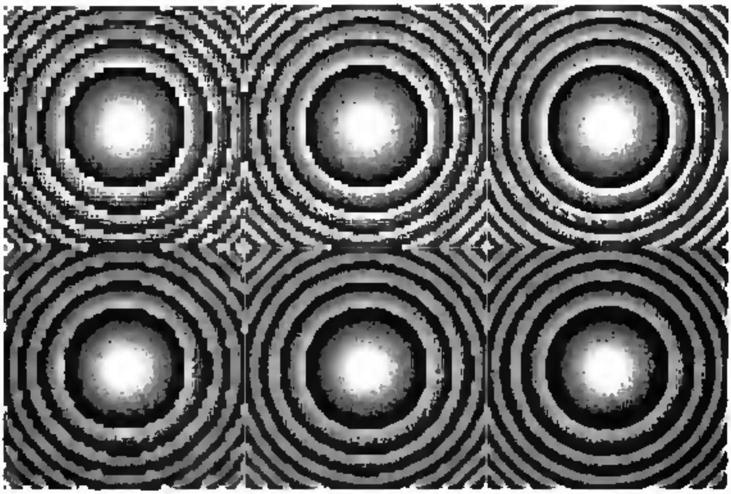

Fig. 3.14: Effect of exposure pixel size. *Upper row:* Exposure data of a circular F/2 lens sampled in cartesian coordinates with pixel size (from left to right) of 1.2 μm, 0.8 μm and 0.4 μm. *Lower row:* Resulting surface profile after convolution with a writing spot of $w = 1.2$ μm.

However, independently of the *NA*, the sampled circular structures show the rectangular raster pattern. Figure 3.14 shows the exposure data of a lens (*F*/2) sampled with pixel sizes of $p_x = p_y = 1.2$ μm, 0.8 μm, and 0.4 μm and the resulting surface relief, obtained by convolution with a writing spot of $w = 1.2$ μm. The pixel size should be chosen approximately three times smaller than the spot size to obtain smooth circular zones. This situation is shown in the right column of Fig. 3.14.

We conclude that for most applications, the pixel size should not exceed 400 nm for a writing spot size of $w = 1.0\text{-}1.5$ μm.

In this chapter we have obtained a qualitative and quantitative understanding of the strength, tolerances, and limitations of the fabrication technology. Together with the results from Chapter 2, we use this knowledge for the surface profile optimization in Chapter 4.

4. Surface profile optimization

In the second part of Chapter 3 we identified the convolution effect as a main limitation in the fabrication of continuous-relief diffractive optical elements with a high diffraction efficiency. Our aim is to optimize the surface relief in a way that the convolution effect is minimized and the fabrication tolerances remain relaxed. The following optimization procedures are based on the use of the design freedoms (cf. Sec. 2.2) and the analysis of the fabrication tolerances and limitations (cf. Sec. 3.4). A more detailed treatment of the optimization procedures is found in Pub II.

4.1 Use of design freedoms

For a constant writing spot size, the *dead blaze* ε (cf. Fig. 3.8) mainly depends on the aspect ratio of the structure. The total dead area of a DOE is lowered by reducing the total number of profile steps. This is achieved by using higher phase-matching numbers M, the most important of the design freedoms presented in Section 2.2.

Figure 4.1 shows the measured diffraction efficiencies for blazed gratings with periods between 4 µm and 360 µm, designed for $M = 1$, 2 and 3. The efficiencies were normalized to the transmission through the unstructured substrate. For $\Lambda/M = 10$ µm, the efficiency of the first order grating ($\eta = 64$ %) could be increased to 72 % and 81 % for $M = 2$ and $M = 3$, respectively. As can be seen from Fig 4.1, working with phase-matching numbers up to $M = 3$ leads to a significant increase in diffraction efficiency up to very large periods ($\Lambda = 60$ µm). These measured results are in good agreement with calculated values based on Eq. 3.5.

The use of higher phase-matching numbers for dead area reduction is simple in terms of data generation. Moreover there is no necessity to know of the exact writing spot size. However, working in higher diffraction orders increases the total number of propagating diffraction orders and the free spectral range, this can be disadvantageous for some applications. The deeper profiles impose the need for thicker resist films which requires non-standard processing and also limits this approach due to reduced etching tolerances for higher *M*'s.

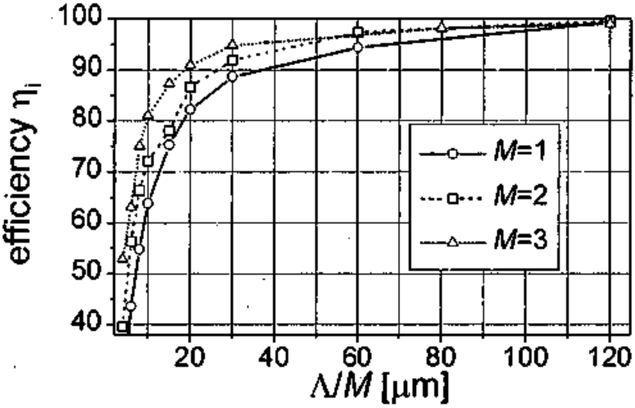

Fig. 4.1: Measured diffraction efficiencies for blazed gratings with different periods, working in the first, second and third order. The diffraction efficiency has been normalized to the total transmission in the grating diffraction plane.

The use of a constant phase-offset φ_0 (cf. Sec. 2.2.2) in order to minimize the influence of etching errors is investigated in Pub. I. In Pub. II we use it to minimize the influence on convolution effects. We found that for lenses with a small number of zones the focal length stability upon etching errors can be significantly improved by adding an appropriate phase-offset.

Elements with an arbitrary zone position and size (cf. Sec. 2.2.3) were investigated in numerical simulations and experiments. As a main feature, we found for depth errors ($\mu \neq 1.0$) or for illumination with a "*wrong*" wavelength ($\lambda \neq \lambda_0$) a different angular distribution of the unwanted "stray" light. In comparison with the diffraction pattern of a lens with a regular zone positioning, the unwanted diffraction orders are smeared out and no longer well defined.

4.2 Linear scaling

For convoluted blazed gratings we found that the first order diffraction efficiency as a function of a the depth scaling μ differs from the behavior of non-convoluted gratings, as it is described by Eq. 3.3. The convoluted gratings show the maximum in first order efficiency for depth scaling values $\mu > 1$. Thus, an intentional depth-scaling is used to increase the first order diffraction efficiency for convoluted gratings. Moreover, the efficiency in the zeroth order is reduced by a linear distortion of the exposure data. For blazed grating structures, the optimum depth scaling factors to achieve a maximum first order and a vanishing zeroth order diffraction efficiency are shown in Fig. 4.2.

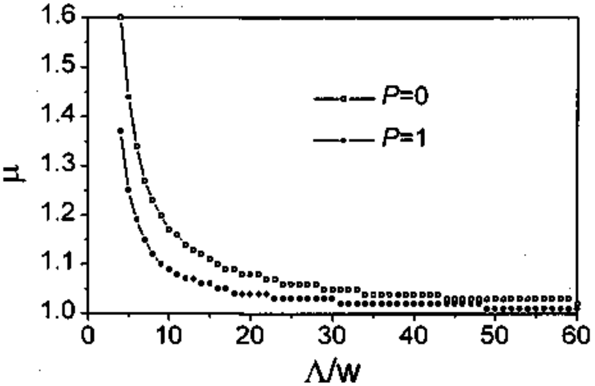

Fig. 4.2: Depth-scaling factors to achieve maximum first or minimum zeroth order diffraction efficiency, respectively. The discrete steps are due to a discrete resolution in the calculation and have no physical meaning.

4.2.1 Zero order suppression in CGH's

The design of computer generated holograms (CGH) with an iterative Fourier transform algorithm (IFTA) is pixel-based. The typical output is a phase bitmap which varies from pixel to pixel without obvious correlation (cf. 4.3 a). Therefore, the surface profile to be fabricated consists of many profile steps. Fig. 4.3 b shows an optical microscope image of a section of the laser-written CGH. The surface relief consists of small features with rectangular shape. Especially for CGHs having a pixel size p_{CGH} in the order of the writing systems minimum feature size, the convolution effect is observed in the optical reconstruction [Lar 94]. This is manifested in a large zeroth order contribution. In Publication II, we successfully demonstrated the suppression of this zeroth order by applying a linear scaling to the exposure data.

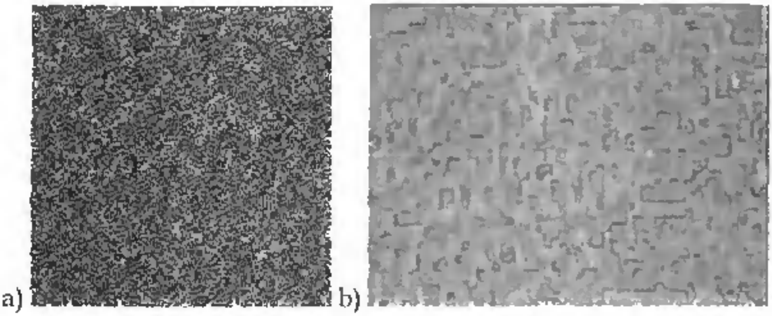

Fig. 4.3: CGH phase relief (a) and a fabricated section of it as optical microscope image (b).

The optical reconstruction of a CGH with a small pixel size of 3 x 3 µm² is shown in Fig. 4.4 for $\mu = 1.0$ and with a suppressed zeroth order for $\mu = 1.65$. In order to experimentally demonstrate the effect, we chose a rather small ratio p_{CGH}/w.

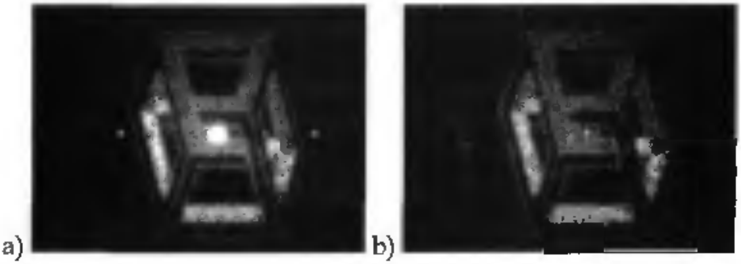

Fig. 4.4: Optical reconstruction of a CGH with (a) standard depth ($\mu = 1.0$) and (b) optimized depth ($\mu = \mu_0 = 1.65$). The zeroth order could be reduced to average signal level.

We take the example of a simple binary grating ($\Lambda = 8$ µm, $\lambda = 0.5$ µm, $n = 1.5$) to illustrate the underlying mechanism of the zeroth order suppression.

The convolution of the square grating with the Gaussian writing beam leads to a rounding of the profile steps (Fig. 4.5 a). In order to obtain destructive interference along the optical axis, the integrated phase delay difference along one period between the grooves and hills has to be $\Delta\Phi = \pi\ \Lambda/2$. This is no longer fulfilled for the convoluted grating with $\mu = 1$. A linear depth scaling increases the phase delay in the hills and lowers it in the grooves. With a proper choice of the scaling factor μ, $\Delta\Phi = \pi\,\Lambda/2$ can be reached and thus a vanishing zeroth order η_0. Figure 4.5 b shows the linear scaled convoluted grating as well as the desired profile for comparison.

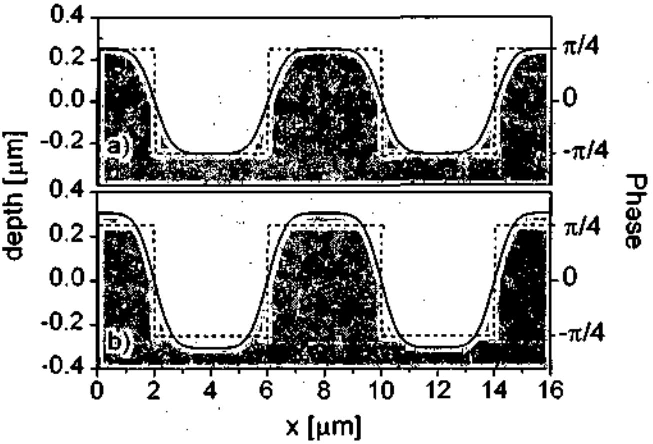

Fig. 4.5: Convoluted binary grating ($\Lambda = 8\,\mu m$, $w = 1.0\,\mu m$) for depth scaling of $\mu = 1.0$ (a) and $\mu = 1.22$ (b). The original square profile is also shown (dashed line), the corresponding phase delay is indicated at the right axis.

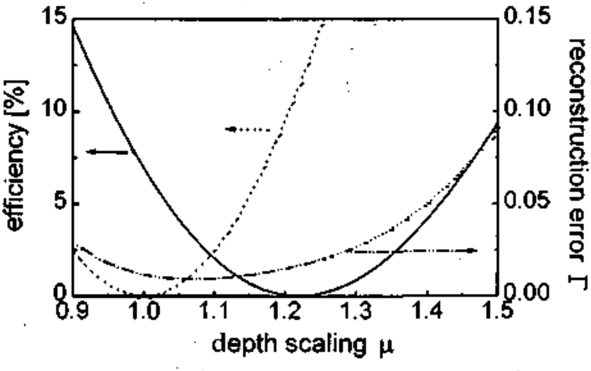

Fig. 4.6: Diffraction efficiency of the zeroth order for the depth scaled convoluted (solid line) and the original square grating (dashed line).

In Fig. 4.6, the zeroth order diffraction efficiency η_0 is plotted as function of the depth scaling for the convoluted square grating. For comparison, the same curve is plotted for the ideal, non-convoluted grating. The minimum of η_0 for the convoluted grating, located at $\mu_0 = 1.22$, is broader than for the original square grating, located at $\mu = 1.0$. These relaxed etching tolerances makes it comfortable to hit this minimum in the fabrication process.

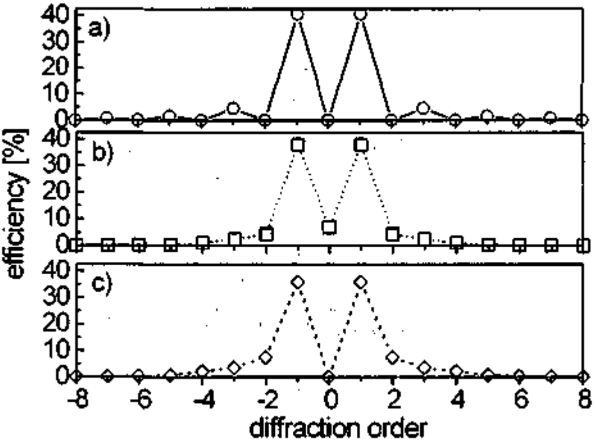

Fig. 4.7: Diffraction pattern of the square grating (a), the convoluted grating with $\mu = 1.0$ (b) and with $\mu = 1.22$ (c).

The diffraction pattern of the ideal square grating (a) and the convoluted grating with $\mu= 1.0$ (b) and $\mu = 1.22$ (c) are shown in Fig. 4.7. For the convoluted grating with $\mu = \mu_0$, we observe a reduction of the intensities of the first order in favor of the higher orders. As a measure for the deviation of the diffraction pattern of the convoluted grating to the diffraction pattern of the square grating we define the reconstruction error Γ by:

$$\Gamma = \sum_i \left(\eta_{c_i} - \eta_{s_i}\right)^2 \tag{4.1}$$

The diffraction efficiency of the orders i is η_{c_i} for the convoluted and η_{s_i} for the square grating. The reconstruction error Γ is plotted in Fig. 4.6. The suppression of the zeroth order is accompanied by an increase of the reconstruction error. The minimum of the zeroth order intensity is obtained at a different depth than the minimum of the reconstruction error.

When we apply these results to computer generated holograms or other complicated structures, we have to take the following into account. For the case of a CGH, the diffracted light is spread over many more orders than for the one-dimensional grating with a relatively small period. Typically, the signal window of a two-dimensional CGH consists of 256×256 or even 512×512 orders. Thus, the zeroth order can easily exceed the average intensity in the signal window and influence the element performance. The optimum depth scaling values μ_0 for a two-dimensional grating or CGH will be larger than for the one-dimensional gratings considered here, since the convolution effect has to be compensated in both lateral dimensions.

The direct laser beam writing technology is not optimized for the fabrication of such structures with a very large number of profile steps. A multilevel technology is usually more suitable. However, some applications require the combination of CGH structures with continuous-relief refractive or diffractive lenses on a single substrate. The fabrication of the individual pattern with different technologies waists the valuable advantage of accurate alignment by the single exposure run and increases the number of process steps involved.

If we follow the standard CGH design approach, we have to ensure that the CGH pixel size p_{CGH} exceeds the minimum feature size of the writing system. However, in Chapter 3 we showed that an exposure pixel size $p < w$ is still resolved laterally (cf. Fig. 3.14). An improved CGH design algorithm for laser written continuous-relief structures should use this fact by setting the CGH pixel size $p_{CGH} = p$ ***and*** limiting the minimum feature size of the CGH phase pattern above the writing spot size w. This should be explored in the future.

Such a design procedure for binary structures, based on a modified iterative Fourier transform algorithm (IFTA), has recently been demonstrated [Aag 97, Sch 97]. The motivation for this work was to exploit the full capability of modern high resolution lithographic e-beam systems but still uses a paraxial optical design. To fulfill the paraxial approximation, the maximum deflection angle and therefore the minimum feature size must be limited. Within the IFTA, a median filter replaces unwanted small feature sizes, leaving the resulting features with a more complex shape than simple squares.

4.3 Point spread function compensation for blazed gratings

In this section, we compensate for the convolution effect by optimizing a given set of exposure data, taking into account the spot size. Starting with a set of non-compensated exposure data points, the surface relief is calculated by simulating the exposure with the Gaussian writing beam. The difference between the resulting relief and the desired profile is added to this resulting relief [Ekb 94]. Corrected exposure data values are extracted taking into account the discrete nature of the exposure raster. The new exposure values are then limited to positive values within a specific range. Already after one to two iterations, considerable improvements in diffraction efficiency are achieved. Usually, the algorithm is stopped after 10 - 20 iterations, depending on the grating period, the spot size, and the exposure pixel size. A typical result for the exposure data and the resulting surface relief is shown in Fig. 4.8. A linear photoresist calibration relation was assumed. An AFM measurement of an optimized structure is shown in Fig. 4.9.

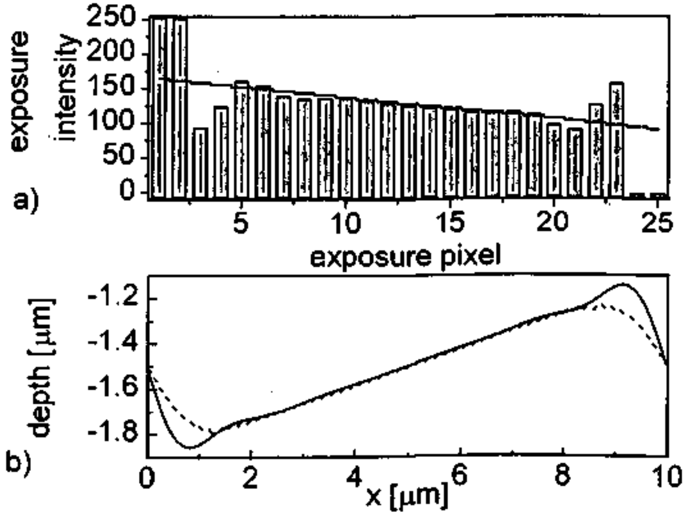

Fig. 4.8: Exposure intensities (a) and resulting surface profile (b) for an optimized (bars, solid line) and non optimized grating.

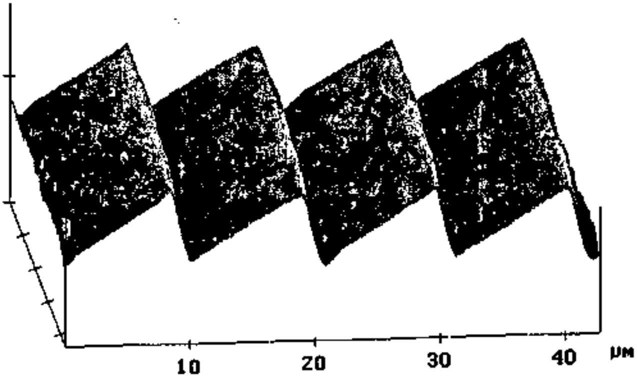

Fig. 4.9: AFM micrograph of a Λ = 10 µm first order grating with individual exposure pixel optimization. The vertical scale is 1 µm.

Table 4.1 shows the experimental obtained diffraction efficiencies for three different periods.

The individual pixel optimization method leads to a gain in efficiency comparable to the use of higher phase-matching numbers ($M = 3$ instead of $M = 1$) for a $\Lambda/M = 10$ µm grating. The achievahle gain in efficiency is considerable, the diffraction efficiency is increased by 30 % for a 10 µm grating from 61 % to 79 %. To obtain the same reduction of the convolution effect without optimization, approximately half the writing spot size would be required (cf. Eq. 3.5). With the optimization, we combine high diffraction efficiency with the advantages of a large writing spot resulting in a smooth surface, simpler data generation, and shorter writing time.

Table 4.1: Measured diffraction efficiencies in % of non-optimized and optimized blazed gratings. The calculated theoretical values are given in brackets.

	Λ = 6 µm	Λ = 10 µm	Λ = 20 µm
non optimized	41 (43.6)	61 (63.4)	83 (80.6)
optimized	64 (66.8)	79 (79.2)	90 (89.3)

We investigated the robustness of the optimized profiles (cf. Fig. 4.8) with respect to etching errors and uncertainties in the knowledge of the exact writing spot size. The optimized profile showed a better performance than the non-optimized profiles for a very wide range of the parameters µ and *w* (Pub II).

We conclude, that working in higher diffraction orders (Sec. 4.1) is a simple approach in terms of data generation, but it has to be balanced against the technology tolerances. We showed that with a well controlled resist processing, the influence of the tighter etching tolerances for $M > 1$ can be held below the achieved gain in diffraction efficiency.

The application of a linear scaling factor (Sec. 4.2) to correct for the convolution effect is especially suitable for complex structures and the suppression of the zeroth diffraction order.

The individual pixel optimization (Sec. 4.3) requires the greatest computational effort and the knowledge of the writing spot size. But it is advantageous with respect to fabrication tolerances.

4.4 Diffraction efficiency modeling

For the design of an optical microsystem, it is important to get an estimation of the diffraction efficiency of an individual element before it is fabricated and tested. Furthermore, especially for the use of higher phase-matching numbers the gain in diffraction efficiency due to a lower convolution effect has to be compared with the tighter etching tolerances. The diffraction efficiency of the DOE can either be calculated using the numerical method described in Sec. 2.4 or it can be calculated by locally decomposing the DOE into blazed gratings with period Λ and integrating the local diffraction efficiencies $\eta(\Lambda)$ over the whole element [Bur 92]. For a radial symmetric DOE with aperture radius a, the integrated efficiency is then given by:

$$\eta = \frac{\pi}{I_0} \int_0^a \left(\eta_s(r) + \eta_p(r)\right) \cdot i(r) \cdot r dr . \tag{4.2}$$

with the integrated incident intensity:

$$I_0 = \int_0^a i(r) \cdot 2\pi r dr , \tag{4.3}$$

$i(r)$ being the radial intensity distribution of the incident wave. Note that the efficiency value should be always accompanied by a specification of the illumination condition. The local diffraction efficiencies $\eta_s = \eta_s(\Lambda)$ and $\eta_p = \eta_p(\Lambda)$ for s and p polarization include the polarization dependent Fresnel losses. The local efficiencies are obtained from experiment or calculated with the knowledge of the writing spot size and the etching tolerances.

The Fresnel losses can be reduced by either applying an antireflection coating on the structure or by combining it with an inherent subwavelength grating structure [Hei 96, Nik 97]. The latter is a challenge in master generation but offers the advantage of fabricating the DOE with antireflection properties in one single replication step.

5. Applications

In this chapter we present applications of diffractive optical elements and microlens arrays that were investigated in the frame of this thesis. We show how applications in the fields of microscopy, optics in computing, wavefront sensing, and laser beam collimation can profit from the use of diffractive optical elements. Each application has its specific demands on the design and fabrication of the elements.

5.1 Lens arrays for confocal microscopy

Optical scanning confocal microscopy is a well established technique [Wil 84, Bra 79, Car 87] in which the capability of optical sectioning allows the three dimensional reconstruction of the topography of technical surfaces to be built up from a series of hundreds of depth discriminated height sections. High lateral resolution can be obtained by the use of high numerical aperture (*NA*) objectives, but the resulting field size is small. This disadvantage can be overcome by the use of a high *NA* microlens array, instead of a single objective, to extend the field size and add the possibility of parallel scanning [Tiz 94]. In order to obtain good measurement results, microlens arrays with small focal depth and small spherical aberration have to be used. Publication III describes the design and fabrication of a suitable lenslet array by direct laser writing lithography. Operated in reverse mode, the confocal microscope is a powerful tool for microlens array characterization.

5.1.1 Confocal microscope as characterization tool

The characterization of microlenses is a difficult task since the lenslets usually have a short focal length and a small aperture. In addition to the parameters of a single lens, their uniformity over the array is of great interest. A microlens array can consist of many thousands of individual lenslets, therefore a serial testing is not practical. Hutley [Hut 91] and Schwider [Sch 97a] developed measurement techniques for microlens arrays based on the extension of single lens measurement techniques [Sch 95]. This requires an extended field size for the measurement setup. The microlens array based confocal microscope can be modified into a lens array characterization tool: The object to be measured is replaced by a known object such as a flat mirror. This allows a parallel measurement of the properties of the microlens array itself.

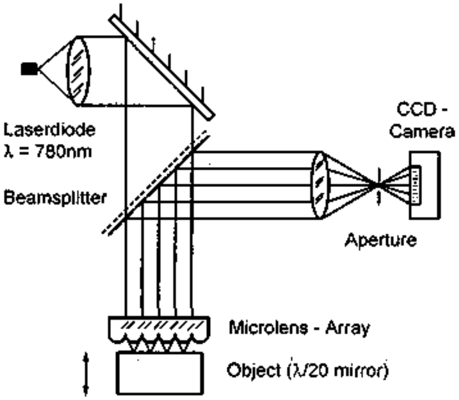

Fig. 5.1: A schematic sketch of a modified confocal microscope for characterization of microlens arrays. An optically flat mirror is used at the object plane [Pub III].

Fig. 5.1 shows the principal setup for a microlens array characterization. Typically measured parameters include the axial intensity response and the resulting focal length distribution over the array. From the axial response, valuable information about the diffraction efficiency and stray light can be obtained. This technique has been applied for the characterization of the lens arrays investigated in Publications III and IV. Although the lens arrays in Pub. III and IV were designed for the use in confocal microscopy, the characterization method described above is not restricted to lens arrays for this application. As one result of Pub. III, Fig. 5.2 shows the focal length distribution of a lens array with high numerical aperture ($NA = 0.3$) for the use in confocal microscopy. For a focal length $f = 250\ \mu m$ a mean variation of the focal length within one row of 120 nm was measured. This is an experimental evidence for the focal length stability of diffractive lenses as discussed in Chapter 2.5. Diffractive lens arrays are of great interest for applications requiring a very uniform and predictable focal length distribution. In the gray scale representation (Fig. 5.2 a), the waviness of the glass substrate can be seen as a limiting factor to obtain high focal length uniformity.

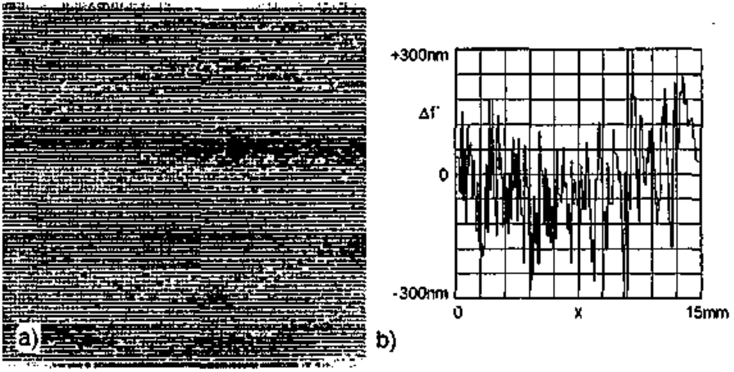

Fig. 5.2: Focal length variation Δf for a direct laser written microlens array. (a) Grey scale representation (0-5 μm) over the whole 15 x 15 mm field size (b) Cross-section along single lenslet row.

In the next Section we use this unique feature of diffractive lenses to "shape" the focal length distribution according to the application needs.

5.2 Lens arrays with spatial variation of the optical function

Microlens arrays consisting of refractive or diffractive lenslets have numerous applications in imaging, optical computing and detection systems. Most of the applications require microlens arrays with identical lenslets. An optimization of the fabrication process for a specific lens parameter set is therefore typically required. As an example, excellent results have been demonstrated for lithography systems equipped with refractive lenslets fabricated by a photoresist reflow technique [Völ 97]. However, if diffractive lenses are also feasible for a given application and corresponding fabrication technologies are available, the range of geometrical and optical parameters accessible for the individual lenslets is considerably enlarged. In particular, the lens numerical aperture *NA* can cover a very large range. In addition, the *variation* of the optical function over the lens array can help to enable, improve or simplify many optical systems. The parameters that can be changed include the focal length, (cf. Fig. 5.3), the lens anamorphism, the aperture and the beam deflection angle. The latter can be used to simplify solutions for spatially varying optical interconnectors in optical computing systems [Res 91] and for matching arrays with different optical pitch [Hut 96] in e.g. parallel optical sensing systems.

As demonstrations of arrays with a varying optical functions, lens arrays with a spatial variation of the focal length and beam deflection angle have been realized. In Pub. IV the lens design algorithms including the data handling and the experimental characterization results of the fabricated arrays are presented.

5.2.1 Spatial variation of the focal length

As first examples for lens arrays with a spatial variation of the optical functions, arrays with a variation in focal length have been fabricated. As an illustration for typical results achievable, the scanning electron micrograph in Figure 5.3 shows the section of a microlens array (aperture 100 x 100 µm²) with a parabolic variation of the focal length in two dimensions. The fill factor of the lens array is 100 %.

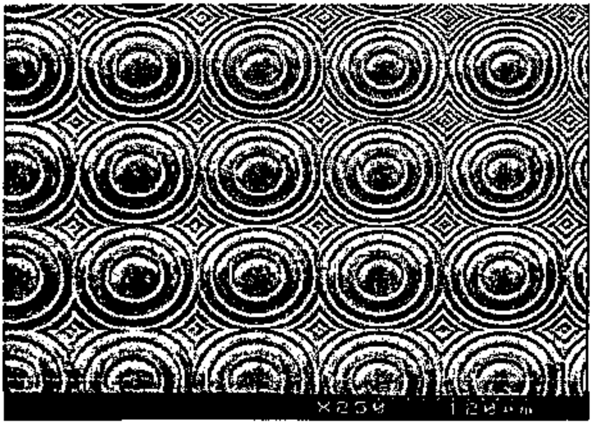

Fig. 5.3: Section of a diffractive lens array with a spatially parabolic varying focal length in both lateral dimensions. The lenslet aperture is 100 x 100 µm².

The confocal microscope was used to measure the focal length distribution of the arrays with a spatial varying focal length. The centers of gravity of the axial response curves are determined for the measurement of the focal length. The result for an array with a cylindrical focal length distribution (radius of curvature $R = 20$ mm) is shown in Figure 5.4. A very smooth distribution is obtained. The discrete focal length steps, resulting from the individual lenslets can be distinguished. The radius of curvature of the measured cylindrical focal length distribution fits well within the design value of $R = 20.0$ mm.

We also measured the lateral intensity distribution for the individual lenses. A diffraction limited behavior was found over the whole focal length range [cf. Fig. 5 in Pub. IV]. The exact achievement of the designed focal length distribution with diffraction limited performance over the whole parameter range for an array with a high fill factor is a powerful feature of diffractive lenses.

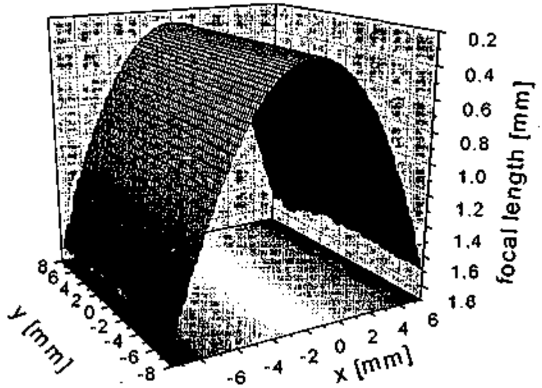

Fig. 5.4: Measured focal length distribution of a the lens array with a cylindrical focal point distribution.

5.2.2 Lens arrays focusing on curved objects.

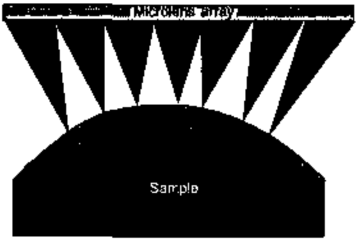

Fig. 5.5 : Principle of microlens array focusing onto a sphere.

We now combine a spatial variation of the focal length with a spatial variation of an additional deflection angle. The results is a lens array with off-axis lenses which focus onto a curved object. This situation is shown in Figure 5.5.

For such rather complex lens arrays, a feasibility study is performed before fabrication. This is illustrated for a lens array focusing onto a sphere. Figure 5.6 shows the sinus of the local deflection angle θ (sin(θ) = λ/Λ) for the inner and outer aperture edge of the individual lenses as function of their position x in the array. This information gives us a good overview of the structure which has to be fabricated. As we have seen in Chapter 3, the local grating period Λ (Λ = λ/sin(θ)) of a DOE should be maximized in order to obtain a maximum in diffraction efficiency. We use possible freedoms in the external parameters (e.g. lens aperture, radius of curvature, etc.) to balance high diffraction efficiency of the individual lenslets against other application requirements.

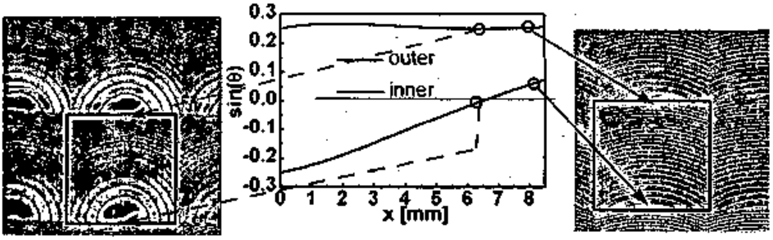

Fig. 5.6: Calculation of the local deflection angle to optimize the design with respect to fabrication issues.

5.2.3 Confocal microscopy on curved surfaces

The maximum object height variation to be measured with a microlens array based confocal microscope set-up (cf. Sec. 5.1) is restricted to the focal length of the microlenses. Lens arrays with spatially varying focal lengths are used on non-planar surfaces whose overall profile height exceeds the vertical measurement range of a microlens array based set-up, but is known within a reasonable accuracy. The lens array focal surface is shaped to fit the expected object shape. For such arrays, the light must be normal incident onto the measured object in order to fulfill the confocal condition. In the measurement, only the deviation of the object surface from the focal surface has to be detected, the maximum accessible profile depth is therefore considerably increased. Furthermore, it allows even faster measurements since the total vertical scan movement is reduced. One interesting application of confocal microscopy on curved surfaces is the testing of components with a complex shape in a

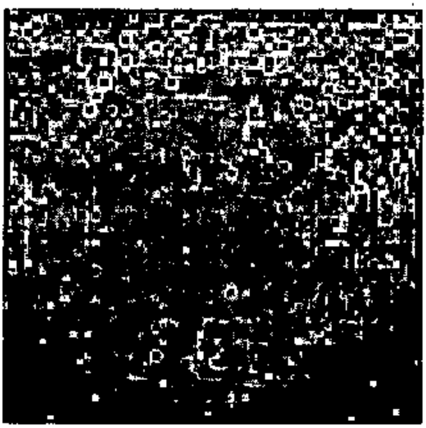

Fig. 5.7: Measured deviation of the lens array focal length distribution from the measured spherical object. The field size is 11 mm x 11 mm and the gray scale corresponds to a deviation of 0-11.8 mm.

manufacturing line. Arrays for focusing onto a cylindrical ($R = 20$ mm) and a spherical surface ($R = 52.44$ mm) have been designed and fabricated.

Results of confocal measurements [ITO] of a spherical plano-convex lens, having a radius of curvature of $R = (52.44 \pm 1.0)$ mm are shown in Fig. 5.7. The topography obtained from the confocal measurement (field size 11 mm x 11 mm) shows the difference between the focal spot distribution of the lens array and the object. An individual pixel in Fig. 5.7 corresponds to the response of one microlens aperture. For the plano-convex lens investigated, we found a residual deviation which lies within the manufacturing tolerances for this type of lens.

Chromatic behavior of lens arrays focusing onto a sphere

Diffractive lenses show strong chromatic aberrations, their Abbe number is given by $V_D = -3.45$ [Sto 88]. They are therefore mainly used with monochromatic or narrow bandwidth illumination. However, in some cases, we can take advantage from their strong chromatic aberration. Hutley et. al. [Hut 88] realized a distance sensor based on the chromatic aberration of a diffractive lens. Tiziani et. al. [Tiz 96] demonstrated for a confocal microscope as described in Section 5.1 that the z-scan of the object can be replaced by a scan of the illumination wavelength. This mechanical free scanning allows an even faster measurement. This is of great interest in time critical applications as in on-line inspection systems. In the following, we investigate the chromatic behavior of a microlens array focusing onto a sphere.

We use polar coordinates (r, θ, z). The focal length of the lens focusing on the sphere with radius R at position r is for $r << R$ given by (cf. Fig. 5.8):

$$f(r) = f_{\min} + R - \sqrt{R^2 - r^2} \approx f_{\min} + \frac{r^2}{2R} \tag{5.1}$$

The chromatic focal length behavior of one individual lens with focal length f_0 at wavelength λ_0 follows from Eq. 2.5:

$$f_1(\lambda) = \frac{\lambda_0}{\lambda} \cdot f_0 \, . \tag{5.2}$$

Inserting Eq. 5.2 into Eq. 5.1 gives a focal length distribution which is still spherical but has a new radius of curvature given by:

$$R_1(\lambda) = \frac{\lambda}{\lambda_0} R_0 , \tag{5.3}$$

and a new minimal distance $f_{min,2}$ given by Eq. 5.2. This situation is shown in Figure 5.8 for the two wavelengths λ_0 and $\lambda_1 > \lambda_0$.

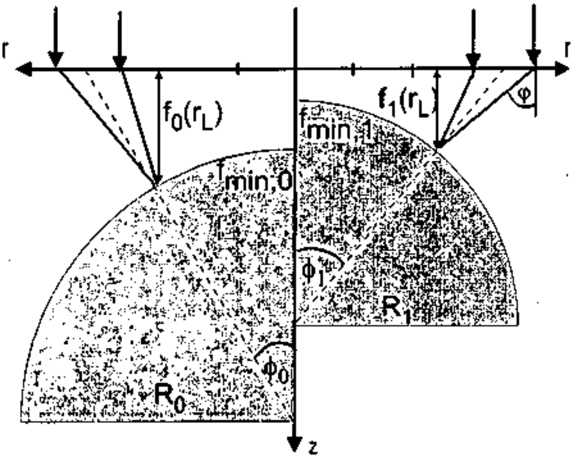

Fig. 5.8: Change of focal length distribution for illumination with the wavelength λ_0 (left) and for illumination with $\lambda_1 > \lambda_0$ (right).

Since the minimum distance f_{min} also changes with the wavelength, a chromatic scanning technique doesn't eliminate the need for a residual scan in the vertical direction without additional effort in the data analysis. However, a single lens array can be used to measure objects with different radii of curvature.

In practice, the high numerical aperture of the lenslets make the use of phase-matching numbers $M > 1$ desirable to ease the fabrication. This lowers the tolerances of the lenslets efficiency upon a wavelength change (cf. Eq. 3.3). For $M = 3$, an tolerable efficiency loss of 25% limits the wavelength range and therefore the change of the radius R to $\delta R/R = 0.1$. This measurement range can be extended by adequate calibration procedures [Tiz 96].

For the above derivation we used Eq. 5.2 which is strictly valid only for paraxial diffractive lenses. This condition is not fulfilled for the lenses investigated in Pub. IV. However, Eq. 5.2 is a good starting point to obtain a general understanding of the chromatic behavior of the lens array. For a nonparaxial lens, rays passing near the lens center will follow Eq. 5.2 whereas rays passing near the aperture edge will have a stronger chromatic aberration. This leads in addition to the focal length change given by Eq. 5.2 to an axial broadening δf of the focal position. This axial broadening δf is obtained with the grating equation to:

$$\delta f = \frac{\lambda_0}{\lambda} f_0 - \sqrt{\left(\frac{\lambda_0}{\lambda}\right)^2 \left(f_0{}^2 + a^2\right) - a^2} \,. \tag{5.4}$$

Note that the broadening δf scales with the lens aperture radius a for a given *NA* and becomes considerable for diffractive lenses with macroscopic apertures $a > 1$ mm. A similar focal broadening for diffractive non-paraxial lenses is found in the case of thermal expansion (cf. Chapter 2).

For the spherical focal length distribution of the lens array discussed above, a broadening of the focal distribution occurs additionally to the change of its radius of curvature. For parameters of the lens arrays investigated, ($a = 100$ µm, $f_{min} = 400$ µm), illumination with $\lambda = 1.2\,\lambda_0$ gives a maximum broadening of $\delta f = 4.6$ µm for the lenses with the highest *NA*. This is still below the diffraction limited axial extension of the focus which is 17 µm FWHM (cf. Eq. 6 in Pub. 1).

5.3 Lens arrays for optics in computing

Applications in information technology can profit considerably from micro-optical elements. For the laser to fiber coupling in optical transmission systems, the use of DOEs [Ros 95b] is an alternative to approaches based on butt-coupling [Nic 81] or ball lenses [Kar 88]. Microlens arrays are an important part of optical interconnect systems [Dho 95] which aim to overcome the limitations of low transmission rates in electronic computer bus systems.

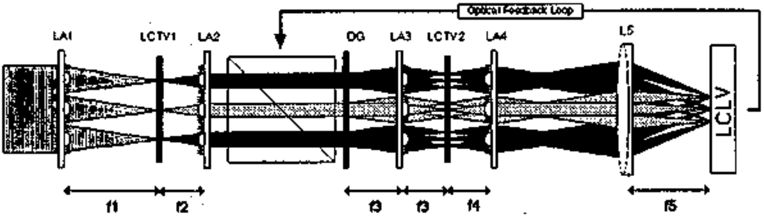

Fig. 5.9: Vector matrix multiplier for a neural network application [Ber 97a].

A system with a high optical complexity is currently being developed by Berger et. al. [Ber 97a]. The heart of this optically implemented asynchronous recurrent neural network is a reconfigurable interconnect which acts as vector matrix multiplier (cf. Fig. 5.9). It has a high degree of parallelism with its 16 x 16 channels and 65536 interconnections in total. This leads to a large image field of 17.5 x 17.5 mm^2. The main issue for the realization of the optical setup is to match each one of the 65536 fanned out laser beams to its individual pixel on the liquid crystal television (LCTV2). The use of microlens arrays offers the advantage that the input pixels are imaged in paraxial positions [Loh 91] eliminating the problem of field curvature and reducing the effect of lens aberrations [Loh 89]. This results in a more compact system design. However, in order to profit from these principal advantages, microlenses with an accurate focal spot pitch, diffraction limited performance, a high fill factor, high efficiency and a correct focal length are needed.

Table 5.1: Parameters of the lens arrays realized.

	f [mm]	NA	N	Λ_{min} [μm]	M	η [%]
A	11.5	0.05	53	7	2	64
B	50	0.011	12	31	1	74
C	80	0.007	8	50	1	72

For the application we designed and fabricated lens arrays (16 x 16, pitch p = 1092 μm) with three different focal lengths (cf. Table 5.1) for the use at different positions in the setup [Ber 97]. The array A was designed to work in the second diffraction order (M = 2) to ease the fabrication since the minimum local first order grating period Λ_{min} is only 7 μm. The other two types (B and C) had a rather low Fresnel number N, but still high enough to profit from the diffractive behavior and achieve a precise focal length (cf. Sec. 2.5). Our direct write technique is very well suited to fabricate such lens arrays with a low numerical aperture and with a high fill factor. The measured efficiencies (cf. Table 5.1) include the absorption of the photoresist (at λ = 488 nm) and the Fresnel losses at the three interfaces (air/glass, glass/photoresist, photoresist/air).

The lateral positioning of the focal spots in the image plane is extremely important for the application. To test it, the lens array was illuminated with a plane wave and the LCTV was placed in the focal plane. A transmission pattern was sent onto the LCTV, a camera placed behind. The resulting intensity distribution is shown in Fig. 5.10 for a replicated and a photoresist original array. For the replicated arrays (either UV-casting on a glass substrate or hot embossing in polycarbonate sheets), the individual foci are slightly displaced and do not hit the corresponding pixels of the LCTV. For the photoresist master, perfect alignment is obtained. We conclude that our standard replication process could not fulfill the demanding application requirements (maximum displacement of $\delta x < 10\ \mu m$ in the focal plane at $z = 50000\ \mu m$) over the whole area at that time.

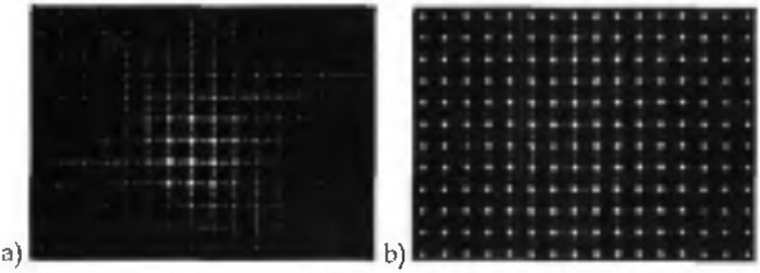

Fig. 5.10: Focal plane alignment of replicated array (a) and photoresist original (b) [Ber 97].

We measured the lens pitch of the Ni shim to $p = (1091.7 \pm 0.3)\ \mu m$, for the UV-casted replica to $p = (1091.7 \pm 0.3)\ \mu m$ and for the hot embossed replica to $p = (1083.9 \pm 0.4)\ \mu m$. For such critical applications the shrinkage of 0.74 % during the electroforming and hot embossing process can also be compensated for [Gal 97b].

However, the lateral displacement of the focal spot pattern is also observed for UV embossed replica and is due to a waviness of the shim introduced in the galvanic electroform process. A maximum lateral deviation in the focal plane of $\delta x = 10\ \mu m$ corresponds for plane wave illumination to a 200 nm tilt over one lens aperture of 1.0 mm. This flatness problem of the Ni-shims is also known in standard industrial replication processes and has meanwhile been significantly improved. As an alternative approach, the resist pattern was transferred into quartz by reactive ion etching (RIE). The resulting lens arrays did fulfill the positioning requirement and showed an increased efficiency (> 80 %), partly due to the reduced absorption losses. From these optically flat quartz masters, replicas can be obtained by UV casting.

The reconfigurable optical interconnect did profit enormously from the use of microlens arrays fulfilling the demanding tolerances. This results in a simpler alignment and eliminates the problem of field curvature, allowing a more compact overall system design.

5.4 Lens arrays for wavefront sensing

Interferometric wavefront measurement techniques are very well developed and allow a very precise measurement [Mal 78]. However, they require coherent light and a reference wavefront in most cases. In some applications it is of interest to measure non-coherent light or a reference wavefront cannot be generated.

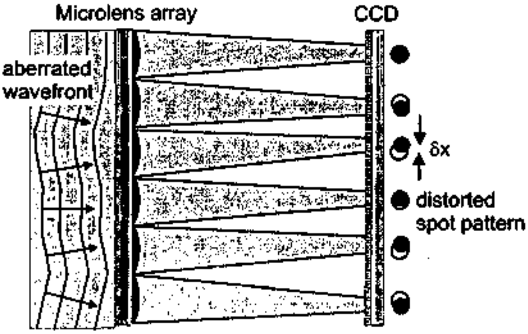

Fig. 5.11: Principle of a Shack-Hartmann wavefront sensor.

As an alternative to interferometric techniques, Shack-Hartmann wavefront sensors are used to sense e.g. atmospheric turbulence as input for adaptive optics in telescopes. For the optical characterization of fabricated elements, a Shack-Hartmann wavefront sensor was realized [Kus 96]. The working principle is sketched in Fig. 5.11. The heart of the sensor consists of a microlens array. An incident ideal plane wave leads to a regular pattern of focal points in the image plane. Aberrations in the incident wave lead to distortion δx of the focal point pattern. From these distortions δx, the wavefront slope over the microlens pupils is obtained and the wavefront shape is reconstructed. From the wavefront, the Seidel aberration coefficients can be obtained. The micro-lens array (22 x 22 lenslets, focal length $f = 40.5$ mm, semi-aperture $a = 447$ µm), was specially designed and fabricated for this purpose.

In order to obtain a high resolution of the measured wavefront, a long focal length and small subapertures are needed. On the CCD, several pixels should be illuminated so that the center of gravity (and thus the lateral shift δx (cf. Fig. 5.11)) can be determined with sub-pixel resolution. These requirements lead to lenses with low Fresnel numbers. For wavefront sensing in telescopes, we fabricated lens arrays with a very low Fresnel number (40 x 40 lenslets, $f = 40$ mm, semi-aperture $a = 125$ µm, $N = 0.6$) which are now in use in Shack-Hartmann sensors at the European Southern Observatory (ESO) in Chile and at the Imperial College of Science, Technology and Medicine, London, UK.

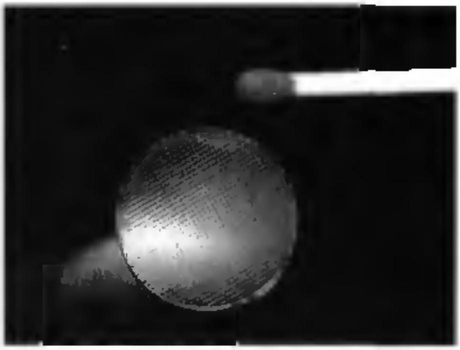

Fig. 5.12: The photo shows the lens array, replicated onto a circular glass substrate by UV-casting.

The Fresnel number of $N = 0.6$ means that the central zone was not fully used, the sag over the aperture is only 300 nm. A photograph of a replicated (UV-casting) sensor module is shown in Fig. 5.12. Direct write methods are well suited to fabricate such lens arrays with a very high efficiency since no profile steps are present. The tolerances of such low Fresnel number lenses upon etching errors were found to be very relaxed (cf. Pub. I and Sec. 2.5.1).

5.5 Diffractive lenses for astigmatism correction

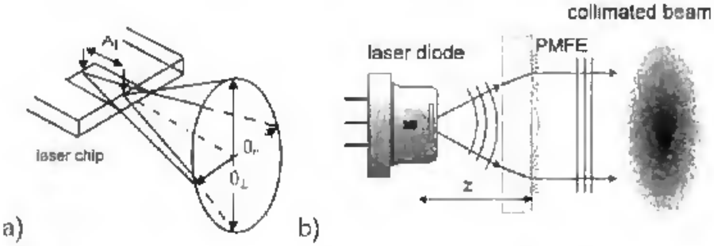

Fig. 5.13: Sketch of longitudinal astigmatism of semiconductor laser diodes (a) and of collimation setup with a diffractive lens (b).

The strongly asymmetric beam divergence angles in the horizontal and vertical planes of edge emitting semiconductor laser diodes are often not compatible with the requirements of the applications. Furthermore, these laser diodes often show a longitudinal astigmatism A_l as illustrated in Fig. 5.13. In most cases, the divergence angles and beam diameters have to be adjusted to appropriate values and the astigmatism to be corrected. Solutions based on classical optics, such as by using cylindrical lenses, tend to be bulky and expensive. The flexibility of the DOE approach allows collimation and longitudinal astigmatism correction to be performed with one single planar optical element [Hes 95]. This is achieved by an anamorphic element with two different focal lengths f and

$f + A_l$ in the two principal directions $\perp$ and $//$, taking into account the different geometrical source points of the emitted light.

Fig. 5.14: Images of the focused beam at different positions along the optical axis. Focused with a microscope objective (a) and an anamorphic diffractive lens (b).

Fig. 5.14 shows the spot diagram of a focused laser diode using a commercial microscope objective for different focal distances z. Due to the longitudinal astigmatism, the light has two focal planes. The same experiment (cf. Fig. 13), using an anamorphic DOE shows that the beam is now free of astigmatism, with only one focal plane.

The suitability of continuous-relief DOEs for low-cost replication techniques such as injection molding offers the promising prospect of combining the DOE with features to simplify the assembly of the complete system. Also, the DOE can be part of the housing itself, e.g. can incorporate a window function [Wie 95].

6. Conclusions

Diffractive optical elements can offer great advantages in many applications. They allow the realization of optical functions which are impossible or only difficult to realize with conventional refractive optics. This feature and their unique ability to combine different optical functions in one single element can simplify existing optical systems or can generate new fields of applications. However, a successful implementation of diffractive optical elements requires a detailed understanding of the design and fabrication process.

A new approach for the surface relief calculation of high numerical aperture lenses ($0.1 < NA < 0.5$) was presented. It combines the accuracy of existing phase-sensitive ray tracing methods with the simplicity of the widely used thin layer approximation. This results in a considerable simplification of the exposure data generation and allows the practical realization of new types of micro-optical elements with complex structures and high deflection angles.

Aperture diffraction effects, mainly neglected for bulk optical systems, can be important for micro-optical elements. We investigated the influence of aperture diffraction effects on the fabrication tolerances for refractive and diffractive lenslets. It was found that the diffraction at the aperture counterbalance the influence of etching errors. This results in relaxed fabrication tolerances.

It has been shown that direct laser beam writing is an attractive master generation technology for DOE fabrication. However, the resolution of this technology is limited by the finite size of the writing spot. The consequence is a reduction in diffraction efficiency for small periods. We successfully demonstrated robust optimization techniques which lead to considerable improvements in the diffraction efficiency. As typical example, an increase from 61 % to 79 % was achieved for a 10 μm grating.

To obtain the same improvement in diffraction efficiency with a non-optimized design would require half the writing spot size. The calculation of the diffraction efficiency of fabricated elements was related to the measurable writing spot size. This is an important tool for the component and system design.

Lens arrays for applications in parallel scanning confocal microscopy have shown excellent results. Replicated arrays have been fabricated by UV-embossing into a thin epoxy film on a glass substrate and by hot embossing into a flexible polycarbonate film. Fabricated laser written arrays with $NA = 0.28$ exhibit a very high uniformity in focal length and nearly diffraction limited axial response.

A new characterization technique, based upon a confocal microscope arrangement, was used to characterize the array performance. The technique has high resolution and the parallel sampling gives rapid access to array specific information such as the uniformity of the lenslets. It represents a very convenient approach for lens array characterization in general.

We demonstrated optical systems that require or benefit from microlens arrays with spatially variant optical properties. Direct laser beam writing has proven to be a flexible technology that guarantees a high-accuracy fabrication of refractive as well as diffractive lenses covering a large parameter range on one single substrate. It is capable to combine a high fill factor with the possibility to shape the focal surface of the lens array with very high accuracy. This is a valuable assessment for certain types of applications. The variation of focal length alone and in combination with a varying deflection angle was demonstrated for the application of confocal microscopy on curved surfaces.

References

[3DLtd] A company active in this field is 3D Limited, 6314 Unterägeri, Switzerland.

[Aag 97] H. Aagedal, F. Wyrowski, M. Schmid, J. Müller-Quade, and T. Beth, "Consequence of high resolution lithography for the design in the paraxial domain", EOS Topical Meeting Series 12, 166-167 (1997).

[Art 92] G. Artzner, "Microlens arrays for Shack-Hartmann wavefront sensors," Opt. Eng. 31, 1311 - 1322 (1992).

[Beh 93] G.P. Behrmann and J.P. Bowen, "Influence of temperature on diffractive lens performance," Appl. Opt. 32, 2483-2489 (1993).

[Ben 96] J. Bengtsson, "Kinoform-only Gaussian-to-rectangle beam shaper for a semiconductor laser," Appl. Opt. **35**, 3807-3814 (1996).

[Ber 97] Ch. Berger, N. Collings, R. Völkel, M. T Gale and Th. Hessler, "Advantages and Problems of Microlens Arrays in an Optical Neural Network Application", EOS Topical Meeting Digest Series 13, 115 - 120, 1997.

[Ber 97a] Ch. Berger, N. Collings, D. Gehringer, "Recurrent optical neural network for the study of pattern dynamics," in *Optical Information Science and Technology*, Proc. SPIE, Moscow 27-30.8.1997.

[Blo 97] C.G. Blough, M. Rossi, S.K. Mack, R.L. Michaels, "Single-point diamond turning and replication of visible and near-infrared diffractive optical elements," Appl. Opt. 36 , 4648-4654 (1997).

[Bor 80] M. Born, E. Wolf, *Principles of Optics*, p. 128, Pergamon Press (Oxford, 1980).

[Bow 94] J.P. Bowen, C.G. Blough, V. Wong, "Fabrication of optical surfaces by laser pattern generation," in OSA Topical Meetings Digest Series 13, 153-156 (1994).

[Bra 79] G.J. Brakenhoff, P. Blom and P. Barends, "Confocal scanning light microscopy with high aperture immersion lenses," J. Microsc. 117, 219 - 232, (1979).

[Bur 89] D.A. Buralli, G.M. Morris, "Optical performance of holographic kinoforms," Appl. Opt. 28, 976 - 983 (1989).

[Bur 92] D.A. Buralli, G.M. Morris, "Effects of diffraction efficiency on the modulation transfer function of diffractive lenses", Appl. Opt. 31, 4389-4396 (1992).

[Car 87] K. Carlson and N. Aslund, "Confocal imaging for 3D digital microscopy," Appl. Opt. **26**, 3232 - 3238 (1987).

[Car 94] E. Carcolé, J. Campos, I. Juvells, and S. Bosch, "Diffraction efficiency of low-resolution Fresnel encoded lenses," Appl. Opt. **33**, 6741-6746 (1994).

[Cox 91] J.A. Cox, B. Fritz, T. Werner, "Process error on binary optics performance," Proc. SPIE 1555, 80-88 (1991).

[Dal 90] D. Daly, R.F. Stevens, M.C. Hutley, and N. Davies, "The manufacture of microlenses by melting photo-resist", J. Meas. Sci. Techn. **1**, 759 - 766 (1990).

[Däs 95] W. Däschner, M. Larrson, and S.H. Lee, "Fabrication of monolithic diffractive optical elements by their use of e-beam direct write on an analog resist and a single chemically assisted ion-beam-etching step," Appl. Opt. 34, 2534-2539 (1995).

[Dho 95] B. Dhoet, P. de Dobbelaere, J. Blondelle, P. Van Daele, P. Demeester, and R. Baets, "Monolithic integration of diffractive lenses with LED-arrays for board-to-board free space optical interconnect," J. Lightwave Techn. **13**, 1065-1073 (1995).

[Ehb 95] P. Ehbets, M. Rossi, and H.P. Herzig, "Continuous-relief fan out elements with optimized fabrication tolerances," Opt. Eng. **34**, 3456 - 3464 (1995).

[Ekb 94] M. Ekberg, F. Nikolajeff, M. Larsson, and S. Hård, "Proximity-compensated blazed transmission grating manufacture with direct-writing, electron-beam lithography," Appl. Opt. 33, 103-107 (1994).

[Fak 95] D. Faklis, G.M. Morris, "Spectral properties of multiorder diffractive lenses," Appl. Opt. **34**, 2462 - 2468 (1995).

[Far 90] M.W. Farn, J.W. Goodman, "Effect of VLSI fabrication errors on kinoform efficiency," Proc SPIE **1211**, 125-136 (1990).

[Fin 95] J.M. Finland, K. M. Flood, R.J. Bojko, "Efficient f/1 binary-optics microlenses in fused silica designed using vector diffraction theory," Opt. Eng. **34**, 3560-3563 (1995)

[Fle 97] M. B. Fleming, M.C. Hutley, "Blazed diffractive optics," Appl. Opt. **36**, 4635 - 4643 (1997).

[Fuj 82] T. Fujita, H. Nishihara, J. Koyama, "Blazed gratings and Fresnel lenses fabricated by electron-beam lithography," Opt. Lett. **7**, 578-580 (1982).

[Fut 92] J. Futhey, M. Fleming, "Superzone diffractive lenses," OSA Tech. Dig. **9**, 4 (1992).

[Gal 83] M.T. Gale and K. Knop, "The fabrication of fine lens arrays by laser beam writing," Proc. SPIE **398**, 347-353 (1983).

[Gal 94] M.T. Gale, M. Rossi, J. Pedersen, and H. Schütz, "Fabrication of continuous-relief microoptical elements by direct laser writing in photoresist", Opt. Eng. **33**, 3556-3566 (1994)

[Gal 97] M.T. Gale, "Direct writing of continuous-relief elements," in: *Micro-Optics - Elements, Systems, and Applications*, H.P. Herzig, ed., (Taylor & Francis, London, 1997).

[Gal 97a] M.T. Gale, "Replication," in: *Micro-Optics - Elements, Systems, and Applications*, H.P. Herzig, ed., (Taylor & Francis, London, 1997).

[Gal 97b] M.T. Gale, J. Pedersen, H. Schütz, H. Povel, A. Gandorfer, P. Steiner, P.N. Bernasconi, "Active alignment of replicated microlens arrays on a charge-coupled device imager," Opt. Eng. 36, 1510-1517 (1997).

[Gas 78] J.D. Gaskill, *Linear Systems, Fourier Transforms and Optics* (Wiley, New York, 1978), Chap. 10.2.

[Ger 75] A. Gerrad, J.M. 8urch, *Introduction to matrix methods in optics,* (John Wiley & Sons, London, 1975) p. 117.

[Gol 96] M.A. Golub, M. Duparré, E. B. Kley, R. Kowarschik, B. Lüdge, W. Rockstroh, H.J. Fuchs "New diffractive beam shaper generated with the aid of e-beam lithography," Opt. Eng. 35, 1400-1406 (1996).

[Goo 96] J.W. Goodman, *Introduction into Fourier Optics,* 2^{nd} Ed., (McGraw-Hill, New York, 1996).

[Han 83] C.Y. Han, Y. Ishii, K. Murata, "Reshaping collimated laser beams with a Gaussian Profile to uniform profiles", Appl. Opt. 22, 3644 (1983).

[Hei 96] C. Heine, *Thin Film Coated Submicron Gratings: Theory, Design, Fabrication and Application,* Dissertation, University of Neuchâtel (Neuchâtel, 1996).

[Her 97] H.P. Herzig, "Design of refractive and diffractive micro-optics", in *Micro-Optics: Elements, Systems, and Applications,* H.P. Herzig, ed. (Taylor & Francis, London, 1997).

[Hes 95] Th. Hessler, M. Rossi, R.E. Kunz; "Diffractive optical elements for laser diodes," Tech. Digest Workshop on Diffractive Optics, Prague, pp. 52-53 (1995).

[Hes 97] Th. Hessler and M. Rossi, "Design and fabrication aspects of continuous relief diffractive optical elements"; in *Diffractive Optics and Optical Microsystems,* S. Martelucci and E. Chester, eds (Plenum Press, New York, 1997) pp. 139-148.

[Hut 82] M.C. Hutley, *Diffraction Gratings,* (Academic Press, London, 1982), p. 49.

[Hut 88] M.C. Hutley, R.F. Stevens, "The use of a zone-plate monochromator as a displacement transducer," J. Phys. E: Sci. Instrum. 21, 1037-1044 (1988).

[Hut 91] M.C. Hutley, D. Daly, R.F. Stevens, "The Testing of Microlens Arrays," IOP Short Meeting Series 30, 67-81 (1991).

[Hut 96] M.C. Hutley, R.A. Hunt, K. Khand, D. Daly, R.F. Stevens, "The use of a series of lens arrays to match optical arrays of different pitch," EOS Topical Meeting Digest Series 9, 66-67 (1996).

[ITO] The confocal microscopy measurements were performed by the "Institut für Technische Optik", at the University of Stuttgart, Germany.

[Jam 81] T.H. Jamieson, "Thermal effects in optical systems", Opt. Eng. 20, 156 - 160 (1981).

[Jun 96] D. Juncker, Master Thesis, University of Neuchâtel (1996).

[Kar 88] H. Karstensens, "Laser diode to single-mode fibre coupling with ball lenses," J. Opt. Commun. 9, 42-49 (1988).

[Kat 95] A.D. Kathman, D.H. Hochmuth, D.R. Brown, "Efficiency considerations for diffractive optical elements," Proc. SPIE 2577, 114-122 (1995)

[Kor 95] V. P. Koronkevich, V.P. Kiryanov, V.P. Korol'kov, A. G. Poleshchuk, V.V. Cherkashin, E.G. Churin, A.A. Kharissov, "Fabrication of diffractive optical elements by direct laser-writing with circular scanning", in: *Digital Image Processing and Computer Graphics*, N.A. Kuznetsov, V. A. Soifer, eds., Proc. SPIE 2363, pp. 290-297 (1995).

[Kui 95] M. Kuittinen, H.P. Herzig, and P. Ehbets, "Improvements in diffraction efficiency of gratings and microlenses with continuous relief structures," Opt. Commun. **120**, 230-234 (1995).

[Kun 93] R.E. Kunz and M. Rossi, "Phase-matched Fresnel elements", Opt. Commun. **97**, 6 - 9 (1993).

[Kun 97] R.E. Kunz, "Miniature integrated optical modules for chemical and biochemical sensing," Sensors and Actuators B **38-39**, 13-28 (1997).

[Kus 96] M. Kuster, "Shack-Hartmann Wellenfront sensor," Diploma Thesis, Neu-Technikum Buchs, Buchs, Switzerland (1996).

[Lan 92] P. Langlois, H. Jerominek, L. Leclerc, J. Pan, "Diffractive optical elements fabricated by laser direct writing and other techniques," Proc. SPIE **1751**, 2-12 (1992).

[Lar 94] M. Larrson, M. Ekberg, F. Nikolajeff, and S. Hård, "Successive development optimization of resist kinoforms manufactured with direct-writing, electron-beam lithography", Appl. Opt. **33**, 1176-1179 (1994).

[Lee 78] W.H. Lee, "Computer-generated holograms: Techniques and Applications" in *Progress in Optics* Vol. XVI, (E. Wolf, ed.) pp. 119 - 232 (1978).

[Leg 97] J.R. Leger, "Design considerations for high *f*/number diffractive optics," Talk ThK1, OSA Annual Meeting (Long Beach, 1997).

[Li 81] Y. Li and E. Wolf, "Focal shifts in diffracted converging spherical waves," Opt. Comm. **39**, 211 - 215 (1981).

[Li 84] Y. Li and E. Wolf, "Three-dimensional intensity distribution near the focus in systems of different Fresnel numbers," J. Opt. Soc. Am. A **1**, 801 - 808 (1984).

[Loh 89] A.W. Lohmann, "Scaling law for lens systems," Appl. Opt. **28**, 4996-4998 (1989).

[Loh 91] A.W. Lohmann, "Image formation of dilute arrays for optical information processing," Opt. Commun. **86**, 365-370 (1991).

[Mag 78] R. Magnusson, T.K. Gaylord, "Diffraction efficiencies of thin phase gratings with arbitrary grating shape," J. Opt. Soc. Am. **68**, 806 - 809 (1978).

[Mal 78] D. Malacara (ed.), *Optical shop testing*, (Wiley and Sons, New York, 1978).

[Mar 90] J.C. Marron, D.K. Angell, and A.M. Tai, "Higher-Order Kinoforms", Proc. SPIE **1211** Computer and Optically Formed Holographic Optics, 62 - 66 (1990).

[Nic 81] A. Nicia, "Lens coupling in fibre-optic devices: efficiency limits", Appl. Opt. **20**, 3136-3145 (1981).

[Nik 95] F. Nikolajeff, J. Bengtsson, M. Larrson, M. Ekberg, and S. Hård, "Measuring and modeling the proximity effect in direct-write electron-beam lithography kinoforms," Appl. Opt. **34**, 897-903 (1994).

[Nik 97] F. Nikolajeff, *Diffractive Optical Elements: Fabrication, Replication , and Applications and Optical Properties of a Visual Field Test,* Dissertation, Chalmers University of Technology (Göteborg, 1997).

[Nis 87] H Nisihara T. Suhara, "Micro Fresnel Lenses", in *Progress in Optics* Vol. XXVI, (E. Wolf, ed.) 1 - 38 (1987).

[Nop 93] E. Noponen, J. Turunen, A. Vasara, "Electromagnetic theory and design of diffractive-lens arrays", J. Opt. Soc. Am. A **10**, 434 - 443 (1993).

[NPL] See the conferences on Microlens Arrays at the NPL , Teddington, UK in 1993: IOP Short Meetings on Microlens Arrays, National Physical Laboratory, Teddington , UK (1993), in 1995: Microlens arrays, EOS Topical Meeting Digest Series **5**, (1995) and in 1997: Microlens arrays, EOS Topical Meeting Digest Series 13, (1997).

[Opp 95] Y. Opplinger, P. Sixt, J.M. Stauffer, P. Regnault, G. Voirin, "One-step 3D shaping using a gray-tone mask for optical and microelectronic applications," Microelectronic Eng. **23**, 449-454 (1995).

[OSh 95] D.C. O'Shea, W.S. Rockward, "Gray-scale masks for diffractive-optics fabrication: II. Spatially filtered halftone screens," Appl. Opt. **34**, 7518-7526 (1995).

[Phi] Philips Competence Centre Plastic B.V., Optical Components, Eindhoven, The Netherlands.

[Pom 94] D.A. Pommet, M.G. Moharan, E.B. Grann, "Limits of scalar diffraction theory for diffractive phase elements", J. Opt. Soc. Am. A **11**, 1827 - 1834 (1994).

[Rei 97] K. Reimer, H.J. Quenzer, M. Jürss, B. Wagner, "Micro-optic fabrication using one-level gray-tone lithography," in *Miniaturized Systems with Micro-Optics and Micromechanics II,* M. Edward Motamedi; L.J. Hornbeck; K.S. Pister; eds, Proc. SPIE **3008**, 279-288, (1997).

[Res 91] E. J. Restall, B. Robertson, M.R. Taghizadeh, and A.C. Walker, "Holographic microlens arrays as spatially variant optical interconnects," IOP Short Meeting Series **30**, 83-89 (1991).

[Rho 80] P.W. Rhodes, D.L. Shealy ,"Refractive optical systems for irradiance redistribution of collimated radiation: their design and analysis", Appl. Opt. **20**, 3545-3553 (1980).

[Rho 80] P.W. Rhodes, D.L. Shealy, "Refractive optical systems for irradiance redistribution of collimated radiation: their design and analysis", Appl. Opt. **20**, 3545-3553 (1980).

[Ric 93] D.W. Ricks, "Scattering from diffractive optics," in *Diffractive and Miniaturized Optics,* SPIE Critical Reviews of Optical Science and Technology,CR49, S.H. Lee; ed., pp. 187-211 (1993).

[Ron 95] R.L. Roncone, D.W. Sweeney, "Cancellation of material dispersion in harmonic diffractive lenses", Proc. SPIE Vol. 2404, Diffractive and Holographic Optics Technology II, Ivan Cindrich; Sing H. Lee; Eds, p. 81-88 (1995).

[Ros 93] R.E. Kunz, M. Rossi, "Phase-matched Fresnel elements," Opt. Commun. 97, 6-10 (1993).

[Ros 95] M. Rossi, R.E. Kunz, and H.P. Herzig, "Refractive and diffractive properties of planar micro-optical elements," Appl. Opt. 34, 5996 - 6007 (1995).

[Ros 95a] M. Rossi, "Phase-matched optical Fresnel elements", Dissertation, University of Neuchâtel (1995).

[Ros 95b] M. Rossi, G.L. Bona, and R.E. Kunz, "Arrays of anamorphic phase-matched Fresnel elements for diode-to-fiber coupling," Appl. Opt. 34, 2483-2488 (1995).

[Ros 96] M. Rossi, C.G. Blough, D.H. Raguin, E. K. Popov and D. Maystre, "Diffraction efficiency of high-NA continuous-relief diffractive lenses," in *Diffractive Optics and Micro-Optics*, Vol. 5, OSA Technical Digest Series, 233 - 236 (1996).

[Ros 97] M. Rossi, Th. Hessler and M.T. Gale, "Design and Fabrication of Micro-Optical Elements with Deep Relief Structures," in Vol. 12 of EOS Topical Meeting Digest Series (European Optical Society, Orsay, France,1997), pp. 68 - 69.

[Ros 97] M. Rossi, Th. Hessler and M.T. Gale, "Design and Fabrication of Micro-Optical Elements with Deep Relief Structures," in Vol. 12 of EOS Topical Meeting Digest Series (European Optical Society, Orsay, France,1997), pp. 68-69.

[Saa 94] J. Saarinen, S. Honkanen, S.I. Najafi, and J. Huttunen, "Double-ion-exchange process in glass for the fabrication of computer-generated waveguide holograms," Appl. Opt. 33, 3353-3359 (1994).

[Sch 95] J. Schwider, O. Falkenstörfer, "Twyman-Green interferometer for testing micro-spheres," EOS Topical Meeting Digest Series 5, 60-64 (1995).

[Sch 97] H. Schwarzer, S. Teiwes, and F. Wyrowski, "Non-pixelated design of computer-generated diffractive elements for increased diffraction efficiency", EOS Topical Meeting Series 12, 164-165 (1997).

[Sch 97a] J. Schwider, H. Sickinger, "Arraytests for Microlenses," Submitted to Optik (1997).

[Sin 95] S. Sinzinger and M. Testorf, "Transition between diffractive and refractive micro-optical components," Appl. Opt. 34, 5970 (1995).

[Ste 97] M.B. Stern, "Binary optics fabrication," in: *Micro-Optics - Elements, Systems, and Applications*, H.P. Herzig, ed., (Taylor & Francis, London, 1997).

[Sto 88] T. Stone, N. George, "Hybrid diffractive -refractive lenses and achromats," Appl. Opt. 27, 2960-2971 (1988).

[Sul 95] T.J. Suleski, D.C. O'Shea, "Gray-scale masks for diffractive-optics fabrication: I. Commercial slide imagers," Appl. Opt. 34, 7507-7517 (1995).

[Swa 91] G.J. Swanson, "Binary optics technology: Theoretical limitations on the diffraction efficiency of multilevel diffractive optical elements", *MIT Technical Report* 914 (1991).

[Swe 77] W. C. Sweatt, "Describing holographic optical elements as lenses," J. Opt. Soc. Am. 67, 803 - 808 (1977).

[Swe 95] D.W. Sweeney, G.E Sommargen, "Harmonic diffractive lenses" , Appl. Opt. 34, 2469 (1995).

[Tiz 94] H.J. Tiziani and H.M. Uhde, "Three-dimensional analysis by a microlens-array confocal arrangement," Appl. Opt. 33, 567-572 (1994).

[Tiz 96] H.J. Tiziani, R. Achi, and R.N. Krämer, "Chromatic confocal microscopy with microlenses," J. Mod. Optics 43, 155-163 (1996).

[Tsc 95] T. Tschudi, L. Wang, J.M. Aasfour, and B. Goebel, "Collimation of semiconductor laser beams by means of computer generated holograms", Technical Dig. Workshop on Diffractive Optics, Prague, p. 6, (1995).

[Völ 95] R. Völkel, Ph. Nussbaum, H.P. Herzig, R. Dändliker, and W.B. Hugle, "Microlens arrays for optical lithography", EOS Topical Meeting Digest Series 5, 100 - 105 (1995).

[Völ 97] R. Völkel, H.P. Herzig, Ph. Nussbaum, P. Blattner, R. Dändliker, E. Cullmann, and W. B. Hugle, "Microlens lithography and smart masks", Microelectronic Engineering 35, 513-516 (1997).

[Wie 95] D. Wieser, K. Müller, M. Allemann, F. Bishof, M.T. Gale and Th. Hessler, "Passiver Infrarot-Einbruchdetektor und dessen Verwendung", European Patent No. 95117323.6-2215.

[Wil 84] T. Wilson and C. Sheppard, *Theory and Practice of Scanning Optical Microscopy*, (Academic Press, London, 1984).

[Yoo 96] G.Y. Yoon, T. Jitsuno, M Nakatsuka, and S. Nakai, "Shack Hartmann wave-front measurement with large F-number plastic microlens array," Appl. Opt. 35, 188 - 192 (1996).

Abstract of Publications I - IV

Publication I

Relaxed fabrication tolerances for low Fresnel number lenses

Thomas Hessler and Rino E. Kunz

Numerical simulations have been performed to study the influence of resist developing errors on continuous relief microlenses. For very low Fresnel numbers (N < 4) the focal shift counteracts changes in the radius of curvature due to the depth errors and stabilizes the focal length. For higher Fresnel numbers (N > 2), the focal length is essentially determined by the diffraction at the lateral pattern of the segments, and deviations from the ideal blaze influence only the efficiency. A qualitative picture based on Fourier optics is given to explain these markedly relaxed tolerances with respect to depth errors for planar optical elements even for low Fresnel numbers.

Publication II

Analysis and optimization of fabrication of continuous-relief diffractive optical elements

Thomas Hessler, Markus Rossi, Rino E. Kunz, and Michael T. Gale

The fabrication of continuous-relief diffractive optical elements by direct laser beam writing in photoresist is analyzed. The main limitation and tolerances are identified and their influence on the optical performance are quantified. Fabricated structures show rounded profile steps resulting from the convolution of the desired profile with the writing beam. This leads to a reduction of the diffraction efficiency. Optimization techniques are presented to minimize this effect. Scaling the profile depth by a factor $\mu > 1$ increases the first order diffraction efficiency for blazed elements. This method is also applied to suppress the zeroth diffraction order in computer generated holograms. A nonlinear compensation of the exposure data for the Gaussian beam convolution resulted in an 18 % increase of the diffraction efficiency for a blazed grating with a period 10 μm to a value of 79 %.

Publication III

Microlens arrays for confocal microscopy

H.J. Tiziani, R. Achi and R.N. Krämer, T. Hessler, M.T. Gale, M. Rossi and R.E. Kunz

A new, high resolution measuring system based on confocal microscopy has been developed for the evaluation of microlens arrays, in particular for applications in confocal microscopy itself. Lenslet arrays for parallel scanning and processing in confocal microscopy were designed as phase-matched Fresnel lenslets and fabricated by direct laser writing. Replica arrays were produced by uv-embossing and hot embossing techniques. Fabricated arrays with a numerical aperture of 0.28 exhibited near diffraction limited performance and a focal length standard deviation of 120 nm in a nominal value of 250 µm. The technique developed represents a convenient and powerful technique for the characterisation of lenslet arrays in general.

Publication IV

Microlens arrays with spatial variation of the optical functions

Th. Hessler, M. Rossi, J. Pedersen, M.T. Gale, M. Wegner*, D. Steudle* and H.J. Tiziani*

Direct laser beam writing is a mature technology for the fabrication of continuous-relief micro-optical (diffractive and refractive) lenses and lens arrays having a wide range of different optical design parameters. Whereas most microlens array applications require only one specific element type, some applications can profit from the combination of micro-optical elements having different optical functions in the same array. Lens arrays with a spatial variation of the focal length and beam deflection angle have been fabricated and successfully tested in confocal microscope measurements on non-planar surfaces.

Publication I

Relaxed fabrication tolerances for low-Fresnel-number lenses

Thomas Hessler and Rino E. Kunz

Paul Scherrer Institute, Badenerstrasse 569, 8048 Zurich, Switzerland

Received September 5, 1996; revised manuscript received January 29, 1997; accepted January 29, 1997

Numerical simulations have been performed to study the influence of resist-developing errors on continuous-relief microlenses. For very low Fresnel numbers ($N < 4$), the focal shift counteracts changes in the radius of curvature that are due to the depth errors and stabilizes the focal length. For higher Fresnel numbers ($N > 2$), the focal length is essentially determined by the diffraction at the lateral pattern of the segments, and deviations from the ideal blaze influence only the efficiency. A qualitative picture based on Fourier optics is given to explain these markedly relaxed tolerances with respect to depth errors for planar optical elements and even for low Fresnel numbers. © 1997 Optical Society of America [S0740-3232(97)00307-4]

Key words: Micro-optics, diffraction, fabrication tolerances, low-Fresnel-number lenses.

1. INTRODUCTION

Improvements in microfabrication techniques during recent years allowed the fabrication of lenses with very-small-aperture radii well below 1 mm,[1] often arranged in an array. For such lenses, aperture diffraction effects can be of considerable importance. A suitable parameter for describing the aperture diffraction effects is the Fresnel number N of the lens, which is defined as[2]

$$N = \frac{a^2}{\lambda f}, \tag{1}$$

where f is the geometric optical focal length; λ, the wavelength; and a, the lens aperture radius. Expressed in terms of the lens f-number $F = f/2a$, it is given by $N = a/(2\lambda F)$. It describes the maximum phase deviation from a plane wave in units of $\lambda/2$ over the aperture; i.e., N is twice the number of Fresnel zones for a 2π zone lens. The importance of aperture diffraction effects increases with decreasing N. Typically a large f-number or a small aperture leads to a low N. Recently, microlenses with an aperture as low as 3 μm have been fabricated,[1] giving a low N even for very small f-numbers. A field of application for low-Fresnel-number lenses and the motivation for this study is their use in lens arrays for Shack–Hartmann wave-front sensing.[3] These lenses typically have a small aperture (e.g., a = 125–250 μm) and a large f-number (e.g., F = 45–160) at the same time.

In this paper we investigate the profile-relief tolerances of coherently illuminated lenses having Fresnel numbers below 10 with respect to fabrication errors and compare two coding schemes. The phase function of an optical element such as a lens can in principle be coded into a surface profile in two ways: as a thin surface relief,[4] where the phase function is wrapped to an interval between zero and integer multiples of 2π [Fig. 1(a)]; or as a profile without phase steps, as shown in Fig. 1(b). Such phase-wrapped elements are often simply referred to as diffractive; non-phase-wrapped elements, as refractive. We use the terms diffractive lens and refractive lens below to refer to elements obtained by these two coding schemes. Diffractive elements are usually fabricated by lithographic methods as a stepwise approximation by multiple mask exposure or by direct-write methods such as e-beam writing,[5] laser writing,[6] and diamond turning[7] as continuous profile. Refractive elements are in general fabricated as a continuous profile by, e.g., resist reflow methods[8] or for low Fresnel numbers, also by direct-writing methods.

For low numerical aperture, the optical performance of ideally fabricated elements illuminated at the design wavelength is, within the scalar theory, independent of the coding scheme. Differences in the performance become relevant when the elements are operated away from their design parameters.[9,10] For fabrication methods such as direct laser writing into photoresist,[6,11] the depth control during the developing process is one of the most critical points. In this study we focus on the influence of depth errors on the focal length of diffractive and refractive lenses with a continuous profile.

In the limit of high Fresnel numbers, when many segments are illuminated, the differences in the performance are well known. The angular spectrum of the transmitted light of a continuous-relief diffractive lens is governed by the diffraction at the pattern given by the segment boundaries. The refraction at the blazed profile determines the energy distribution within the allowed, sharply defined diffraction orders. Deviations from the ideal relief profile depth will not affect the angular spectrum, but the energy will be redistributed among the individual orders (f, $f/2$, $f/3$,...), as shown in Fig. 2(a). The function of a refractive lens with high N is based on the refraction at the curved interface. Hence depth errors will shift the focus position from f to $\bar{f}$ [Fig. 2(b)], but the energy in the focus will remain nearly constant.

For low Fresnel numbers, diffraction effects have to be taken into account to describe the performance for both diffractive and refractive lenses.[12] The performance of low-N refractive lenses in the presence of relief depth errors is governed by the combined effects of the refraction

0740-3232/97/0701599-08$10.00   © 1997 Optical Society of America

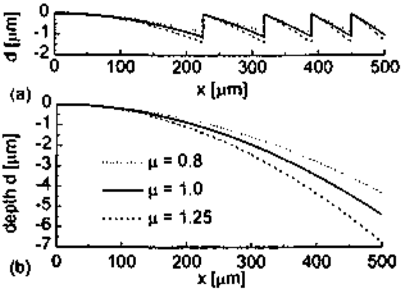

Fig. 1. Surface-relief profile of (a) the diffractive lens and (b) the refractive lens investigated ($f = 40$ mm). The surface profile of the depth-scaled lenses (depth scaling μ) is indicated by the dotted and the dashed curves.

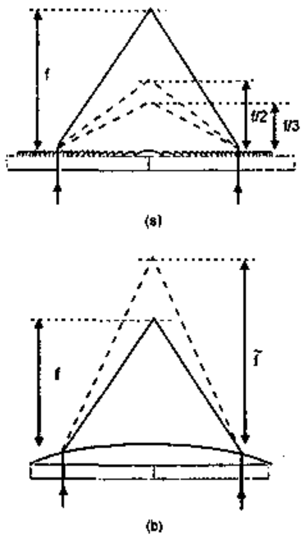

Fig. 2. Optical performance of depth-scaled lenses for high N: (a) diffractive, (b) refractive.

at the deformed profile and of the diffraction at the aperture. For diffractive lenses with low N, which have only a very low number of segments, the angular spectrum of the diffraction orders is broadened, and the refraction at the continuous profile becomes more influential.

After briefly recalling the properties of low-Fresnel-number lenses, we investigate the focal-length dependence of diffractive and refractive lenses on depth errors for varying Fresnel numbers. In the second part of this study we derive analytical expressions for illustrating the numerical results that we obtained for diffractive lenses.

2. LOW-FRESNEL-NUMBER LENSES

For low N ($N < 10$), the light distribution in the focal volume differs significantly from what one expects from the classical Debye theory[12] because of diffraction effects at the aperture. The distribution becomes asymmetric along the optical axis, and the focal position, defined as the point of maximum on-axis intensity, shifts away from its geometric optical value toward the aperture. It is possible to redesign the lens shape by increasing its geometric focal length to compensate the effect of the focal shift and to obtain the maximum on-axis intensity in the desired plane. The redesigned lens has a lower Fresnel number and therefore a broader and more asymmetric on-axis light distribution. As a consequence, it has a lower intensity in the desired plane than in the uncorrected case.[13] This variation of the magnitude of the focal shift with the refocusing is important for the focal-length variation of depth-scaled lenses, as is shown below.

3. ANALYTICAL TREATMENT OF A REFRACTIVE LENS

First, we derive an analytical expression for the on-axis irradiance distribution of a depth-scaled low-Fresnel-number refractive lens with a circular aperture. In the paraxial approximation, assuming that $R \gg x$, the depth profile of a refractive, spherical lens can be described by

$$d(x) = d_0 + R - \sqrt{R^2 - x^2} \approx d_0 - \frac{x^2}{2R}, \tag{2}$$

where R is the radius of curvature of the lens; d_0, a depth offset; and x, the radial coordinate of the lens. An etching error, typically resulting from variations in development of the exposed resist, leads to a nonideal depth profile

$$\tilde{d}(x) = \mu d(x), \tag{3}$$

where μ is the depth scaling factor, with $\mu = 1$ corresponding to the ideal case (Fig. 1).

We express the depth $\tilde{d}$ of the depth-scaled lens in terms of a modified radius of curvature $\tilde{R}$ according to relation (2) as

$$\tilde{d}(x) \approx \tilde{d}_0 - \frac{x^2}{2\tilde{R}}. \tag{4}$$

This leads to $\tilde{d}_0 = \mu d_0$ and to $\tilde{R} = R/\mu$ for the modified radius of curvature $\tilde{R}$ of the scaled lens. Hence a focal length

$$\tilde{f} = f/\mu \tag{5}$$

for the depth-scaled lens is obtained from the lens equation.

The on-axis intensity ($x = 0$, $y = 0$) of a spherical wave, diffracted at a circular aperture, is given by[12]

$$I(u_N) = I_0\left(1 - \frac{u_N}{2\pi N}\right)^2 \operatorname{sinc}^2(u_N), \tag{6}$$

with the variable

$$u_N = \frac{N}{2}\frac{\Delta z}{\Delta z + f} \tag{6a}$$

and $\Delta z = z - f$, which places the origin of the coordinate u_N to the geometric focus f. I_0 gives the intensity at the geometric focal point, and we write it, for purposes explained below, without using the amplitude factor A of Ref. 12 in terms of a and f as

$$I_0 = \left(\frac{\pi a^2}{\lambda f}\right)^2. \tag{6b}$$

We have seen in Eq. (5) that a depth-scaled lens can be regarded as a lens with a modified focal length $\bar{f}$. Hence on the basis of Eq. (6) we obtain the following equation for the on-axis intensity for the depth-scaled lens:

$$\bar{I}(\bar{u}_N) = \tilde{I}_0\left(1 - \frac{\bar{u}_N}{2\pi\bar{N}}\right)^2 \operatorname{sinc}^2(\bar{u}_N), \tag{7}$$

with

$$\tilde{I}_0 = \left(\frac{\pi a^2}{\lambda\bar{f}}\right)^2, \tag{7a}$$

using a modified Fresnel number $\bar{N} = \mu N$ and a changed coordinate $\bar{u}_N$ to relate the diffraction pattern of the scaled lens to the coordinate system of the geometric focus of the unscaled lens:

$$\bar{u}_N = \frac{\bar{N}}{2}\frac{\Delta\bar{z}}{\Delta\bar{z} + \bar{f}}, \tag{7b}$$

with $\Delta\bar{z} = z - \tilde{f}$. To relate the coordinate origin to the optical axis $z = 0$, we express the variable $\bar{u}_N$ in terms of z and μ:

$$\bar{u}_N(z, \mu) = \frac{\mu N}{2}\frac{z - (f/\mu)}{z}. \tag{8}$$

Equations (7) can now be written in terms of the depth-scaling factor μ and the z coordinate, with a prefactor independent of the depth scaling:

$$\tilde{I}(z, \mu) = \left(\frac{f\pi N}{z}\right)^2 \operatorname{sinc}^2\left[\frac{N}{2}\left(\frac{f}{z} - \mu\right)\right]. \tag{9}$$

The prefactor contains the Fresnel number N of the unscaled lens and accounts for the asymmetry and the focal shift for low values of N. The depth scaling shifts the sinc function along the optical axis. We define the focal length $f(N, \mu)$ as the position $z_{\max}$ at which the on-axis intensity $\tilde{I}(z, \mu)$ is at a maximum. For large N the width of the sinc function is narrow, and the focal length is given by Eq. (5).

4. NUMERICAL SIMULATION METHOD

The diffraction pattern of the lenses are obtained by numerical evaluation of the Rayleigh–Sommerfeld diffraction formulas[14]:

$$u_2(x, y) = \iint_{-\infty}^{\infty} u_1(x_e, y_e)\left(\frac{z_{12}}{i\lambda r_{12}^2}\right)\exp(ikr_{12})\mathrm{d}x_e\mathrm{d}y_e. \tag{10}$$

We calculate the complex-amplitude distribution $u_1(x_e, y_e)$ in the tangential plane (x_e, y_e) to the surface relief by phase-sensitive ray tracing through the microstructure, thus taking into account the phase shift of the surface relief and the refraction of the rays at the curved surface. With this approach, effects due to the finite depth of the surface relief are included within the validity of the scalar theory.[9] For the simulation of the resist-developing errors, the surface profile has been deformed according to Eq. (3).

5. RESULTS

We calculated the intensity distributions for diffractive and refractive lenslets with circular aperture versus the Fresnel number. The Fresnel number was changed from $N = 0.5$ to $N = 9.88$ by variation of the aperture radius from $a = 112\ \mu\text{m}$ to $a = 500\ \mu\text{m}$. For the simulation, we used the parameters of lenses that we fabricated for a Shack–Hartmann wave-front sensor with $f = 40$ mm, $\lambda = 0.633\ \mu\text{m}$ (He–Ne laser) and a refractive index of $n = 1.58$ (polycarbonate). The aperture of the fabricated lenses is $a = 125\ \mu\text{m}$, leading to $N = 0.62$.

A. Refractive Lens

For a refractive lens, the resulting focal length $f(N, \mu)$ obtained from Eq. (9) is plotted versus the Fresnel number N for three different depth-scaling factors, $\mu = 0.8$, $\mu = 1.0$, and $\mu = 1.25$, in Fig. 3. We used these rather high depth-scaling factors to emphasize their effects. In the fabrication process the depth errors are typically below 5%. Calculations were carried out for various depth-scaling factors μ, and a nearly linear dependence of their effects with the depth scaling was found. The on-axis intensity distributions were also calculated by the numerical method described above. The obtained positions of maximum intensity are plotted as symbols in Fig. 3 and are in excellent agreement with the analytical results.

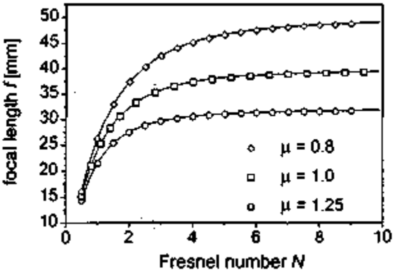

Fig. 3. Influence of depth scaling on the focal length for different Fresnel numbers (of the unscaled lens) for a refractive design. The solid curves are obtained by evaluation of the maximum of Eq. (9), and the data denoted by the symbols are obtained by the numerical simulation method.

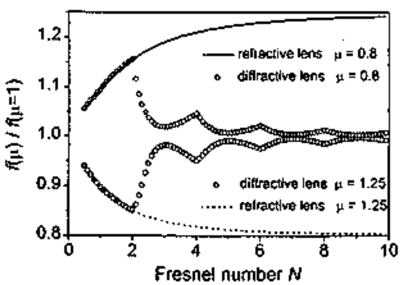

Fig. 4. Normalized focal-length change resulting from the etching errors for a diffractive and a refractive design. For the diffractive lens, the stabilization of the focal length due to diffraction comes into play with the illumination of the second zone.

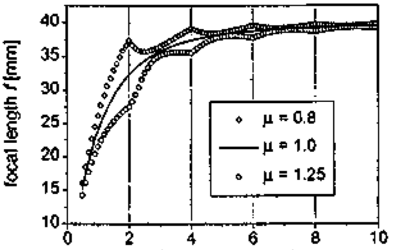

Fig. 5. Influence of depth scaling on the focal length for different Fresnel numbers for a diffractive design.

The focal length for the unscaled, refractive lens $f(N, \mu = 1.0)$ decreases for decreasing N because of the focal shift discussed above. This aperture diffraction effect is independent of the way in which the lens phase function is coded. For $N > 10$, the focal length approaches the design value of 40 mm. The focal length of the depth-scaled lenses ($\mu \neq 1$) approaches the value given by Eq. (5) for high N. This is the behavior expected for a refractive lens with high N.

For low N, the dependence of the focal length on the depth errors decreases. This is clearly indicated in Fig. 4, where the relative focal-length change $f(N, \mu)/f(N, 1)$ of the refractive lens is plotted as the solid ($\mu = 0.8$) and the dashed ($\mu = 1.25$) curves. The symbols in Fig. 4 refer to the case of the diffractive design and are discussed in the next paragraph. The reduced depth tolerance for low N can be explained as follows. The depth-scaled, refractive lens can be thought of as being a lens with a scaled focal length. The Fresnel number of this lens therefore changes to $\tilde{N} = \mu N$. For $\mu < 1$, the focal length increases because of the etching error [Eq. (5)], but the Fresnel number decreases, and the focal shift of the scaled lens is more pronounced. It counteracts the focal-length change resulting from the change of the radius of curvature. For $\mu > 1$, the geometric focal length decreases, but the Fresnel number increases. The focal shift is less pronounced and counteracts the focal-length reduction that is due to the change of the radius of curvature. The focal length of the depth-scaled refractive lenses for low Fresnel numbers is therefore stabilized by the focal shift that is due to the diffraction at the lens aperture.

B. Diffractive Lens

For the case of a diffractive design, the situation is very different. The results of the numerical calculations are presented in Fig. 5. For very low Fresnel numbers ($N \leq 2$), the behavior is identical to that in the refractive case because of the trivial fact that both surface profiles are identical for $N \leq 2$. For higher values of N, the focal-length dependence decreases rapidly, and the focal length is nearly independent of the depth, e.g., blaze of the structure. The focal length is then stabilized because of the diffraction at the lateral pattern, defined by the segment boundaries. This is the result expected for a diffractive lens with high N. This stabilization effect has been used successfully for the design of microlens arrays for confocal microscopy in which a focal-length deviation of only 120 nm at a focal length of 250 μm has been achieved experimentally.[11] In Fig. 4 the relative focal-length change is shown (open symbols). A striking observation is the sudden onset of the focal-length stabilization as soon as a small portion of the second segment is illuminated. At first sight this might appear surprising; however, it can be explained by the interference of the coherent partial waves emanating from the two segments. Furthermore, the focal length shows a pronounced oscillation in N with the periodicity of 2.

C. Phase Offset

The wrapped phase function $\Psi(x)$ of a diffractive lens can be written as[16]

$$\Psi(x) = [\phi(x) + \varphi_0] \bmod 2\pi, \tag{11}$$

where $\phi(x)$ is the lens phase function and φ_0 is a constant phase offset that shifts the segment boundaries laterally. This phase offset has no influence on the optical performance of an ideally fabricated and illuminated element, and it can be used as an additional design freedom. As we have shown above, the focal-length stabilization sets in with the illumination of the second segment. By means of the phase offset, the first segment boundary can be moved toward the lens center to reduce the size of the central segment in favor of the second segment. Figure 6 shows the focal length of a diffractive lens, scaled with a depth-scaling factor of $\mu = 1.25$ for different phase offsets φ_0. The onset of the focal-length stabilization is shifted with the first segment boundary to lower Fresnel numbers. Addition of a phase offset can be used to reduce the fabrication tolerances by enhancing the diffractive properties of an optical element. This concept has been used to reduce the fabrication tolerances for fan-out elements[15] and the zero-order intensity for binary diffractive diffusers.[16]

D. Energy Redistribution

Unfortunately, the stabilization of the focal length of the diffractive lenses also has a drawback. For $\mu \neq 1$, additional foci appear, and the energy is redistributed among

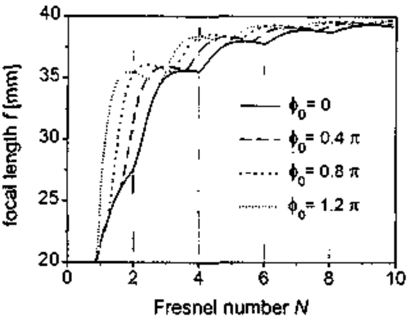

Fig. 6. Focal-length variation of depth-scaled ($\mu = 1.25$) diffractive lenses with different phase offsets φ_0. The onset of the focal-length stabilization can be shifted to lower N with the phase offset φ_0.

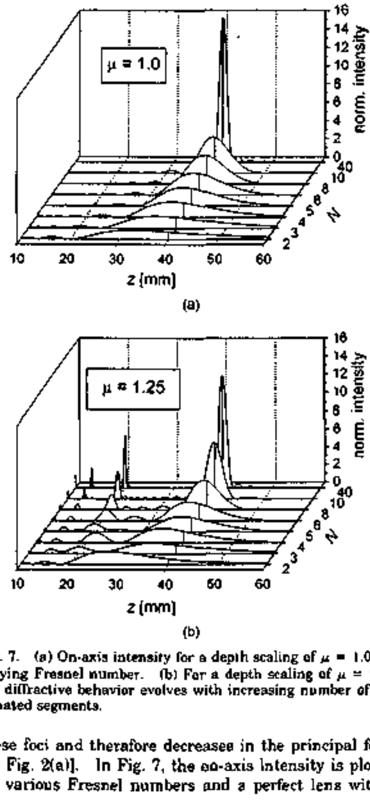

Fig. 7. (a) On-axis intensity for a depth scaling of $\mu = 1.0$ and varying Fresnel number. (b) For a depth scaling of $\mu = 1.25$, the diffractive behavior evolves with increasing number of illuminated segments.

these foci and therefore decreases in the principal focus [cf. Fig. 2(a)]. In Fig. 7, the on-axis intensity is plotted for various Fresnel numbers and a perfect lens with $\mu = 1.0$ [Fig. 7(a)] and a depth-scaled lens with $\mu = 1.25$ [Fig. 7(b)]. The intensity has been normalized to the area of the lenses for a meaningful presentation. For the depth-scaled case, the higher-order foci are already formed by the illumination of very few zones. This appearance of higher-order foci with depth errors and the nonsensitivity of the focal positions on the depth of the structure is a typical property of a diffractive optical element. This diffractive behavior becomes dominant even for few zones.

The intensities in the different foci depend on the depth scaling and the Fresnel number. For a small depth scaling ($\mu = 1.05$) and a large Fresnel number ($N = 40$), the intensity in the second-order focus is very small: it is 1.4% of the intensity of the first-order focus. For decreasing N, the relative intensity in the second-order focus increases to 4.5% for $N = 10$ and to 19% for $N = 4$. For a large depth scaling ($\mu = 1.25$) this increase is less pronounced: The second-order intensity increases from 44% for infinite N to 50% for $N = 10$ and 68% for $N = 4$, respectively. For an even larger depth scaling a focal switch occurs: The second-order intensity exceeds the first-order intensity for $\mu > 1.33$ and infinite N and for a slightly lower depth scaling for low N. The presence of the focal switch is not a low-Fresnel-number property, but the evolution of the second-order intensity with the depth scaling does depend on N, as discussed above. In comparison, the effect of focal switching was recently observed in another system[17]: Diffracting screens with a nonuniform amplitude transmission can produce axial superresolution. Axial superresolution means a narrower central lobe in the axial intensity distribution at the cost of stronger lateral lobes as compared with the axial intensity distribution for a spherical wave incident upon a screen with uniform amplitude transmission. Because of the narrower central lobe, such systems show a reduced sensitivity to the focal shift, and, for sufficiently low Fresnel numbers, an increase of the intensity of the lateral lobe over the main lobe results in a focal switch.

6. EVOLUTION OF DIFFRACTIVE BEHAVIOR: A FOURIER OPTICS APPROACH

As was shown above for lenses, we only have to illuminate a second segment to see a stabilization of the focal length with respect to depth errors. In numerical calculations, Rossi *et al.*[9] also found indications of an early onset of diffractive behavior when the number of illuminated zones is increased. By consideration of the influence of shrinkage errors on the performance of a blazed grating, the difference between its diffractive and refractive properties was recently discussed by Herzig,[18] and an analogous behavior was found.

Sinzinger and Testorf[10] investigated the chromatic behavior of a blazed grating with varying blaze depth in the limit of many illuminated segments, using a Fourier optics approach. They discussed the transition from a low-order to a higher-order diffractive element. Increasing the order, which leads to deeper elements, gives rise to an oscillating behavior of an overall refractive type.

In the remainder of this paper we present an explanation for the distinct diffractive behavior of the depth-scaled lenses observed even for a low number of illuminated segments. Using a Fourier optics approach and starting from a linear blazed grating, we then extend the result obtained to cylindrical one-dimensional and circular two-dimensional phase zone lenses.

A. Blazed Grating

A blazed grating with only one illuminated period is simply a microprism. Its deflection angle changes when the prism blaze angle is changed because of a depth error. By increasing the number of illuminated segments b, a transition to a diffractive device will occur because of the interference between the elementary waves emanating from the individual segments.[4] Depth errors will then affect only the intensity distribution within the allowed angular spectrum, which itself will be unaffected. We shall regard this insensitivity of the angular spectrum with respect to depth errors as a diffractive property of a planar optical element.

The transmission function of a partially illuminated blazed grating[19] can be written as

$$t(x) = \left\{\frac{1}{\Lambda}\operatorname{comb}\left(\frac{x}{\Lambda}\right) \otimes \left[\exp\left(i2\pi\mu\frac{x}{\Lambda}\right)\operatorname{rect}\left(\frac{x}{\Lambda}\right)\right]\right\}\operatorname{rect}\left(\frac{x}{b\Lambda}\right), \tag{12}$$

where Λ denotes the grating period; b, the number of illuminated periods; μ, the depth-scaling factor; and $\otimes$, the convolution operation. The comb function represents an array of delta functions and is defined in Chap. 3 of Ref. 14. The partial illumination is taken into account by the last rect function. We are interested in the intensity distribution in the Fourier plane. The Fourier transform of the transmission function is given by [see Chap. 7 of Ref. 14]

$$g(\nu) = \left(\operatorname{comb}(\nu\Lambda)\left\{\delta\left(\nu - \frac{\mu}{\Lambda}\right) \otimes [\Lambda \operatorname{sinc}(\nu\Lambda)]\right\}\right) \otimes [b\Lambda \operatorname{sinc}(\nu b\Lambda)], \tag{13}$$

which can be evaluated to

$$g(\nu) = b\Lambda^2 \operatorname{sinc}\left[\left(\nu - \frac{\mu}{\Lambda}\right)\Lambda\right]\sum_{n=-\infty}^{\infty}\operatorname{sinc}\left[\left(\nu - \frac{n}{\Lambda}\right)b\Lambda\right] = b\Lambda^2 g_{\text{blaze}} g_{\text{grat}}, \tag{14}$$

with $\operatorname{sinc}(x) = \sin(\pi x)/(\pi x)$. The diffraction pattern is given by $I(\nu) = |g(\nu)|^2$. Its shape is determined by a shifted sinc function (g_{blaze}), multiplied by g_{grat}. This factor consists of a series of sinc functions with finite widths determined by the number of illuminated segments b, each centered at a position given by the grating equation. The corresponding width w_g of a peak in g_{grat} is a measure of the resolving power of the grating. For an infinite number of illuminated segments b, g_{grat} becomes the comb function.

A depth error μ changes the blaze angle and therefore the refraction angle. This leads to a displacement of the g_{blaze} sinc function. Its width w_b is determined by the diffraction at one single segment and is therefore much broader than the width of the sinc functions forming g_{grat}. It acts as an envelope of the allowed angular spectrum. Figure 8 shows the blaze and the grating contributions [Fig. 8(a)] and the resulting intensity [Fig. 8(b)] for $b = 2$. As can be seen, even for two illuminated segments, w_g is much narrower than w_b. As a result, the intensity distribution shows precursors of the individual diffraction orders for $\mu \neq 1$. A depth error shifts the envelope and results in a nonvanishing intensity in the higher orders. For low b, the maxima of the precursors of the individual orders are not exactly at the position given by the grating period, but they approach this value with increasing b and therefore decreasing w_g.

Below, the extension to cylindrical and circular lenses is presented.

B. Cylindrical Diffractive Lens

For simplicity reasons, let us first consider a one-dimensional (cylindrical) zone lens in the paraxial approximation. Its transmission function is given by

$$t(x) = \left\{\operatorname{comb}\left(\frac{x^2}{2\lambda f}\right) \otimes \left[\exp\left(i2\pi\mu\frac{x^2}{2\lambda f}\right)\operatorname{rect}\left(\frac{x^2}{2\lambda f}\right)\right]\right\}\operatorname{rect}\left(\frac{x^2}{2\lambda f}\Big/ b\right). \tag{15}$$

By means of the variable substitution

$$\xi = \frac{x^2}{2\lambda f}, \tag{16}$$

the transmission function can be rendered periodic.

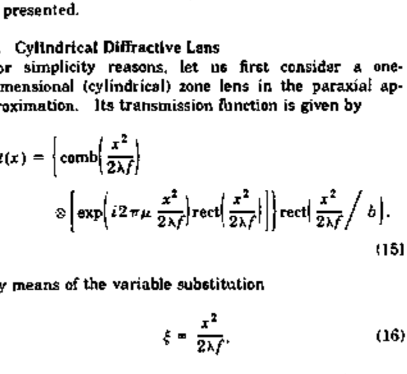

Fig. 8. (a) Grating and blaze contributions for $b = 2$ and a depth scaling of $\mu = 1.25$. The width w_g of the peaks is already much narrower than the width w_b of the envelope function g_{blaze}. (b) Precursors of the diffraction orders have already formed in the resulting intensity distribution $I(\nu)$.

After the substitution, the transmission function can be written in the same form as that of a blazed grating:

$$t(\xi) = \{\mathrm{comb}(\xi) \otimes [\exp(i2\pi\mu\xi)\mathrm{rect}(\xi)]\}\mathrm{rect}(\xi/b). \tag{17}$$

This transforms to

$$g(\eta) = \{\mathrm{comb}(\eta)[\delta(\eta - \mu) \otimes \mathrm{sinc}(\eta)]\} \otimes b\ \mathrm{sinc}(b\eta) \tag{18}$$

and to

$$\begin{aligned} g(\eta) &= b\ \mathrm{sinc}(\eta - \mu) \sum_{n=-\infty}^{\infty} \mathrm{sinc}[b(\eta - n)] \\ &= b g_{\mathrm{blaze}} \cdot g_{\mathrm{grat}} \end{aligned} \tag{19}$$

by use of the δ function properties for the evaluation of the convolution integral. The width of the sinc functions in g_{grat} is given by the size b of the illuminated aperture, whereas the width of the sinc function in g_{blaze} is constant in the reduced coordinate representation, with its position being shifted by a depth scaling.

If we identify the inverse Fourier variable $1/\eta$ as the reduced coordinate z/f, we obtain

$$\begin{aligned} I(z, \mu, N) &= |g(z, \mu, N)|^2 \\ &= \left(\frac{N}{2}\right)^2 \mathrm{sinc}^2\left(\frac{f}{z} - \mu\right) \sum_{n=-\infty}^{\infty} \mathrm{sinc}^2\left[\frac{N}{2}\left(\frac{f}{z} - n\right)\right] \end{aligned} \tag{20}$$

for the on-axis intensity, where we substituted the number of illuminated segments b by the Fresnel number $N/2$. Again, as shown in Fig. 9, even for an element with only two segments illuminated, the angular spectrum according to the diffraction at the segments (g_{grat}) is sufficiently resolved to produce precursors of the higher-order foci in the on-axis intensity according to the envelope (g_{blaze}) given by the diffraction at an individual segment. This explains the onset of the diffractive behavior as early as the second segment is illuminated.

C. Circular Diffractive Lens

We now extend the results from the one-dimensional cylindrical diffractive lens to circular lenses while making use of the analytical results given in the first part of this paper. For a depth-scaled refractive lens, the on-axis intensity distribution is given by Eq. (9). This intensity distribution is given by a sinc function and a factor that depends on the Fresnel number and the coordinate z. This factor is responsible for the focal shift for low Fresnel numbers.

Symmetry considerations show that the position of possible foci for the circular lens will be the same as for the cylindrical lens. These focal positions are given by the series of sinc functions in Eq. (20). The diffractive lens with $b = 1$, with no phase offset φ_0 present, is strictly the same as a refractive lens for $N = 2$. The intensity distributions must therefore coincide for these cases. Therefore the prefactors have to be the same for both types of lenses, with the value being dependent only on the geometry of the aperture. If we substitute the prefactor of Eq. (20) by the factor of Eq. (9), we obtain the on-axis intensity for a depth-scaled, diffractive lens:

$$\begin{aligned} I(z, \mu, N) = \left(\frac{f\pi N}{z}\right)^2 \mathrm{sinc}^2\left(\frac{f}{z} - \mu\right) \\ \times \sum_{n=-\infty}^{\infty} \mathrm{sinc}^2\left[\frac{N}{2}\left(\frac{f}{z} - n\right)\right]. \end{aligned} \tag{21}$$

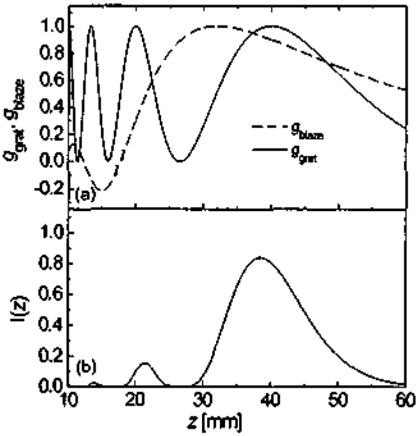

Fig. 9. (a) Grating and blaze contributions for a depth-scaled ($\mu = 1.25$) cylindrical diffractive lens with two segments illuminated. (b) On-axis intensity $I(v)$ for the same lens.

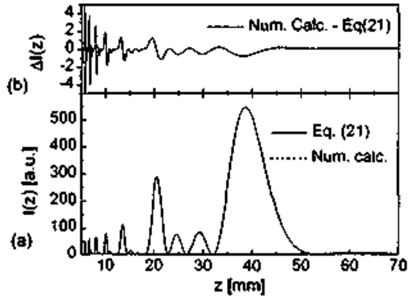

Fig. 10. (a) On-axis intensity pattern for a low-Fresnel-number depth-scaled diffractive lens ($f = 40$ mm, $N = 8$, $\mu = 1.25$). Results are compared for the Fourier optics approach in which Eq. (21) is used (solid curve), and for numerical calculations (dashed curve). (b) Difference $\Delta I(z)$ of the two intensity patterns.

Figure 10(a) shows the intensity pattern calculated by Eq. (21) for a circular symmetric depth-scaled diffractive lens (solid curve). It agrees well with the intensity pattern obtained by numerical calculations (dashed curve) for the same lens; both curves cannot be distinguished in the plot. Close to the aperture, the results obtained from the

Fourier approach begin to deviate from the numerical results, as shown in the difference plot in Fig. 10(b).

An important difference between the diffractive and the refractive lenses is the redistribution of the energy among the focal points observed for the diffractive lens on introduction of a depth error. This redistribution is described by the product of g_{grat} and the envelope g_{blaze}.

The expressions derived above are very useful in calculating the effects of simple surface distortions such as linear depth errors and give physical insight into the structure of the diffraction pattern obtained. For more-complicated surface distortions, the numerical method is more suitable. With this derivation we obtained an analytical result for the on-axis intensity distribution of depth-scaled continuous-relief diffractive lenses. It explains the early onset of diffractive behavior with the illumination of the second segment.

7. CONCLUSIONS

The phase function of an optical element can be coded into a surface relief in two ways: as a diffractive relief or a refractive relief. For low Fresnel numbers, because of the moderate maximum profile height, modern direct-writing technologies such as laser direct writing permit the fabrication of both designs with the same technology. We have investigated the tolerances for both designs with respect to profile depth errors. The results are important for choosing the appropriate lens coding scheme and for performing the optimization for practical applications such as Shack–Hartmann wave-front sensors and confocal microscopy.

For very low Fresnel numbers, the diffraction at the aperture stabilizes the focal length, independent of the coding scheme used. For the intermediate range of Fresnel numbers, we found a very early onset of the stabilization of the focal length as soon as the second segment was illuminated. One can shift the onset of the stabilization by shifting the first segment boundary, using a phase offset. For large Fresnel numbers, both designs showed the behavior expected for diffractive and refractive lenses with high N. The focal length of a diffractive lens is stabilized over the whole range of Fresnel numbers by the diffraction at the aperture and the diffraction at the pattern, given by the segment boundaries.

We presented a qualitative picture of the evolution of the stabilizing behavior of a partially illuminated diffractive lens, using Fourier optics in the paraxial domain. Even for two illuminated segments, the angular spectrum for the diffractive structure is sufficiently resolved to produce precursors of the diffraction orders and therefore leads to a stabilization of the focal length on depth errors.

ACKNOWLEDGMENTS

The authors gratefully acknowledge helpful discussions with K. Knop, C. Haine, and L. Kempen at Paul Scherrer Institute, Zurich and with R. Dändliker and H. P. Herzig from the Institute of Microtechnology, University of Neuchâtel. Furthermore, we are indebted to H. P. Herzig for giving us a copy of Ref. 18 prior to its publication.

REFERENCES

1. R. Völkel, H. P. Herzig, Ph. Nussbaum, P. Blattner, R. Dändliker, E. Cullmann, and W. B. Hugle, "Microlens lithography and smart masks," in *Micro-Nano-Engineering 96, Microelectronic Engineering* (Elsevier, Amsterdam, 1997).
2. Y. Li and E. Wolf, "Three-dimensional intensity distribution near the focus in systems of different Fresnel numbers," J. Opt. Soc. Am. A 1, 801–808 (1984).
3. G. Y. Yoon, T. Jitsuno, M. Nakatsuka, and S. Nakai, "Shack–Hartmann wave-front measurement with large *F*-number plastic microlens array," Appl. Opt. 35, 188–192 (1996).
4. R. E. Kunz and M. Rossi, "Phase-matched Fresnel elements," Opt. Commun. 97, 6–9 (1993).
5. E.-B. Kley, T. Possner, and R. Göring, "Realization of micro-optics and integrated optic components by electron-beam-lithographic surface profiling and ion exchange in glass," Int. J. Optoelectron. 8, 513–527 (1993).
6. M. T. Gale, M. Rossi, J. Pedersen, and H. Schütz, "Fabrication of continuous-relief microoptical elements by direct laser writing in photoresist," Opt. Eng. 33, 3556–3566 (1994).
7. C. G. Blough, D. Faklis, S. K. Mack, R. L. Michaels, and S. J. Ward, "High-efficiency replicated diffractive optics," in *Design, Fabrication, and Applications of Precision Plastic Optics*, R. Hebert, ed., Proc. SPIE 2600, 50–56 (1995).
8. D. Daly, R. F. Stevens, M. C. Hutley, and N. Davies, "The manufacture of microlenses by melting photo-resist," J. Meas. Sci. Technol. 1, 759–766 (1990).
9. M. Rossi, R. E. Kunz, and H-P. Herzig, "Refractive and diffractive properties of planar micro-optical elements," Appl. Opt. 34, 5996–6007 (1995).
10. S. Sinzinger and M. Testorf, "Transition between diffractive and refractive micro-optical components," Appl. Opt. 34, 5970–5976 (1995).
11. T. Hessler, M. T. Gale, M. Rossi, and R. E. Kunz, "Fabrication of Fresnel microlens arrays by direct writing in photoresist," in Vol. 5 of EOS Topical Meetings Digest Series (European Optical Society, Orsay, France, 1995), pp. 37–43.
12. Y. Li and E. Wolf, "Focal shifts in diffracted converging spherical waves," Opt. Commun. 39, 211–215 (1981).
13. J. H. Erkkila, "On the maximum wave intensity in the focal volume," *Opt. Commun. 43, 313–314 (1982).*
14. J. D. Gaskill, *Linear Systems, Fourier Transforms and Optics* (Wiley, New York, 1978), Chap. 10.2.
15. P. Ehbets, M. Rossi, and H. P. Herzig, "Continuous-relief fan out elements with optimized fabrication tolerances," Opt. Eng. 34, 3456–3464 (1995).
16. H. P. Herzig, M. Kuittinen, W. Singer, J. Wangler, and E. Piper, "Diffractive beam shaping elements at the fabrication limit," Opt. Eng. 35, 2779–2787 (1996).
17. M. Martinez-Corral and V. Climent, "Focal switch: a new effect in low-Fresnel-number systems," Appl. Opt. 35, 24–27 (1996).
18. H. P. Herzig, "Design of refractive and diffractive micro-optics," in *Micro-Optics: Elements, Systems, and Applications*, H. P. Herzig, ed. (Taylor & Francis, London, 1997).
19. M. C. Hutley, *Diffraction Gratings* (Academic, London, 1982), p. 49.

Publication II

Analysis and optimization of fabrication of continuous-relief diffractive optical elements

Thomas Hessler, Markus Rossi, Rino E. Kunz, and Michael T. Gale

The fabrication of continuous-relief diffractive optical elements by direct laser beam writing in photoresist is analyzed. The main limitation and tolerances are identified and their influence on the optical performance are quantified. Fabricated structures show rounded profile steps resulting from the convolution of the desired profile with the writing beam. This leads to a reduction of the diffraction efficiency. Optimization techniques are presented to minimize this effect. Scaling the profile depth by a factor $\mu > 1$ increases the first order diffraction efficiency for blazed elements. This method is also applied to suppress the zeroth diffraction order in computer generated holograms. A nonlinear compensation of the exposure data for the Gaussian beam convolution resulted in an 18 % increase of the diffraction efficiency for a blazed grating with a period 10 µm to a value of 79 %.

1. Introduction

Obtaining high diffraction efficiency is a challenge in design and fabrication especially for diffractive optical elements (DOE's) with large deflection angles. Such DOEs include off-axis and high numerical aperture (NA) lenses. To obtain a high efficiency, the phase function of the DOEs is either approximated by a multilevel structure or realized directly as continuous surface relief. The theoretical efficiency of ideal continuous-relief structures is, within the validity scalar theory, 100 %. In practice however, theoretical limitations and fabrication issues lead to efficiencies below the scalar value. Employing direct write techniques a continuous profile is generated in a single fabrication step. This is in contrast to the large number of steps necessary for the fabrication of multilevel elements with comparable efficiencies. Direct write techniques include single-point diamond turning (SPDT), electron-beam and laser-beam writing. An overview over these technologies is given in [1].

With SPDT excellent results have been achieved for high NA lenses [2]. However, this technology is limited to the fabrication of elements with circular symmetry. A higher flexibility is given by direct laser or e-beam writing. The electron beam can be focused down to very small spots. However, for optical applications employing resist films with a thickness in the order of 1 µm, the resolution is severely reduced by the so-called proximity effect. This effect can be reduced by point spread function compensation techniques [3, 4].

An alternative to e-beam writing is direct laser-beam writing. Complex DOEs with large areas are fabricated within a reasonable time frame. Circular laser-beam writing systems [5] are well adopted for the fabrication of circular structures. For more complex patterns or for lens arrays, a cartesian raster scan is preferable with respect to exposure data preparation. Elements with a large range of different optical parameters such as diffractive [6, 7] and refractive [8] low and high NA lenslets and lens arrays have successfully been fabricated over the last years.

The influence of fabrication tolerances such as etching or stage positioning errors on the performance of continuous-relief DOEs was investigated [9, 10, 11, 12] in the past. The influence of resolution limitations was discussed in general for blazed structures [13] and demonstrated for gray-tone exposure techniques [14, 15].

In this paper, we present an optimized DOE design, taking fabrication issues into account. It is founded on a quantitative understanding of the

---

When this work was performed all authors were with the Paul Scherrer Institute Zurich, Badenerstrasse 569, 8048 Zurich, Switzerland. M. Rossi, R.E. Kunz, and M.T. Gale are now with the CSEM Centre Suisse d'Electronique et de Microtechnique SA Zurich, Badenerstrasse 569, 8048 Zurich, Switzerland.

confining tolerances and limitations and is based on accessible technology parameters.

The underlying design and modeling methods for continuous-relief DOE's are described in the next Section. In Section 3 we describe and analyze the fabrication technology and its influence on the optical performance on continuous-relief DOE's. Optimization techniques for blazed structures are presented in Section 4. In Sections 5 and 6 these methods are applied to diffractive lenses and computer generated holograms.

2. Theory of continuous-relief diffractive optical elements

The first step in designing a diffractive optical element is to define the geometric and physical parameters of the optical element. These include the focal length, the numerical aperture NA, the refractive index n, and the design wavelength λ_0. If some of these parameters are not fixed by the application demands, they can be chosen to meet additional requirements, e.g. given by the fabrication technology. Once all system parameters are determined, a transmission function $t(x,y) = \exp(i\,\phi(x,y))$ for the DOE is calculated [16] and converted into a surface profile. Especially for DOEs with large deflection angles, this transformation has to be done with great care [17], a detailed description is found in [18].

For the modeling of the continuous surface-relief structures, we calculate the phase function in the tangential plane σ (cf. Fig. 1) behind the structured layer by tracing rays though the surface relief *h(x,y)*. The optical field in the image plane is calculated by using a Fourier transform for the far-field diffraction pattern or by solving the Rayleigh-Sommerfeld diffraction integrals for the near-field solution [10]. Thus, the influence of fabrication effects can be modeled.

For grating periods $\Lambda \le 10\,\lambda$ [19, 20], diffraction efficiency results from rigorous calculations do differ significantly from the 100 % value predicted by the thin layer approximation. This drop in diffraction efficiency can be predicted by phase-sensitive ray tracing calculations [21]. We will give a derivation for a simple formula, describing this drop in efficiency. Let us consider for simplicity a one dimensional blazed grating illuminated by a normal incident plane wave with unit amplitude. If we trace a series of rays through the grating structure as in Fig. 1, we observe the following phase and amplitude distribution in the tangential plane σ:

$$\varphi_S(x) = \sqrt{\frac{\Lambda}{\Lambda'}}\frac{1}{\Lambda}comb\left(\frac{x}{\Lambda}\right) \otimes \left\{\exp\left(i2\pi\frac{x}{\Lambda}\right)\cdot rect\left(\frac{x}{\Lambda'}\right)\right\} . \qquad (1)$$

This describes a plane wave with a rectangular intensity modulation, an amplitude of $\sqrt{\Lambda/\Lambda'}$ and a fill factor of Λ'/Λ. The sign $\otimes$ denotes the convolution operation, the comb-function is given by equally spaced delta functions as defined in [22]. The incident light is redistributed to the region $\Lambda' = \Lambda - \delta$, the width of the dark region δ is given by $\delta = d_{RT}\tan(\theta)$. The intensity modulation gives rise to diffraction during further propagation. The Mth order efficiency in the far field, obtained by taking the square modulu of the Fourier transform of Eq. (1) and normalizing it to the ideal grating [11], is given by:

$$\eta_S = \left(\frac{\Lambda'}{\Lambda}\right) = \left(1 - \frac{\delta}{\Lambda}\right). \qquad (2)$$

Equation (2) is a simple relation to estimate the theoretical limit of the diffraction efficiency for DOEs with small local grating periods. A good agreement with rigorous calculations has been shown in [21].

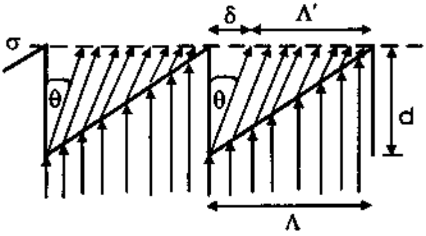

Fig. 1: Shadow effect for large deflecting angles θ.

3. Fabrication technology - direct laser beam writing

In this paper, we will concentrate on the fabrication of diffractive optical microstructures by direct laser beam writing into photoresist. Most of the results can also be applied for other direct write techniques such as e-beam writing. A detailed description of the direct laser beam writing technology is given in [1,6]. Only a brief summary of the specific features of the 3rd generation laser writing system developed at the CSEM [23] is given here. A photoresist coated substrate is raster-scanned under an intensity modulated, focused HeCd laser beam, leading to an exposure pattern which is transferred into a surface relief in a subsequent wet chemical development process. Copies of this original microstructure are made by electroplating a nickel shim that is used for low cost, high volume production by moulding, embossing or casting techniques [24].

The parameters of our laser beam writing system can be summarised as follows. The bitmap of exposure intensities (8 bit resolution) has a minimum pixel size of $p_x = p_y = 400$ nm. The interscan distance, -the distance between two subsequent line scans - is 400 nm or multiples of it. The focused spot size of the HeCd laser (wavelength $\lambda = 0.442$ µm) is in the range of 1 - 2 µm and is controlled by an autofocus system.

The intensity distribution of the focused writing spot is routinely measured in the two scanning directions with a knife edge technique. An amplitude grating ($\Lambda = 80$ µm) is mounted on a detector and scanned by the translation stages under the focused beam. The intensity distribution is obtained by taking the derivative of the detector signal and is then fitted with a Gaussian function:

$$I(x) = I_0 \exp\left\{-2\left(\frac{x}{w}\right)^2\right\} \qquad (3)$$

The waist w of the beam is referred to as the writing spot size.

A microstructure fabricated by direct laser-beam writing typically differs in certain ways from the desired surface profile. Especially sharp profile steps in DOE's can not be reproduced exactly. This is mainly due to the finite extension of the focused laser beam. The whole fabrication process includes several mechanical (scan movements) and chemical (exposure, development) processes; their respective tolerances will also influence the final result.

A. Tolerances of continuous-relief DOE fabrication

The key to a reproducible fabrication process is a calibration that connects the exposure values to the etching depth. The influence of etching errors has been studied previously [10,11], we will now briefly recall the main aspects. We define the etching error as a depth-scaling value

$$\mu = d/d_0 \qquad (4)$$

d being the measured and d_0 the desired depth. Further, the phase delay due to a wavelength detuning between the design and the illuminating wavelength is given by:

$$\alpha = \lambda_0\big(n(\lambda) - 1\big)/\lambda\big(n(\lambda_0) - 1\big). \qquad (5)$$

The diffraction efficiency of the Nth diffraction order of a continuous-relief diffractive lens designed to work in the Mth order is given by [10]:

$$\eta_D = \mathrm{sinc}^2(\alpha\mu M - N). \qquad (6)$$

As can be seen from Eq. (6), the tolerances are tighter for higher phase-matching numbers M. Typically, the etching depth is well controlled within ± 5 %. With more calibration effort and more sophisticated processing control of the photoresist accuracies of 2 % can be achieved. For a lens with $M = 1$ a 5 % etching error still gives an efficiency of 99 %, whereas for $M = 3$ the efficiency is reduced to 92 % and for $M = 5$ already to 81 %.

Further tolerances to be considered in practice are positioning errors and the raster line straightness. These inaccuracies will lead to a statistical or regular surface roughness. Accurate control of the stage movements and a proper choice of the writing spot size can minimize this effect [9].

B. Limitations of continuous-relief DOE fabrication

In order to reduce the effect of variations in the interscan distance and other tolerances of the scanning stages, a large writing spot is desired [9]. On the other hand, a large spot limits the resolution of the writing system. Mathematically, the profile obtained by the writing process is given by the convolution of the input surface relief with the point spread function of the writing spot [25]. Typically rounded structures are sketched in Fig. 2. A part of the relief has the wrong local slope, this is also referred to as *dead blaze* ε.

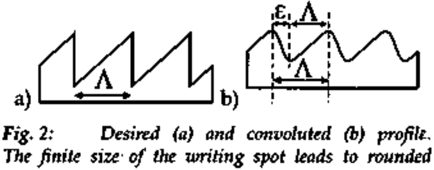

Fig. 2: Desired (a) and convoluted (b) profile. The finite size of the writing spot leads to rounded profile steps. Part of the grating is considered as dead blaze ε.

In order to obtain an estimate for the influence of the convolution effect on the diffraction efficiency, we calculate the phase distribution in the tangential plane σ behind these profiles. We assume the light passing through the dead area ε as lost. The phase function $\varphi(x)$ of the part with the "correct" direction in the tangential plane σ can be described by:

$$\varphi_C(x) = \frac{1}{\Lambda} comb\left(\frac{x}{\Lambda}\right) \otimes \left\{ \exp\left(i2\pi \frac{x}{\Lambda} \right) \cdot rect\left(\frac{x}{\tilde{\Lambda}} \right) \right\}. \qquad (7)$$

The resulting diffraction efficiency, is equal to the square modulus of the Fourier transform of Eq. (7), normalized to the square modulus of the Fourier transform of the phase function of an non-convoluted ideal blazed grating [11]. The efficiency in the desired order is expressed by the expression,

$$\eta_C = \left(\frac{\tilde{\Lambda}}{\Lambda} \right)^2 = \left(1 - \frac{\varepsilon}{\Lambda} \right)^2, \qquad (8)$$

where ε is the "dead blaze " as defined in Fig. 2. A similar result was obtained by [26]. The exact value of ε is analyzed in the next paragraph.

Comparing the convolution with the shadowing effect (Sec. IIb), we see that the convolution leads to a distorted phase with unit amplitude, whereas the shadowing affects the amplitude distribution and leaves the phase unchanged, i.e. correct.

Next, we combine the shadowing and convolution effects. By ray tracing, we obtain a phase and amplitude distribution in the tangential plane σ. The part with the correct phase is given by:

$$\varphi_{CS}(x) = \sqrt{\frac{\tilde{\Lambda}}{\Lambda'}} \frac{1}{\Lambda} comb\left(\frac{x}{\Lambda}\right) \otimes \left\{ \exp\left(i2\pi \frac{x}{\Lambda} \right) rect\left(\frac{x}{\Lambda'} \right) \right\}, \qquad (9)$$

where the active grating region is denoted by $\tilde{\Lambda} = \Lambda - \varepsilon$. The light is redistributed due to the shadowing to a region $\Lambda' = \tilde{\Lambda} - \delta$ with an amplitude of $\sqrt{\tilde{\Lambda}/\Lambda'}$. The width of the shadowed region δ is given by $\delta = \tan(\theta) \cdot \tilde{\Lambda} \tan(\beta)$. Performing the Fourier transform of Eq. (9) we obtain the following relation for the diffraction efficiency in the first order,

$$\eta_{CS} = \left(\frac{\tilde{\Lambda}\Lambda'}{\Lambda^2} \right) \approx \left(1 - \frac{\varepsilon}{\Lambda} \right)^2 \left(1 - \tan(\beta)\tan(\theta) \right) = \eta_C \eta_S, \qquad (10),$$

where we used $\tan(\beta) = d/\Lambda$. The derivation of Eq. (8) assumes a fixed part of the structure as dead blaze, which is a rough approximation to the real convoluted profile. In numerical simulations we convoluted blazed grating profiles with a Gaussian writing spot and analyzed the optical properties of these profiles by the ray-tracing method and subsequent free space propagation. For a given writing spot size w, we found that the efficiency as function of the grating period Λ is very well described by Eq. (8). The dead area ε is related to the writing spot size by a fixed relation of the form $\varepsilon \approx a_M * w$. The coefficient a_M depends on the phase-matching number M. For an illuminating wavelength $\lambda = 0.633\ \mu m$ and refractive indices $n_1 = 1.64$ and $n_C = 1.0$ the values $a_1 = 1.466$, $a_2 = 1.794$, $a_3 = 1.948$, and $a_4 = 2.094$ were obtained. These coefficients a_M depend slightly on the wavelength and the refractive index.

C. Other considerations on the writing parameters

The Gaussian writing beam has a finite depth of focus. Taking the Rayleigh range $z_R = \pi w^2/\lambda$ as a measure for the depth of focus, a spot size $w = 1.0\ \mu m$ results in a depth of focus of 12 µm for the HeCd laser wavelength $\lambda_0 = 0.442\ \mu m$ in photoresist. For the relatively thin structures considered here ($d = 1 - 3\ \mu m$) the variation of the spot size is negligible and has therefore been neglected. For the fabrication of very deep relief structures or smaller writing spot sizes w, the depth of focus has to be taken into account.

The exposure data values have to be sampled in the coordinate system of the scan. If the optical element does not have the same symmetry as the scan process, sampling effects may occur. For high numerical aperture lenslets sampled in a cartesian coordinate system, spurious lenslets will appear and eventually reduce the diffraction efficiency [27]. For the parameters used in our writing system, this effect is negligible for most applications.

4. Optimization methods

In this section, we present different procedures to increase the diffraction efficiency of laser-written diffractive optical elements. We will demonstrate the methods at the example of blazed gratings.

A. Higher phase-matching numbers

The size of the total dead area ε can be reduced by reducing the number of relief steps (Fig. 3 (a)). This is achieved by designing the element to work in a higher diffraction order. This leads to a surface with deeper profile and less profile steps. The aspect ratio of the structure remains constant, the dead area per profile step is thus only weakly increased.

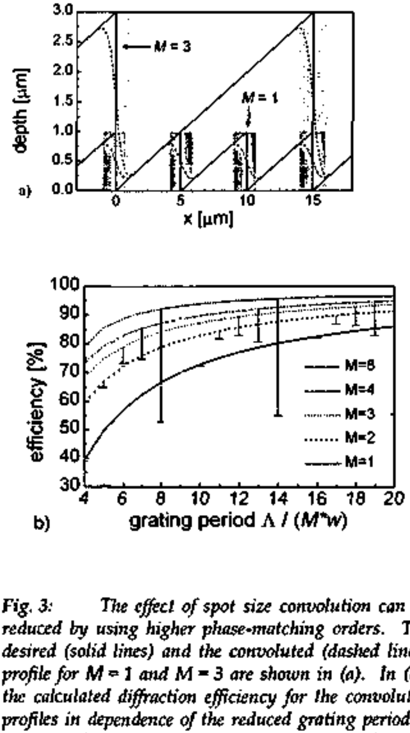

Fig. 3: The effect of spot size convolution can be reduced by using higher phase-matching orders. The desired (solid lines) and the convoluted (dashed lines) profile for M = 1 and M = 3 are shown in (a). In (b), the calculated diffraction efficiency for the convoluted profiles in dependence of the reduced grating period is shown. The error bars indicate the efficiency decrease due to a 5 % etching error.

As can be seen from Fig. 3 (b), the gain in efficiency can be considerable, especially for small grating periods Λ. However for deeper profiles, the sensitivity on etching errors is increased (see Eq. (6)), leading to tighter fabrication tolerances. This is indicated by the error bars in Fig. 3(b), which show the efficiency drop due to a 5 % etching error ($\mu = 1.05$). This is an upper bound for the etching tolerances obtained in practice. These tighter tolerances for high phase-matching numbers have to be considered in the design process.

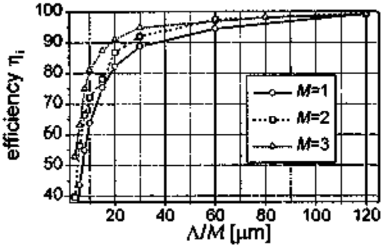

Fig. 4: Measured diffraction efficiencies for blazed gratings with different periods, working in the first, second and third order. The diffraction efficiency has been normalized to the total transmission in the grating diffraction plane.

Fig. 4 shows the measured diffraction efficiencies for blazed gratings with periods between 4 µm and 360 µm, designed for $M = 1$, 2 and 3. For these diffraction efficiency measurements, the substrate with the photoresist layer was attached to a prism with an index matching fluid in order to reduce errors introduced by interference effects due to a wedge of the substrate. The gratings were illuminated from the substrate side with an non-polarized HeNe laser, operating at the green wavelength of $\lambda = 543.5$ nm. The efficiencies were normalized to transmission through the unstructured substrate. The Fresnel and absorption losses are therefore not included. The blazed gratings have been written with the grating lines perpendicular to the fast raster scan axis. Due to small inaccuracies in the raster scan of the stages, additional stray light perpendicular to the diffraction plane is generated. The exact amount dependents on the stage performance and varies with the stage position. This stray light is usually in the order of a few (2-6) percent. Improvements are underway to reduce the stage positioning errors. To ensure a proper comparison between the different gratings fabricated, the efficiencies are based on the intensity integrated along the direction parallel to the grating grooves. The etching error for the gratings in Fig. 4 was below 2 %. For $\Lambda/M = 10$ µm, the efficiency of the first order grating ($\eta = 64$ %) could be increased to 72 % and 81 % for $M = 2$ and $M = 3$, respectively. As can be seen from Fig 4, working with phase-matching numbers up to $M = 3$ does lead to a significant increase in diffraction efficiency up to very large periods ($\Lambda = 60\,\mu m$). For a measured spot size of $w = 1.4\,\mu m$, we calculated the efficiencies for the $\Lambda/M = 10\,\mu m$ grating to be 63 %, 76 % and 82 % for $M = 1$, 2 and 3, respectively. Good coincidence was achieved with the predicted efficiencies.

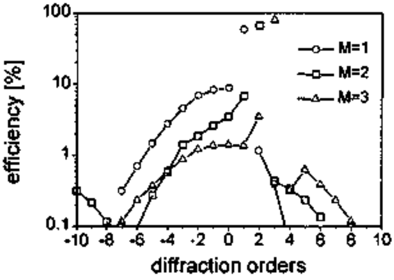

Fig. 5: Effect of convolution on the diffraction pattern for a blazed grating with a period of $\Lambda/M = 10\,\mu m$ and $M = 1$, 2 and 3. Please note the log scale for the efficiency axis.

Fig. 5 shows the typical diffraction pattern of three blazed gratings ($\Lambda/M = 10\,\mu m$) with rounded profile steps designed to work in the first, second and third order. The main part of the light missing in the desired order M can be found in lower and negative orders ($N < M$). The intensity in higher positive orders ($N > M$) is negligible. This confirms the intuitive ray-tracing picture where the rays passing through the rounded edges are directed in the wrong direction and are deflected at larger angles since the profile slope is steeper than the blaze angle.

The use of higher phase-matching numbers to decrease the dead area is simple in terms of data generation. Moreover there is no necessity to know of the exact writing spot size. On the other hand, working in higher diffraction orders increases the total number of propagating diffraction orders and the free spectral range, this can be disadvantageous for some applications. The need for deeper profiles imposes the need for thicker resist films which requires non-standard processing.

B. Linear scaling of exposure data

For convoluted blazed gratings we found that the first order diffraction efficiency as function of a depth scaling μ differs from the behavior of non-convoluted gratings, described by Eq. (6). The convoluted gratings show a maximum first order efficiency for depth scaling values $\mu > 1$. Thus, an intentional depth-scaling is used to increase the first order diffraction efficiency for convoluted gratings. The efficiency in the zeroth order can also reduced by such a linear distortion of the exposure data.

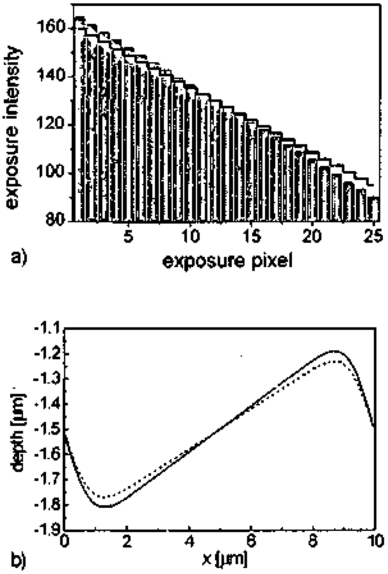

Fig. 6: (a) Exposure data obtained with linear distortion optimization ($w = 1.4$, $\mu = 1.15$, bars) and original data ($\mu = 1.0$, solid line). (b) Resulting surface relief for $\mu = \mu_1$ (solid line) and for $\mu = 1.0$ (dashed line). The diffraction efficiency is increased from 63.7 % to 66.3 %.

Fig. 7 shows the calculated diffraction efficiency of the zeroth (a) and first order (b) of a convoluted blazed grating as function of a depth-scaling μ and the reduced grating period Λ/w. The optimum depth scaling values μ for which the minimum zeroth order and the maximum first order diffraction intensity respectively is reached are denoted by μ_0 and μ_1. For large Λ/w, μ_0 and μ_1 approach $\mu = 1.0$ as given by Eq. (6). For low Λ/w, μ_0 and μ_1 show a strong dependence on Λ/w. The two values μ_0 and μ_1 are not identical, for the whole range of Λ/w it is $\mu_0 > \mu_1 > 1.0$. For a convoluted grating with $M = 1$, increasing the depth-scaling from $\mu = 1.0$ to the optimum value redistributes light mainly from the zeroth order to the desired diffraction order and to the higher diffraction orders.

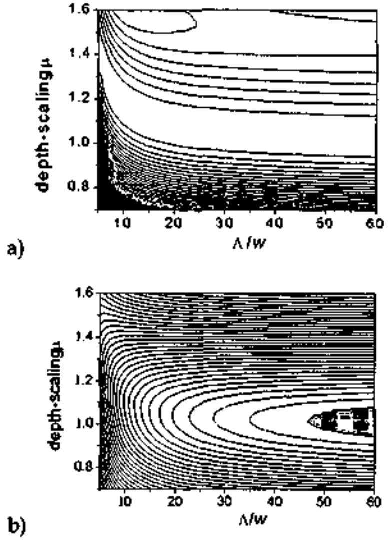

Fig. 7: Calculated efficiency in the zeroth (a) and first (b) diffraction order for a blazed grating with a depth-scaling μ and a grating period Λ / w. The scale ranges from 0 - *40% with a line spacing of 0.8 % in (a) and from* 30 - *100% with a line spacing of 2 % in b).*

The convoluted blazed grating with $\mu = 1$ has the correct blaze angle, but the total depth of the structure is below the desired value. An intentional depth scaling increases the total depth but also changes the blaze angle to a wrong value (Fig. 6). Especially for first order elements ($M = 1$) the depth scaling tolerances are relatively large (see Eq. (6)) so that in overall an increase in efficiency can be obtained. The gain in efficiency is typically 7 % for a $\Lambda = 10$ μm grating.

C. Individual pixel optimization

Another approach to compensate for the convolution effect is to actually optimize a given set of exposure data, taking the spot size into account. This can be done in either the design process itself, e.g. in a modified iterative Fourier transform algorithm or at later stage when transforming the phase values into a surface profile. Alternatively the optical design and the fabrication technology dependent exposure data generation can be separated. This has the advantage, that a given optical design can be used for different sets of fabrication parameters.

We investigated two different algorithms for the exposure data optimization.

The first one, is referred to as the difference algorithm [3]. Starting with a set of non-compensated exposure data points, the surface relief is calculated by simulating the exposure with the Gaussian writing beam. The difference between the resulting relief and the desired profile is added to this resulting relief. Corrected exposure data are extracted by taking the mean values of this profile over the exposure pixels. At this point, the discrete nature of the exposure raster is taken into account. The new exposure values are then limited to positive values within a specific range, depending on the resist calibration data. These steps are repeated a few times. Already after one or two iterations good improvements in diffraction efficiency are achieved. Usually, the algorithm is stopped after 10 - 20 iterations, depending on the grating period, the spot size, and the exposure pixel size.

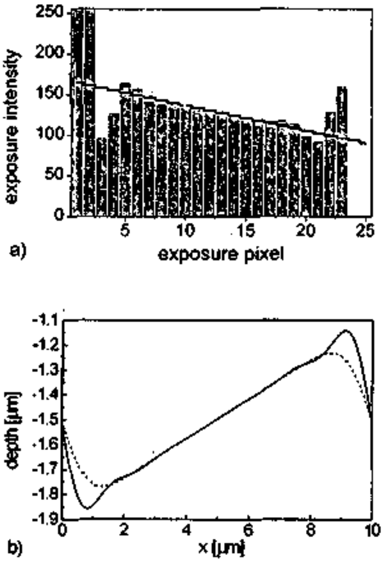

Fig. 8: (a) Exposure data obtained with difference optimization (bars) and (b) resulting surface relief for $\Lambda = 10$ *μm,* $w = 1.4$ *μm (solid line) and for comparison the non optimized relief (dashed line).*

Fig. 8 (a) shows the exposure values after the optimization procedure for a $\Lambda = 10\,\mu m$ grating. The typical result is an increased exposure Intensity at the deep side and a reduced exposure intensity at the shallow side of a profile step. The exposure intensity range was chosen 3 times the corresponding desired profile height. To allow for a reduction of the exposure intensity, the profile is placed in the middle of the exposure interval. The data values in the center of the grating period show a relatively smooth distribution. The resulting surface relief is shown in Fig. 8 (b), showing an increased maximum phase delay and a reduced dead area ε compared to the non-compensated relief.

The second approach we used is a constrained optimization [28] based on the sequential quadratic programming (SQP) method. As merit function we choose the first order diffraction efficiency. The only constraint we use was to limit the exposure data into a fixed interval of positive values as in the case of the difference algorithm.

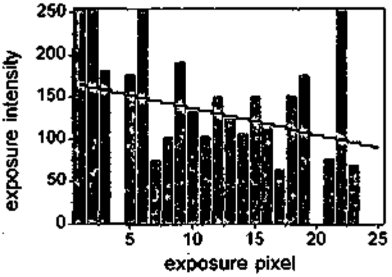

Fig. 9: Exposure data obtained with SQP optimization, $\Lambda = 10\,\mu m$, $w = 1.4\,\mu m$.

Fig. 9 (a) shows the result obtained for a $\Lambda = 10\,\mu m$ grating. Similar to the results obtained with the difference algorithm, the exposure values at the profile steps are maximal and minimal. In-between, the data are less smoothly distributed as in the first case. The theoretical efficiencies are slightly (1 - 2 %) higher than those obtained with the difference algorithm.

D. Robustness analysis and discussion

For both algorithms, the exposure is limited into the interval *[0, Imax]*. This intensity interval has to be divided to the 8-bit resolution of the exposure intensity modulator. Thus, a larger intensity interval reduces the exposure intensity dynamic. The highest efficiencies are obtained by placing the surface structure symmetrically into the exposure data interval. We compared the improvements by increasing the exposure intensity interval for a symmetrically placed blazed grating structure ($\Lambda/w = 7.5$).

Table 1: Diffraction efficiencies η in % for non optimized convoluted blazed grating (A) and optimized gratingr (B). The upper limit of the exposure intensity range [0, I_{max}] is varied from its minimum value I_0 to $10*I_0$.

	A	B			
Imax	I_0	I_0	$3I_0$	$5I_0$	$10I_0$
η	61.1s	65.9	76.5	78.9	80.1

The results are shown in Table 1. I_0 denotes the intensity necessary to obtain the maximum depth of the desired grating structure for $\Lambda >> w$. Increasing I_{max} predicts higher theoretical efficiencies but also reduces the dynamic range, since the whole interval is sampled with 8 bit resolution. For symmetrically placed structures, the minimum photoresist thickness needed for a DOE with a maximum depth d_m is $d(I_{max}/2)+d_m/2$, since there is no need for photoresist below the structured region. Regarding the reduced etching tolerances for thick resist films, the exposure interval should not be increased above five times its minimum value.

The dependence of the achievable efficiency in the optimization procedure on exposure pixel size p was investigated for the difference algorithm. For the values we are currently using in our writing system, a spot size of $w \geq 1.0\,\mu m$ and an exposure pixel size of $p^2 = 0.4 \times 0.4\,\mu m^2$, we found no improvement by reducing the pixel size. From our simulations, we conclude that an exposure pixel size below $w/2$ is sufficient to obtain the maximum improvement for the point spread function compensation. Smaller exposure pixel sizes only unnecessarily increase the amount of data to be handled and increase the writing time.

For the optimized exposure data, the question on their dependence on etching errors and uncertainties and changes in the writing spot size arises. Fig. 10 (a) shows the calculated diffraction efficiencies as function of the depth scaling μ for the optimized blazed gratings ($\Lambda = 10\,\mu m$, $w = 1.5\,\mu m$) and for the non-optimized gratings for comparison (dotted line). The tolerances on etching errors for the optimized profiles are only slightly smaller than for the non-optimized profile and both algorithm show similar tolerances. A very large etching error of 30 % is needed to obtain a lower diffraction efficiency with the optimized profiles.

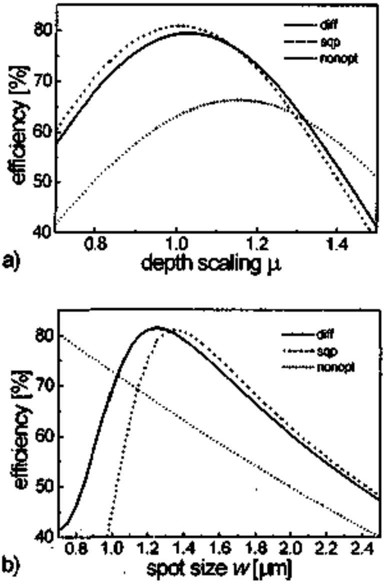

Fig. 10: Diffraction efficiency of optimized (difference algorithm: solid line, SQP algorithm: dashed line) blazed gratings ($\Lambda = 10\,\mu m$, $w = 1.4\,\mu m$) for linear etching tolerances (a) and for changes of the writing spot size (b). For comparison, the tolerances for a non-optimized grating are also shown (dotted line).

Fig. 10 (b) shows the dependence on changes of the spot size w. For both optimization algorithms, the efficiency suffers severely when the spot is significantly smaller than the one used in the optimization process. As expected from the exposure data distribution (Fig. 9), the SQP optimized grating shows the highest sensitivity on reductions in the spot size w.

In order to test the sensitivity to stage positioning errors, we simulated the exposure allowing a statistical variation of the exposure pixel size $\Delta p_x/p_x = \pm 0.1$. This corresponds to a mean deviation of the pixel size of 28 nm. For a $\Lambda = 10\,\mu m$ grating, a 6 % efficiency reduction results for the SQP optimized grating. The tolerance for the difference algorithm optimized grating is twice as large, resulting only in a 3 % efficiency reduction.

We conclude that the difference algorithm leads to somewhat lower theoretical efficiencies. However, this is compensated by its larger tolerances with respect to stage positioning errors and changes in the writing spot size. The simplicity and the resulting calculation speed of the difference algorithm makes it also suitable for large non-periodic structures.

E. Experimental results

Gratings optimized with the two algorithms have been fabricated, the results are shown in Table 2. The measured efficiencies for the non-optimized gratings as well as for the gratings optimized with the difference algorithm are close to the calculated values (Eq. (8)). For a $\Lambda = 10\,\mu m$ grating, the efficiency could be increased from 61 % to 79 % by the point spread function compensation.

Table 2: Measured diffraction efficiencies in % of compensated blazed gratings. The calculated theoretical values are given in brackets.

Algorithm	$\Lambda = 6\,\mu m$	$\Lambda = 10\,\mu m$	$\Lambda = 20\,\mu m$
none	41 (43.6)	61 (63.4)	83 (80.6)
Diff	64 (66.8)	79 (79.2)	90 (89.3)
SQP	60 (69.1)	74 (80.8)	88 (90.1)

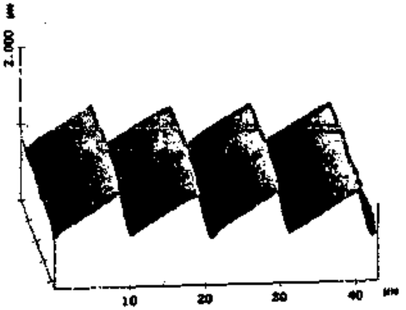

Fig. 11: AFM micrograph of a $\Lambda = 10\,\mu m$ first order grating with individual exposure pixel optimization.

The surface relief of a typical grating is shown in Fig. 11. The measured results of the elements optimized with the SQP algorithm are lower than the calculated values and also lower than the experimental values obtained with the difference algorithm. These results are comparable to the improvements obtained by increasing the phase-matching number form $M = 1$ to $M = 3$ (cf.

Sec. 4A) but less sensitive to depth errors than higher order elements.

5. Optimized lens design

All the above discussed methods are applied for the optimization of diffractive lenses. In practice however, fast optimization algorithm has to be used. Due to its simplicity, the use of higher phase-matching numbers is optimal. We take the experimental results obtained for the blazed gratings ($w = 1.4\,\mu m$) to estimate the diffraction efficiency [29] for a circular diffractive lens with a numerical aperture $NA = 0.1$ and Gaussian illumination beam. The intensity distribution is such that 95.6 % of the energy passes the aperture. For a lens designed in the first diffraction order ($M = 1$), we obtain an integrated efficiency of $\eta = 68\%$. For the same lens designed to work in the third diffraction order ($M = 3$) we expect $\eta = 83\%$. For a square aperture and constant incident intensity, we get for $M = 1$, $\eta = 51\%$ and for $M = 3$, we get $\eta = 72\%$. As mentioned before, the results obtained with the individual pixel optimization lead to similar improvements.

A. Balancing tolerances and limitations

Especially for large grating periods Λ, a design based on low phase-matching numbers M shows an improved robustness against etching errors. Assuming a given tolerance of the etching process and knowing the size of the writing spot w, the optimum phase-matching number M is calculated for each grating period of a diffractive lens. Changing the phase-matching number over the lens is a good compromise between robustness and theoretical gain in diffraction efficiency. However this also leads to a more complex diffraction pattern of the imperfect lens, since the lens is composed of annuli lenses working in different orders.

B. Phase offset

If a phase offset φ_0 is added to the lens phase function [30], the lateral positions of the phase transitions are shifted and one additional transition can be introduced. For lenses with a surface profile deviating form the ideal profile, the optical performance will be influenced by this lateral shift of the zone pattern. For circular lenses, the total dead area can be changed by the radial shift of the positions of the zone boundaries.

Moreover, the transitions can be shifted to regions with lower incident intensity, as the case for an incident Gaussian intensity distribution. The effect of adding a phase offset φ_0 is of relevance especially for lenses with a low number of zones, that is given by

$$N_Z = \frac{a^2}{2\lambda f}\frac{1}{2M} \qquad (12)$$

and has been shown for the case of an etching error [30, 11]. We investigated the use of adding a phase offset for the optimization of continuous-relief lenses. The Strehl ratio was calculated as a function of the phase offset φ_0 for a depth scaled, a convoluted and a depth-scaled and convoluted lens (F/# = 3, $f = 600\,\mu m$, $\lambda = 0.6238\,\mu m$, $M = 2$). For the simulations realistic parameters such as a depth-scaling of $\mu = 5\%$ and a writing spot size of $w = 1.0\,\mu m$ and a constant illumination over the aperture have been assumed.

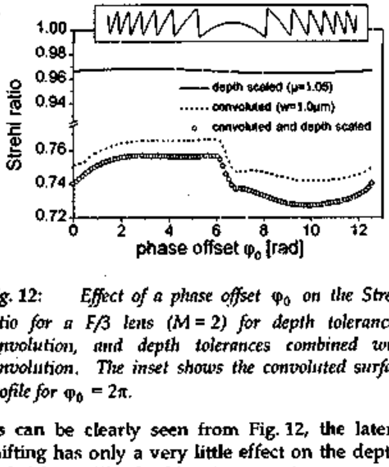

Fig. 12: Effect of a phase offset φ_0 on the Strehl ratio for a F/3 lens ($M = 2$) for depth tolerances, convolution, and depth tolerances combined with convolution. The inset shows the convoluted surface profile for $\varphi_0 = 2\pi$.

As can be clearly seen from Fig. 12, the lateral shifting has only a very little effect on the depth-scaled lens. The Strehl ratio is nearly constant at approx. 0.97. For the convoluted lens the influence is significantly higher. The Strehl ratio is lower and varies with the lateral shift of the zones between 0.74 and 0.77. The depth-scaled and convoluted lens is also dominated by the convolution, the additional depth scaling leads only to an additional reduction of the Sttehl ratio of ~ 1 % which is significantly smaller than in the depth-scaling only case (~ 3 %).

Especially for microlens arrays, having a small number of zones, shifting the transition regions leads to an overall improvement of the lens efficiency.

6. Zeroth order suppression in computer generated holograms

Whereas a non-vanishing zeroth diffraction order might be tolerable for some diffractive optical elements such as focusing lenses, it poses considerable problems for certain types of DOEs. Such DOEs are elements with a large spatial or angular extension of the image, e.g. beam shaping elements, diffusers, and computer generated holograms. The average intensity in the signal window is very small due to the large area. The zero-order contribution is typically concentrated to a limited area close to the optical axis and can easily exceed the average intensity. Recently an approach has been demonstrated [31] to overcome this problem for an excimer laser beam homogenizer fabricated by direct e-beam writing. The microlens array based homogenizer was designed to work off-axis, simply directing the zero order outside the homogenized area. This approach reduces the zero order influence completely. It has to be paid with off-axis structures, having smaller grating periods which are more difficult to fabricate.

CGHs, fabricated by direct-write methods, having a very small pixel size in the order of a few micrometers also suffer from a large zero-order contribution. The reason for this is the convolution effect. One solution to decrease the zeroth order is to compensate for the writing spot for the whole data set or to include the writing spot in the CGH design procedure [32]. As an other possibility, we simply used a linear distortion to eliminate the zero-order contribution in the reconstruction plane (cf. Sec. 4). This approach, based on a global linear distortion of the whole structure is simple and therefore also applicable for complex and large data. The phase function of the CGH was calculated using an iterative Fourier transform algorithm (IFTA) [16] with a resolution of 256x256 pixels. The surface relief was calculated using the thin layer approximation and multiplied with a constant depth scaling factor μ. The magnitude of the optimum depth scaling depends on the ratio of the surface relief feature sizes versus the writing spot size. For a global depth scaling, a typical feature size has been used. The assumption of a typical feature size is applicable for CGHs and well approximated by the CGH pixel size p_{CGH}.

In order to demonstrate the effect, we chose a very small pixel size of $p_{CGH} = 3$ µm for the CGH.

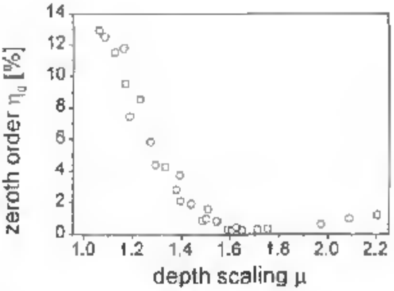

Fig. 13: Measured diffraction efficiency of the zero order for computer generated holograms having different depth. For the parameters used here, the zero order can be suppressed using a depth-scaling factor of 1.65.

Fig. 13 shows the efficiency in the zeroth order as a function of the global depth-scaling. The minimum for the zero order is very broad and the etching tolerances thus not very critical in order to obtain a significant improvement.

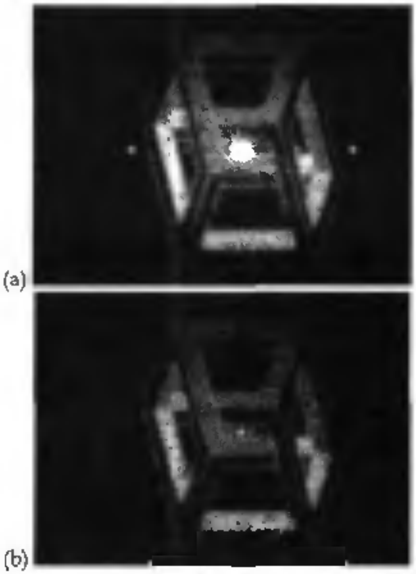

Fig. 14: Reconstruction of CGH with (a) standard depth (μ = 1.0) and (b) optimized depth (μ = μ0 = 1.65). The zeroth order could be reduced to average signal level.

Fig. 14 (a) shows the far field pattern of a CGH written with the nominal depth ($\mu = 1.0$) and Fig. 14 (b) shows the same structure, written with an optimized depth ($\mu = 1.65$). The intensity of the zero order could be reduced significantly. However, the background noise in the reconstruction is slightly enhanced. Larsson and coworkers [33] also found in experiments with kinoforms fabricated by direct electron-beam lithography that the optimum depth for a minimum in the zeroth order does not lead to a minimized uniformity error.

7. Conclusions

It has been shown that direct laser beam writing is an attractive master generation technology for DOE fabrication. Although the efficiency for blazed grating structures shows a strong decrease for small period, this limitation can be substantially reduced. Optimization techniques have been successfully demonstrated, leading to improvements in diffraction efficiency which would require half the writing spot size for non optimized designs.

The individual pixel optimization method leads to a comparable gain in efficiency as the use of higher phase-matching numbers ($M = 3$ instead of $M = 1$) for a $\Lambda/M = 10$ µm grating. The achievable gain in efficiency is considerable, the diffraction efficiency is increased from 61 % to 79 % for a 10 µm grating. Working in higher diffraction orders is a simple approach in terms of data generation, but it has to be balanced against the technology tolerances. However, we showed that with a well-controlled resist processing, the influence of etching tolerances is below the convolution effects, even for structures working in higher orders. The application of a linear scaling factor to correct for the convolution effect is especially suited for complex structures and the suppression of the zeroth diffraction order.

The authors gratefully acknowledge H. Schütz, J. Pedersen, and R. Stutz of CSEM Zurich for their support in laser beam writing technology and R. Dändliker and H.P. Herzig for fruitful discussions.

8. References

---

1 M.T. Gale, "Direct writing of continuous-relief elements," in: *Micro-Optics - Elements, Systems, and Applications,* H. P. Herzig, ed., (Taylor & Francis, London, 1997).

2 C.G. Blough, M. Rossi, S.K. Mack, R.L. Michaels, "Single-point diamond turning and replication of visible and near-infrared diffractive optical elements," Appl. Opt. 36 , 4648 - 4654 (1997).

3 M. Ekberg, F. Nikolajeff, M. Larsson, and S. Hard, "Proximity-compensated blazed transmission grating manufacture with direct-writing, electron-beam lithography," Appl. Opt. 33, 103 - 107 (1994).

4 F. Nikolajeff, J. Bengtson, M. Larrson, M. Ekberg, and S. Hård, "Measuring and modeling the proximity effect in direct-write electron-beam lithography kinoforms," Appl. Opt. 34, 897 - 903 (1994).

5 V. P. Koronkevich, V.P. Kiryanov, V.P. Korol'kov, A. G. Poleshchuk, V.V. Cherkashin, E.G. Churin, A.A. Kharissov, "Fabrication of diffractive optical elements by direct laser-writing with circular scanning", in *Digital Image Processing and Computer Graphics,* N.A. Kuznetsov, V. A. Soifer, eds., Proc. SPIE 2363, pp. 290-297 (1995)

6 M.T. Gale, M. Rossi, J. Pedersen, and H. Schütz, "Fabrication of continuous-relief micro-optical elements by direct laser writing in photoresists," Opt. Eng. 33, 3556 - 3566 (1994).

7 Th. Hessler, M. Rossi, J. Pedersen, M.T. Gale, M. Wegner, D. Steudle and H.J. Tiziani, "Microlens arrays with spatial variation of the optical functions," accepted for publication in JEOS A, Pure Appl. Opt. 6 (No. 6) (1997).

8 M. Rossi, Th. Hessler and M.T. Gale, "Design and Fabrication of Micro-Optical Elements with Deep Relief Structures," in Vol. 12 of EOS Topical Meeting Digest Series (European Optical Society, Orsay, France,1997), pp. 68 - 69.

9 M.T. Gale and K. Knop, "The fabrication of fine lens arrays by laser beam writing," Proc. SPIE 398, 347 - 353 (1983).

10 M. Rossi, R.E. Kunz, and H.P. Herzig, "Refractive and diffractive properties of planar micro-optical elements," Appl. Opt. 34, 5996 - 6007 (1995).

11 Th. Hessler and R.E. Kunz, "Relaxed fabrication tolerances for low Fresnel number lenses," J. Opt. Soc. Am. A 14, 1599 - 1606 (1997).

12 D.W. Ricks , "Scattering from diffractive optics," in *Diffractive and Miniaturized Optics* Critical Reviews of Optical Science and Technology,CR49, Lee SH Ed., pp. 187-211 (1993).

13 M. B. Fleming, M.C. Hutley, "Blazed diffractive optics", Appl. Opt. 36, 4635 - 4643 (1997).

14 T.J. Suleski ,D.C. O'Shea , "Gray-scale masks for diffractive-optics fabrication: I. Commercial slide imagers," Appl. Opt. 34, 7507 7517 (1995).

15 D.C. O'Shea, W.S. Rockward, "Gray-scale masks for diffractive-optics fabrication: II. Spatially filtered halftone screens," Appl. Opt. 34, 7518 - 7526 (1995).

16 H. P. Herzig, "Design of refractive and diffractive micro-optics", in Micro-Optics: Elements, Systems, and Applications, H. P. Herzig, ed., (Taylor & Francis, London, 1997).

17 R.E. Kunz and M. Rossi, "Phase-matched Fresnel elements," Opt. Commun. 97, 6 - 9 (1993).

18 Th. Hessler and M. Rossi, "Direct surface relief calculation for diffractive optical elements with large deflection angles," to be submitted to Appl. Opt.

19 E. Noponen, J. Turunen and A. Vasara, "Electromagnetic theory and design of diffractive lens arrays," J. Opt. Soc. Am. A 10, 434 - 443 (1993).

20 G.J. Swanson, "Binary optics technology: Theoretical limitations on the diffraction efficiency of multilevel diffractive optical elements," Tech. Rep. 914 (MIT Lincoln Laboratory, Cambridge, Mass., 1991).

21 M. Rossi, C.G. Blough, D.H. Raguin, E. K. Popov and D. Maystre, "Diffraction efficiency of high-NA continuous-relief diffractive lenses," In *Diffractive Optics and Micro-Optics,* Vol. 5 of 1996 OSA Technical Digest Series (Optical Society of America, Washington, D.C., 1996), pp. 233 - 236.

22 J.D. Gaskill, *Linear Systems, Fourier Transforms and Optics* (Wiley, New York, 1978), Chap. 10.2.

23 The CSEM (Centre Suisse d'Electronique et de Microtechnique SA) laser beam writing system has been developed at the Paul Scherrer Institute Zurich which was merged with the CSEM in July 1997.

24 M.T. Gale, "Replication," in: *Micro-Optics - Elements, Systems, and Applications,* H. P. Herzig, ed., Taylor & Francis, London, (1997).

25 M. Kuittinen, H.P. Herzig, and P. Ehbets, "Improvements in diffraction efficiency of gratings and microlenses with continuous relief structures," Opt. Commun. 120, 230-234 (1995).

26 T. Fujita, H. Nishihara, J. Koyama, "Blazed gratings and Fresnel lenses fabricated by electro-beam lithography," Opt. Lett. 7, 578 - 580 (1982).

27 E. Carcolé, J. Campos, I. Juvells, and S. Bosch, "Diffraction efficiency of low-resolution Fresnel encoded lenses," Appl. Opt. 33, 6741 - 6746 (1994).

28 Matlab Optimization Toolbox 1.5, The MathWorks Inc., Natick, Massachusetts (1996).

29 D.A. Buralli, G.M. Morris, "Effects of diffraction efficiency on the modulation transfer function of diffractive lenses", Appl. Opt. 31, 4389-4396 (1992).

30 P. Ehbets, M. Rossi, and H.P. Herzig, "Continuous-relief fan out elements with optimized fabrication tolerances," Opt. Eng. 34, 3456 - 3464 (1995).

31 F. Nikolajeff, S. Hård, B. Curtis, "Diffractive microlenses replicated in fused silica for eximer laser beam homogenizing," accepted for publication in Appl. Opt. 36 (No 32) (1997).

32 J. Bengtsson, "Direct inclusion of the proximity effect in the calculation of kinoforms," Appl. Opt. 33, 4993-4996 (1994).

33 M. Larsson, M. Ekberg, F. Nikolajeff, and S. Hård, "Successive development optimization of resist kinoforms manufactured with direct-writing, electron beam lithography," Appl. Opt. 33, 1176 - 1179 (1994).

Publication III

ELSEVIER
ADVANCED
TECHNOLOGY

Optics & Laser Technology [illegible]
[illegible]

PII: S0030-3992(96)00054-8

Microlens arrays for confocal microscopy

H. J. TIZIANI, R. ACHI, R. N. KRÄMER, T. HESSLER, M. T. GALE, M. ROSSI, R. E. KUNZ

A new, high resolution measuring system based on confocal microscopy has been developed for the evaluation of microlens arrays, in particular for applications in confocal microscopy itself. Lenslet arrays for parallel scanning and processing in confocal microscopy were designed as phase-matched Fresnel lenslets and fabricated by direct laser writing. Replica arrays were produced by ultraviolet embossing and hot embossing techniques. Fabricated arrays with a numerical aperture of 0.28 exhibited near diffraction limited performance and a focal length standard deviation of 120 nm in a nominal value of 250 μm. The technique developed represents a convenient and powerful technique for the characterization of lenslet arrays in general. © 1997 Elsevier Science Ltd. All rights reserved.

KEYWORDS: micro-optics, microlens arrays, confocal microscopy

Introduction

Optical scanning confocal microscopy is a well established technique[1–3] in which the capability of optical sectioning allows the three-dimensional reconstruction of the topography of technical surfaces to be built up from a series of hundreds of depth discriminated height sections. High lateral resolution can be obtained by the use of high numerical aperture (NA) objectives, but the resulting field size is small. This disadvantage can be overcome by the use of a high NA microlens array, instead of a single objective, to extend the field size and add the possibility of parallel scanning[4]. In order to obtain high quality, microlens arrays a small focal depth and small spherical aberration must be used. This paper describes the fabrication of a suitable lenslet array by direct laser writing lithography and a characterization technique developed to evaluate the microlens optical properties.

Considerable effort has been undertaken in recent years in the fabrication of lens arrays for a variety of applications[5–7]. The techniques developed include direct writing in resist by laser[8,9] or electron beam[10], photoresist reflow[11,12] and binary optics lithography[13]. Typical arrays can have thousands of microlenses, each with an aperture in the order of 10–100 μm, and have an overall array size of several millimetres. In many applications, not only is the performance of a single lenslet but also the uniformity over the array of great importance. The characterization technique described in this paper enables such an evaluation to be carried out as a convenient and rapid analysis technique and it has the potential of becoming a standard method for microlens array testing. It is based on confocal microscopy with microlenses as first described in Ref. 4. Figure 1 illustrates the basic technique, in which the lenslet array is used in a confocal microscope configuration with a perfect mirror as the object. The measurement data are used to characterize the lenslet array, rather than the object as in the conventional microscope usage.

The lenslet arrays used in this work were fabricated by direct laser writing in photoresist[5]. This is a very

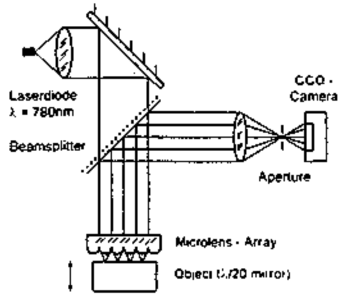

Fig. 1 Modified confocal microscope for focal length evaluation of microlens arrays. An optically flat mirror is used at the object plane

---

HJT, RA and RNK are in the Institut fur Technische Optik, Universitat Stuttgart, Pfaffenwaldring 9, D-70569 Stuttgart, Germany. TH, MTG, MR and REK are in the Paul Scherrer Institute, Badenerstrasse 569, CH-8048 Zurich, Switzerland
Received 12 August 1996. Revised 28 September 1996. Accepted 6 October 1996

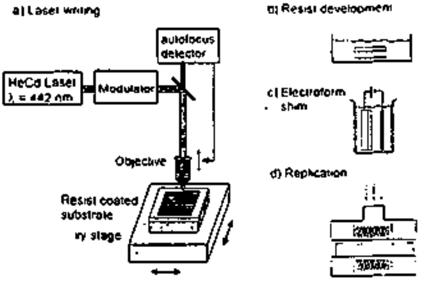

Fig. 2 Fabrication of continuous-relief micro-optical elements: laser writing into photoresist (a), development (b), electroforming (c) and replication by hot embossing or ultraviolet-casting (d)

powerful and flexible technique for producing arrays of computer-generated Fresnel lenslets satisfying a wide range of requirements. Figure 2 illustrates the basic process, in which a scanning, focused laser beam writes the desired exposure pattern in a light sensitive material such as photoresist. Following exposure, the photoresist film is developed to produce the required surface-relief microstructure. Precision control of the scanning, exposure and development processes enables continuous-relief Fresnel lenslets and lenslet arrays with good optical performance to be fabricated. Lenslets of numerical aperture up to 0.5 can be fabricated with zero dead space between individual lenslets, for example in arrays of square microlenses with individual dimensions down to about 5 μm and array areas of many cm^2. The developed surface-relief can be electroformed to a Ni shim and replicated by hot embossing or by ultraviolet-embossing into a thin film of ultraviolet-curable epoxy on a stable glass substrate[8].

The design and fabrication of the Fresnel lenslet arrays, with particular emphasis on arrays for confocal microscopy applications, are outlined in the next section. Details of the characterization technique are described in the following section, followed by the presentation of the experimental results on the lenslet performance and the uniformity of the arrays.

Lenslet design

The choice of lenslets for arrays for confocal microscopy is strongly influenced by the requirement for a highly uniform focal length distribution of the lenslets in the array. This simplifies the scanning and data processing procedures involved in the acquisition of an image. The lenslets, which are illuminated with monochromatic light, should have a high numerical aperture (NA > 0.25) and accurate (micrometre) lateral positioning of the focused spots in the array. High efficiency and low scattered light intensity are desirable but of secondary importance. The fabrication technology should enable large arrays of lenslets of size less than 100 μm square, with negligible dead space between lenslets, to be fabricated on optically flat substrates.

The design and fabrication considerations influencing the choice of lenslet type include the following.

Diffractive versus refractive lenslets

The focal length uniformity in arrays of diffractive lenslets is generally significantly better than that of refractive lenslets. The underlying reason is that the focal length of diffractive lenslets is controlled by the positions of lateral features whereas that of refractive lenslets is controlled by the radius of curvature of the relief profile (see Fig. 3); current fabrication technologies such as laser writing and microlithography are able to fabricate lateral features to very high (submicrometre) precision, whereas resist reflow techniques are (not yet) able to produce the corresponding uniformity in lenslet profile and size. On the other hand, the efficiency of the refractive lenslet arrays, even for monochromatic illumination, is generally better. Errors in the depth of diffractive lenslets lead to light in additional focal points and to stray light, and will affect the intensity but not the position of the main focal point[14]. For confocal microscope applications, however, uniformity in the focal length of large lenslet arrays is the main requirement. Arrays of Fresnel lenslets or zone plates are thus more suitable.

Continuous-relief versus binary Fresnel elements

Diffractive lenslets can be fabricated either as binary optical (multilevel) or continuous-relief elements. Both give good results when using state-of-the art fabrication technology. The optical performance of binary optical structures fabricated using three or four mask steps (8 to 16 levels) closely approaches that of continuous-relief elements; the fabrication requires high performance microlithography equipment with submicrometre alignment capability.

In the work described here, Fresnel microlens arrays were designed and fabricated as continuous-relief Phase-Matched Fresnel Elements (PMFEs)[15,16], fabricated in photoresist by a single step laser writing process. The PMFE is a continuous-relief microstructure consisting of individual segments whose lateral feature size is in the range of a few micrometres to several hundred micrometres. The design concept uses the laws of both wave and geometrical optics. Wave optics is used in order to obtain constructive interference between the waves emanating from different segments, whereas the surface relief shapes of the individual segments are optimized by geometrical optical procedures. PMFEs show an optical behaviour which has both diffractive and refractive properties where the strength of the diffractive or refractive behaviour depends upon the number of segments and their size. For applications in confocal microscopy, in which a highly uniform focal length distribution over the lenslet array is required, the PMFEs are designed to maximize the diffractive behaviour, with the focal length determined predominantly by the lateral feature sizes and positions.

Fresnel lenslet design

The PMFE design algorithm is based on phase-sensitive ray tracing. The surface profile is obtained by the condition, that the optical path length for all rays passing through the same segment is constant. Rays passing through neighbouring segments are allowed to

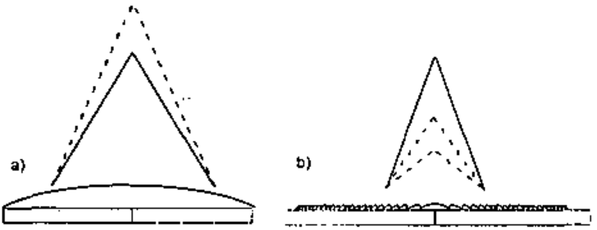

Fig. 3 Influence of depth errors on refractive and diffractive lenslets. For a refractive lenslet (a) the focal position is displaced, whereas for a diffractive lenslet (b) the energy is redistributed among higher-order foci

have an optical path difference of $M \times 2\pi$ ($M = 1, 2, 3, \ldots$), this determines the segment boundaries. This phase matching leads to a constructive interference of all rays. The PMFE design inherently takes into account the constraints of the fabrication process. With the current PSI laser writing system, the minimum segment size is about 5 µm, corresponding to a nominal NA of maximum 0.15 for a 2π phase step Fresnel zone lenslet. Higher NA lenslets with an NA up to 0.5 can be fabricated by moving to higher phase matching numbers M, leading to deeper and wider segments (Fig. 4). For continuous-relief microstructures, the resist film thickness is currently limited to about 5 µm for optimum quality of coated and processed films. Thicker films are possible, but generally suffer from inferior homogeneity and problems such as gas-bubble formation during the processing.

Sensitivity to fabrication errors

The phase matching number M is a design freedom which must be optimized for a given application. For the outer region of a lenslet, fabrication constraints (resist thickness $t \sim 5$ µm, minimum segment width $\Delta_{min} \sim 5$ µm) forces a phase-matching number $M = 3$. For the inner, low NA regions, however, M can be smaller—either 1, 2 or 3. Two strategies were investigated: (a) a constant phase-matching number $M = 3$ over the whole element (maximum M) and (b) keeping the phase-matching number always as low as possible (minimum M). In the second case, M increases when the segment width Δ falls below the minimum segment width Δ_{min}. The two resulting designs are shown in Fig. 5.

The main experimental error in the fabrication process results from variations in the development process and

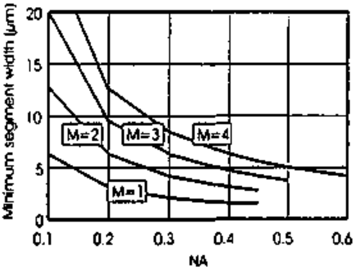

Fig. 4 Segment width Δ of a PMFE as a function of the numerical aperture NA and the phase-matching number M (calculated for a wavelength $\lambda = 632.8$ nm and the refractive index $n = 1.64$ of Shipley 1828 photoresist)

corresponds to a constant factor for the whole microstructure relief. An additional source is the latent image decay for long writing times[8] leading to a variation of this factor over the element area. The absolute depth error in units of wavelengths is thus dependent upon the local depth of the structure.

For the simulation of the behaviour of PMFEs, a dedicated simulation tool was developed based on phase sensitive ray tracing and Rayleigh–Sommerfeld diffraction theory. The influence of the depth errors typical in the exposed photoresist development was simulated. Numerical simulations[10] of the sensitivity of the two designs to depth errors were carried out.

For the first case ($M = 3$, constant over the whole element area), an efficiency reduction of ~ 15% for a depth error of ±5% was obtained. In addition,

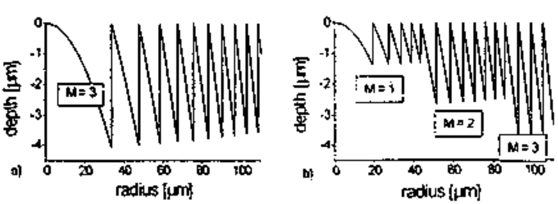

Fig. 5 Phase matching number M as a design parameter. (a) lenslet profile calculated with a maximum M over the whole element. (b) M is kept as low as possible

depending upon the sign of the depth error, higher or lower order focal points will be generated. A depth error of − 5%, expressed by a depth scaling factor $r = 0.95$, leads to an additional focal point at $z \approx 380$ μm with an efficiency of 10% compared with the main focal point at $z = 250$ μm. High phase-matching numbers, leading to deep structures, thus increase the sensitivity to depth errors. The effect is to lower the efficiency in the main focal points and to produce additional foci near the designed one. Since the measurement principle of confocal microscopy requires a well defined axial energy distribution with a high uniformity over the lens array, these effects can limit the system performance and therefore should be avoided as much as possible.

For the case of minimum M (Fig. 5(b)), the numerical simulations showed that a depth error of $r = 0.9$ leads to a loss of efficiency in the main focus of 8.5% and an energy of 2% in the lower order focal point at $z \approx 380$ μm. These values are distinctly better than those for the case of $M = 3 =$ constant. The conclusion is thus that degradation in the relevant optical performance of the lenslet arrays due to fabrication errors can be minimized by a design with values of M kept as low as possible.

Fabrication technology

A laser writing system has been developed at PSI for the fabrication of planar, continuous-relief lenslet and lenslet arrays[8]. Figure 2 shows the fabrication steps and the basic writing system in which a photoresist (Shipley AZ 1828) coated substrate (thickness 3–10 μm) is raster scanned under a focused laser beam (wavelength $\lambda = 442$ nm) whose intensity can be synchronously modulated to 256 discrete levels. The xy translation stage for the system used in this work was an air bearing granite table driven by linear motors with interferometer position measurement.

The relief data points need to be given in a two-dimensional bit-map format of exposure intensities, obtained from the calculated surface-relief by transformation to the two-dimensional writing raster and well-characterized resist development characteristic. The intensity data are calculated in advance or in real time for large elements, to reduce the amount of data handled. The lens array can easily be built up from individual elements via software procedures. The aperture of an individual lens can be also controlled—a rectangular shape allows the fabrication of microlens arrays with zero dead-space. The intensity data are loaded line by line into a buffer and are clocked out by the interferometer pulses during each line scan. The exposed resist film is then developed using Shipley's Microposit 303 Developer, resulting in a depth profile that is reproducible to ±5%. The writing time for the 30 mm by 30 mm lens array is 60 hours for the system used in this work, so that a stable environment and resist reciprocity were important considerations.

The dynamic position accuracy is crucial for the optical performance of the fabricated elements. Since the exposure is generated by overlapping Gaussian beams, a modulation in the profile with a grating period of the interscan distance is created. The amplitude is small if the overlap of the Gaussian beams is optimal[17]. If the interscan distance varies, however, this modulation can become significant and the resulting grating structure leads to stray light and a reduction in the optical efficiency of the element. The writing spot size for a specific element is therefore chosen as large as possible. For the system used in this work, the dynamic positioning accuracy was about ± 150 nm; an improved system is under development.

For the lens array, the writing parameters are an interline spacing of 1 μm, a focused spot size of 1.5 μm and a writing speed of 10 mm s^{-1}. The number of intensity pixels is limited to 64 k along the writing direction and, in principle, unlimited in the other direction. The maximum relief slope is given by the writing spot size and is typically 70°; the minimum segment size with a continuous surface-relief is about 5 μm with a maximum depth of about 5 μm.

Replication

The laser-written Fresnel lenslet arrays in photoresist can be used directly in an experimental confocal microscope, but are susceptible to damage by abrasion or chemical solvents. They are preferably electroformed to a Ni shim after gold-coating the resist relief, with second and third generation shims generated from this first shim by further electroforming steps. These shims can then be used to replicate the lenslet array microstructure into polymer and epoxy materials[6].

For the confocal microscope lenslet arrays, replicas were fabricated primarily by ultraviolet embossing. The shim is pressed against an optically flat glass substrate with an intermediate thin film of ultraviolet-curable epoxy, which is then cured by irradiating with ultraviolet light through the substrate. The replication process creates a high fidelity copy of the original shim, with additional surface roughness of the order of a few nanometres.

Replicas were also fabricated by hot embossing into polycarbonate foil. The optical flatness of such replicas is inferior to that of the ultraviolet-embossed elements, but they can be readily bent to form curved surfaces, opening up new and interesting possibilities in confocal microscope systems. A section of a hot embossed array is shown in Fig. 6.

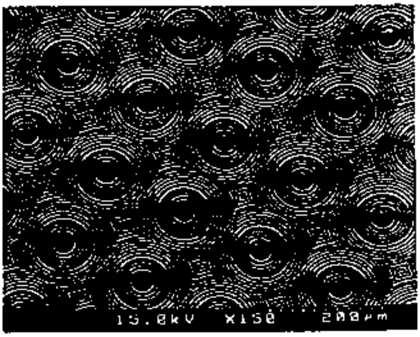

Fig. 6 Scanning electron micrograph of a section of the replicated lens array

Characterization

A new measuring system was developed in order to characterize the focal length variation in microlens arrays. The set-up is based on a confocal microscope in which the front objective is a microlens array (see Fig. 1). Instead of an object to be measured, a perfect mirror is used as a reference plane[4,11]. The illumination is a diode laser (λ = 780 nm), with the light collimated by lens L_c. The parallel beam is focused by the microlens array to form a two-dimensional diffraction limited spot array. The reflected light is collected by the same microlenses and focused by lens L_i (f = 120 mm) onto a pinhole. After passing through the pinhole, the light is incident on a CCD imager, at which the microlens pupil is in focus. The image is processed by a computer with a frame grabber. The detector signal has its maximum in perfect autocollimation; if the mirror is moved out of the focus plane, the incoming light is distributed over an area around the pinhole and the light flux passing the pinhole is reduced.

For the characterization of the microlens array, the mirror is moved stepwise in the axial (z) direction (Fig. 7). At each mirror position, z, the images of the microlens pupils (x_k, y_l) are stored in the frame grabber. The axial response for a confocal system with microlenses can be approximated by the on-axis intensity of one microlens in reflection as[19]

$$I(u) = \left(\frac{\sin\left(\frac{u}{2}\right)}{\frac{u}{2}}\right)^2 \text{ with } u = \frac{2\pi}{\lambda}\,\frac{l^2}{4f'^2_m}\,\Delta z \qquad (1)$$

l is the diameter, f'_m the focal length of one microlens and λ the illuminating wavelength. Δz describes the linear movement of the mirror. The intensity falls off to half its maximum value at a defocusing distance

$$\Delta z_{1/2} = \frac{0.22\lambda}{1-\cos\alpha} \qquad (2)$$

$$\frac{l}{2f'_m} \approx 2\sin\frac{\alpha}{2} \qquad (3)$$

where sin α is the numerical aperture of the microlenses. Hence, the full width at half maximum (FWHM) of the intensity response obtained by moving continuously through the focus is

$$\text{FWHM} = \frac{0.443\lambda}{1-\cos\alpha} \qquad (4)$$

In order to measure the focal length variation of the entire array, the brightest height section can be found for each microlens from the axial response. The height determination can be improved by taking the centre of gravity of each intensity series. Compared with the maximum determination, the influence of the camera noise is reduced and a higher accuracy is guaranteed. Using this approach, a sensitivity of 50 nm for the focal length determination was achieved.

Experimental results

Microlens arrays were fabricated by direct laser writing in photoresist, followed by electroforming and replication by ultraviolet-embossing into a Norland NOA-61 epoxy film on flat glass substrates. The arrays consisted of 200 × 200 lenslets, each 150 × 150 μm in size, with a nominal focal length of 250 μm (NA = 0.28) designed for a wavelength of λ = 780 nm. The dead-space between individual lenslets was essentially zero. Both original (photoresist) and replicated (NOA-61) arrays were characterized. Figures 8 and 9 show the focal length variation for both arrays. The grey scale representation (Figs 8(a) and 9(a)) shows the focal length variation over a 15 × 15 mm section of the 30 × 30 mm arrays. The data in Fig. 8 have been corrected for the substrate flatness by subtracting a filtered reference surface. The curvature of the glass substrate used for the replicated array is evident (Fig. 9): This could be eliminated by the use of an improved polished flat.

The line sections (Figs 8(b) and 9(b)) show the focal variation along a lenslet row of the arrays. The focal lengths' deviation for the direct laser written array lie within ±200 nm of the nominal value of 250 μm, with a standard deviation of 120 nm. This represents an excellent result which allows high precision confocal measurements to be made without the need for a reference, calibration measurement.

The axial response $I(z)$ of the microlenslets is an important quality feature which gives essential

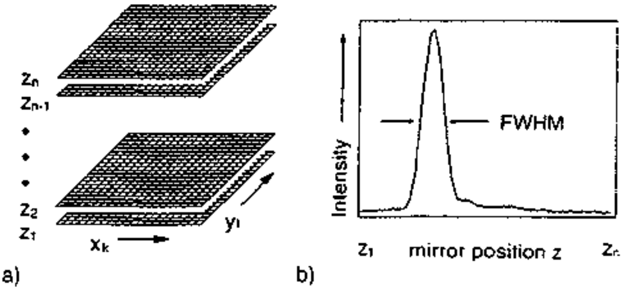

Fig. 7 (a) The pupil array imaged onto the CCD for different mirror positions z. (b) The intensity of one microlens when varying z

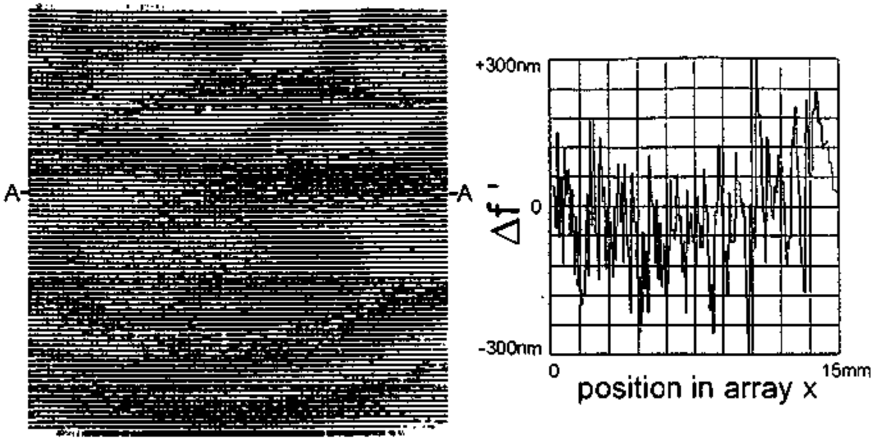

Fig. 8 Focal length variation Δf for a direct laser written microlens array. (a) Grey scale representation over the whole 15 × 15 mm field size. (b) Cross-section along single lenslet row (AA)

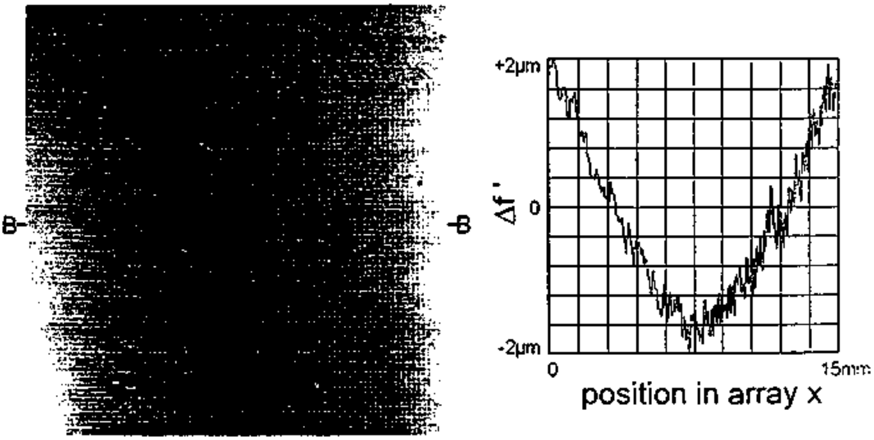

Fig. 9 Variation of Δf for a replicated microlens array (ultraviolet-embossed onto a glass substrate). (a) Grey scale representation over the whole 15 × 15 mm field size. (b) Cross-section along single lenslet row (BB)

information about spherical and chromatic aberration. Figure 10(a) shows the axial response of the photoresist array, measured using 256 height sections obtained by moving the mirror reference plane (see Figs 1 and 7). The measured FWHM is 12 µm, which compares well with the theoretical FWHM of 9 µm. The determination of small deviations from the theoretical FWHM is important for the later use of microlenses since they influence the accuracy of confocal microscope measurements.

Figure 10(b) illustrates information which can be gained from this characterization technique, in this case for a refractive lenslet with a focal length of $f' = 230$ µm (NA = 0.26). Distinct sidelobes can be seen, resulting from spherical aberrations, which increases the FWHM to about 30 µm (the theoretical FWHM is 10 µm).

Chromatic aberration can be determined using laser diodes with different wavelengths. Figure 11 shows the axial response of a diffractive lenslet at four different wavelengths (between 750 nm and 810 nm). The position of the centre of gravity of the curves gives the focal length variation. The chromatic focal length variation can be used in a chromatic measuring system[14].

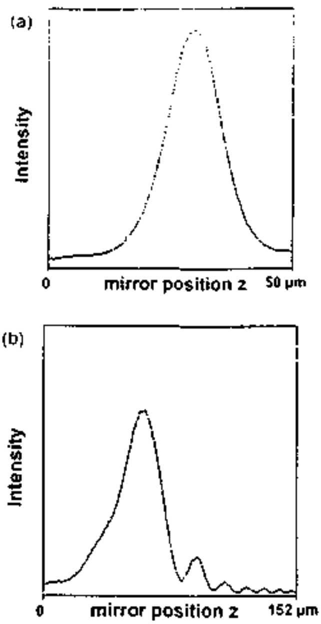

Fig. 10 Axial response for a single lens of a microlens array. (a) phase matched (diffractive) Fresnel lens; (b) refractive reflow lens

Conclusions

The direct laser writing of planar Fresnel microlenslet arrays has been shown to give excellent arrays for applications in parallel scanning confocal microscopy. Sensitivity to fabrication errors can be reduced by using a design which keeps the phase matching number as low as possible over the whole lenslet area. Other fabrication limitations in efficiency and stray light performance are not crucial to this application. Replicated arrays have been fabricated by ultraviolet-embossing into a thin epoxy film on a glass substrate and by hot embossing into a flexible polycarbonate film. Fabricated laser-written arrays with NA ≈ 0.28 exhibit a very high uniformity in focal length (standard deviation of 120 nm in a nominal 250 µm) and nearly diffraction limited axial response.

A new characterization technique, based upon a confocal microscope arrangement, has been used to characterize the array performance. The technique has high resolution and the parallel sampling gives rapid access to array specific information such as the uniformity of the lenslets. This technique represents a very convenient approach for lens array characterization in general.

Acknowledgements

The authors gratefully acknowledge H. Schütz, J. Pedersen and R. Stutz of PSI Zurich for their support in the fabrication by laser beam writing, Ni-shim generation and replication of the lens arrays.

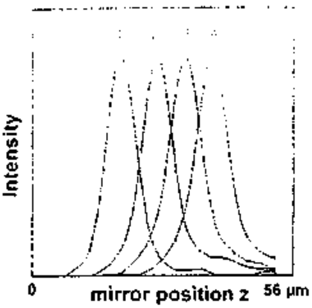

Fig. 11 Chromatic aberration (shift in position of focus) at four wavelengths λ_1 = 750 nm (1), λ_2 = 780 nm (2), λ_3 = 810 nm (3), λ_4 = 840 nm (4)

References

1 Wilson, T., Sheppard, C. *Theory and Practice of Scanning Optical Microscopy*, Academic Press (1984)

2 Brakenhoff, G.J., Blom, P., Barends, P. Confocal scanning light microscopy with high aperture immersion lenses, *J Microsc*, 117 (1979) 219–232

3 Carlson, K., Aslund, N. Confocal imaging for 3D digital microscopy, *Appl Opt*, 26 (1987) 3232–3238

4 Tiziani, H.J., Uhde, H.M. Three-dimensional analysis by a microlens-array confocal arrangement, *Appl Opt*, 33 (1994) 567–572

5 IOP Short Meetings on Microlens Arrays, National Physical Laboratory, Teddington UK (1991)

6 EOS Topical Meetings Digest Series 2, *Microlens Arrays*, National Physical Laboratory, Teddington UK, 13–14 May 1993

7 EOS Topical Meetings Digest Series 5, *Microlens Arrays* ISSN 1167-5357, National Physical Laboratory, Teddington UK, 11–12 May 1995

8 Gale, M.T., Rossi, M., Pedersen, J., Schütz, H. Fabrication of continuous-relief micro-optical elements by direct laser writing in photoresist, *Opt Eng*, 33 (1994) 3556–3566

9 Hessler, T., Gale M.T., Rossi, M., Kunz, R.E. Fabrication of microlens arrays by direct writing in photoresist, *EOS Topical Meetings Digest Series*, 5 (1995) 37–43

10 Kley, E.-B., Possner, T., Göring, R. Realization of micro-optics and integrated optic components by electron-beam-lithographic surface profiling and ion exchange in glass, *Int J Optoelectronics* 8 (1993) 513–527

11 Daley, D., Stevens, R.F., Hutley, M.C., Davies, N. The manufacture of microlenses by melting photo-resist, *J Meas Sci Technol* 1 (1990) 759–766

12 Haselbeck, S., Schreiber, H., Schwider, J., Streibl, N. Microlenses fabricated by melted photoresist, *Opt. Eng*. 6 (1993) 1322–1324

13 Motamedi, M.E., Anderson, R.J., de la Rosa, R., Hale, L.G., Gunning, W.J., Hall, R.L., Khoshnevisan, M. Binary optics thin film microlens array, *Proc SPIE*, 1751 (1992) 22–32

14 Rossi, M., Kunz, R.E., Herzig, H.P. Refractive and diffractive properties of planar micro-optical elements, *Appl Opt*, 34 (1995) 5996–6007

15 Kunz, R.E., Rossi, M. Phase-matched Fresnel elements, *Opt Commun*, 97 (1993) 6–10

16 Rossi, M. Phase-matched optical Fresnel elements, Dissertation Institute of Microtechnology, University of Neuchâtel (1995)

17 Gale, M.T., Knop, K. The fabrication of fine lens arrays by laser beam writing, *Proc. SPIE*, 398 (1983) 347–353

18 Tiziani, H.J., Achi, R., Krämer, R.N., Wiegers, L. Theoretical analysis of confocal microscopy with microlenses, *Appl Opt* 35 (1996) 120–125

19 Tiziani, H.J., Achi, R., Krämer, R.N. Chromatic confocal microscopy with microlenses, *J Mod Optics* 43 (1996) 155–163

Publication IV

Pure Appl. Opt. 6 (1997) 673–681. Printed in the UK PII: S0963-9659(97)86780-3

Microlens arrays with spatial variation of the optical functions

Th Hessler†§, M Rossi†, J Pedersen†, M T Gale†, M Wegner‡, D Steudle‡ and H J Tiziani‡

† Paul Scherrer Institute Zurich‖, Bodenerstrasse 569, CH-8048 Zurich, Switzerland
‡ Institut für Technische Optik, Universität Stuttgart, Pfaffenwaldring 9, D-70569 Stuttgart, Germany

Received 8 August 1997

Abstract. Direct laser beam writing is a mature technology for the fabrication of continuous-relief micro-optical (diffractive and refractive) lenses and lens arrays having a wide range of different optical design parameters. Whereas most microlens array applications require only one specific element type, some applications can profit from the combination of micro-optical elements having different optical functions in the same array. Lens arrays with a spatial variation of the focal length and beam deflection angle have been fabricated and successfully tested in confocal microscope measurements on non-planar surfaces.

1. Introduction

Microlens arrays consisting of refractive or diffractive lenslets have numerous applications in imaging, optical computing and detection systems. Most of these applications require arrays with identical lenslets. An optimization of the fabrication process for a specific lens parameter set is therefore typically required. As an example, excellent results have been demonstrated for lithography systems equipped with refractive lenslets fabricated by a photoresist reflow technique [1]. However, if diffractive lenses are also feasible for a given application and corresponding fabrication technologies are available, the range of geometrical and optical parameters accessible for the individual lenslets is considerably enlarged. In particular, the lens numerical aperture (NA) can cover a very large range. In addition, the *variation* of the optical function over the lens array can help to enable, improve or simplify many optical systems. The parameters that can be changed include the focal length (cf figure 1), the lens anamorphism, the aperture and the beam deflection angle. The latter can be used for spatially varying optical interconnects in optical computing systems and for matching arrays with different optical pitch in, for example, parallel optical sensing systems.

As demonstrations of arrays with varying optical functions, lens arrays with a spatial variation of the focal length and beam deflection angle have been realized. The fabrication technology, the lens design algorithms including the data handling and experimental characterization results of fabricated arrays are presented.

---

§ E-mail address: hessler@psi.ch

‖ The Paul Scherrer Institute Zurich is now part of the CSEM, Centre Suisse d'Electronique et de Microtechnique SA.

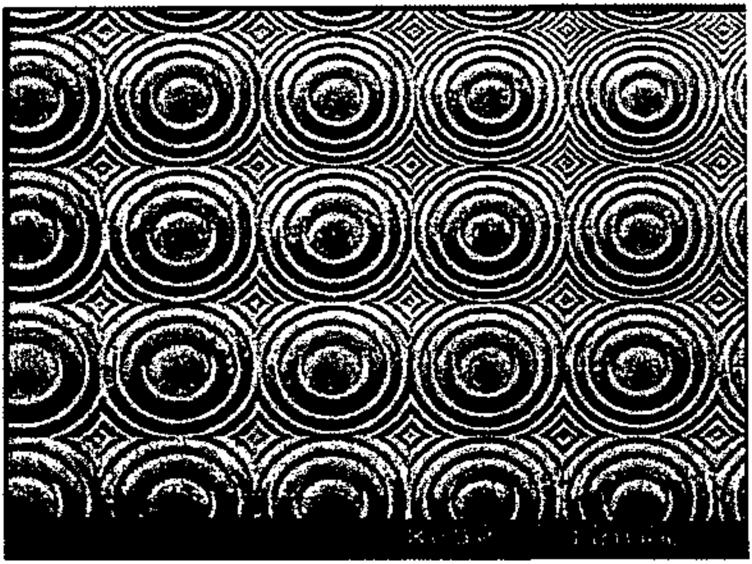

Figure 1. Section of a diffractive lens array with a spatially varying focal length in both lateral dimensions. The lenslet aperture is 100 × 100 μm^2.

2. Laser writing

Since the variation in the optical function can cover a large range, the technology used for the array fabrication needs to show a high level of flexibility. Over the past few years, direct laser beam writing in photoresist has proven to be highly reliable and accurate for the fabrication of continuous-relief micro-optical (diffractive and refractive) lenses and lens arrays with high fill factors [2, 3]. A detailed description of the process can be found in [4]; only a short summary is given here.

A substrate coated with a thin layer of photosensitive material is raster scanned under a focused HeCd laser spot. The intensity of the laser beam is modulated within 8-bit resolution, resulting in a grey-level exposure of the photoresist. This is converted into a surface relief structure by the subsequent wet-etching process. Copies of this original microstructure are made by electroplating a nickel shim that is used for low-cost, high-volume production by moulding, embossing or casting techniques. The ability to structure photoresist layers with depths of up to 15 μm with high accuracy allows the fabrication of diffractive elements working in higher diffraction orders, having deeper and wider zones. This feature of the fabrication technology counterbalances the limitations dictated by the finite size of the focused writing spot. Typical features of a new (third-generation) laser writing system, developed at the Paul Scherrer Institute (PSI) in Zurich, are an accessible profile depth of about 15 μm, a minimum addressable pixel size of 400 nm, an adjustable laser spot size, fabrication specific data preparation procedures and high-precision, computer-controlled translation stages. This wide range of writing parameters results in a large flexibility for the design and fabrication of microstructures. Within the range of accessible parameters, a given lens phase function can be realized in the form of a diffractive or a refractive lens using the same technology. Arrays of lenses having numerical apertures (NA) between 0.003 and 0.5 have been successfully fabricated previously [3].

3. Lens design and data preparation

For lens arrays with spatial varying optical functions, the optical design of the individual lenslets and the preparation of the laser writing exposure data needs special consideration. Having 8-bit resolution and submicron pixel sizes, the amount of exposure data increases to the order of several Gbytes for the lens arrays discussed here. Real-time computation of the exposure data is therefore favourable in order to avoid such large data files.

The individual steps of the real-time calculation are described in the following for a lens array in which the focal spots lie on the surface of a sphere. The beam deflection angle is chosen such that the central ray of each aperture has normal incidence on the spherical surface with radius R (see figure 2(*a*)). Such arrays can be used in confocal microscopy on curved surfaces (see section 5).

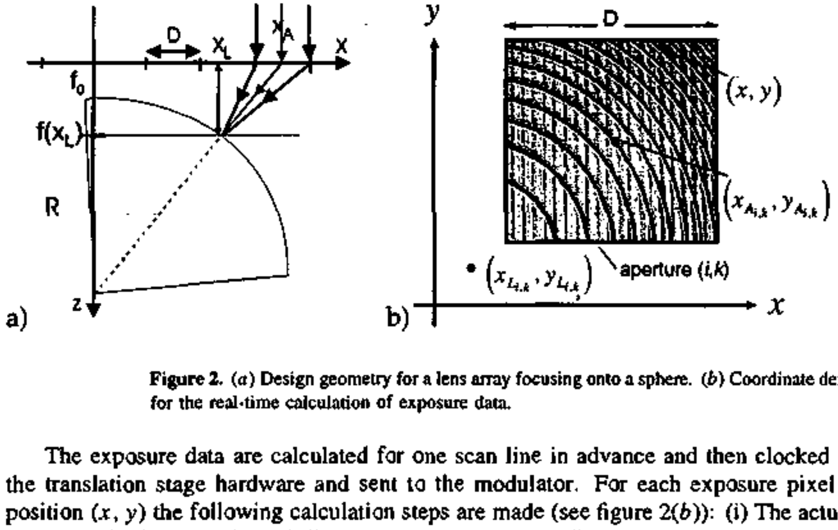

Figure 2. (*a*) Design geometry for a lens array focusing onto a sphere. (*b*) Coordinate definitions for the real-time calculation of exposure data.

The exposure data are calculated for one scan line in advance and then clocked out by the translation stage hardware and sent to the modulator. For each exposure pixel at the position (x, y) the following calculation steps are made (see figure 2(*b*)): (i) The actual lens aperture with index (i, k) and (ii) the aperture centre coordinates $(x_{A_{i,k}}, y_{A_{i,k}})$ are determined from the pixel position (x, y). (iii) The lens centre coordinates $(x_{L_{i,k}}, y_{L_{i,k}})$ are obtained from the aperture centre $(x_{A_{i,k}}, y_{A_{i,k}})$ by $x_{L_{i,k}} = r_{L_{i,k}} \cos(\theta_{i,k})$ and $y_{L_{i,k}} = r_{L_{i,k}} \sin(\theta_{i,k})$, with

$$\theta_{i,k} = \arctan\left(\frac{y_{A_{i,k}}}{x_{A_{i,k}}}\right) \qquad \text{and} \qquad r_{L_{i,k}} = R \sin\left(\arctan\left(\frac{\sqrt{x^2_{A_{i,k}} + y^2_{A_{i,k}}}}{R + f_0}\right)\right).$$

(iv) The focal length is given by $f_{i,k} = f_0 + R - \sqrt{R^2 - r^2_{L_{i,k}}}$. Then, (v) the value of the lens phase function $\phi(x - x_{L_{i,k}}, y - y_{L_{i,k}})$ at the pixel position, (vi) the local depth $d(x, y)$ of the corresponding surface relief are calculated and (vii) finally the exposure intensity, taking resist characteristics into account.

For lenslets with high numerical apertures, the transformation of the phase function into a surface relief (step (vi)) has to be done with great care. The scalar diffraction theory is valid only for feature sizes which are large compared to the illumination wavelength, whereas rigorous calculations are computationally very extensive. We use an approximation based on phase-sensitive ray tracing [5] which does permit the use of fast, scalar calculations down to grating periods of a few wavelengths. This is also roughly the lower limit imposed by the fabrication technology.

The following relation for the optimum profile depth maximum d_0 can be obtained by the phase-matching condition that all partial waves emanating from the grating structure interfere constructively in the Mth diffraction order:

$$d_0(\Lambda) = M\lambda\left(n - \sqrt{1 - \left(\frac{M\lambda}{\Lambda}\right)^2}\right)^{-1}. \tag{1}$$

The local grating period Λ is given by

$$\Lambda(x, y) = \frac{M2\pi}{\nabla\phi(x - x_{L_{l,k}}, y - y_{L_{l,k}})} \tag{2}$$

whereas the local depth $d(x, y)$ can be obtained from the local phase value $\phi(x - x_{L_{l,k}}, y - y_{L_{l,k}})$ by

$$d(x, y) = \mathrm{mod}(\phi(x - x_{L_{l,k}}, y - y_{L_{l,k}}), M2\pi)d_0(\Lambda(x, y))/M2\pi. \tag{3}$$

When designing microstructures it is essential to consider fabrication constraints and tolerances at as early a stage as possible in the design process. Due to the finite size of the writing spot (approximately 1.2 μm FWHM for the PSIZ system), the phase transitions at the zone boundaries cannot be fabricated perfectly vertical. Part of the active area is lost at these transition points. This dead area can be reduced by designing the elements to work in higher diffraction orders, however, having to deal with the drawback of tighter fabrication tolerances [6]. The aim is to use the optimum diffraction order for a given set of system parameters. The diffraction order (or phase-matching number) M can be changed locally within one element. Designs with low values of M result in a larger number of zones which leads to a reduced sensitivity of the focal length to fabrication errors [7].

Typically, all different influences are taken into account and, if needed, weighted against each other to achieve an optimum microlens performance. In the case of different lenses combined in the same array, as treated in this paper, some design features (e.g. the phase-matching number M and the rules for its choice) might change over the lens array.

4. Characterization of fabricated arrays

As first examples for lens arrays with a spatial variation of the optical functions, arrays with a variation in focal length have been fabricated. Lens arrays with the focal spots arranged on a cylindrical, spherical and parabolic surface were fabricated. As an illustration of typical results achievable, the scanning electron micrograph in figure 1 shows the section of a microlens array (aperture $100 \times 100\ \mu\mathrm{m}^2$) with a parabolic variation of the focal length in two dimensions. The fill factor of the lens array is 100%.

In the following, we concentrate on the results obtained for an array with a cylindrical focal spot distribution. It has been designed for an illumination wavelength of $\lambda = 0.6328\ \mu$m. The lens array consists of 80×80 lenses with a constant subaperture of $D = 200\ \mu$m side length, resulting in a total size of $16 \times 16\ \mathrm{mm}^2$. The focal lengths f vary between 300 and 2000 μm, thus giving numerical apertures between 0.31 and 0.06. This corresponds to a cylindrical focal surface with a radius of curvature of $R = 20$ mm. The lenses have a phase-matching number of $M = 2$ for the central section of the array and $M = 1$ for the outer regions, chosen to be constant within one lenslet.

The lenses were tested using a confocal microscope with a flat ($\lambda/20$) reference mirror instead of a measuring object. This set-up for microlens array characterization is described in [8]. The field size of the confocal microscope is 15×16 mm^2, enabling a parallel measurement of practically the whole lens array. The reference mirror was scanned in steps of 9 μm along the z-direction. Figure 3 shows the axial response of one row of the cylindrical array. A dark colour corresponds to high intensity. The axial responses of the individual lenses can be clearly distinguished—represented by the dark vertical stripes. The cylindrical arrangement of the focal points can be easily seen, as well as the appearance of additional foci in the central region of the lenslet row. This is due to energy in higher and lower diffraction orders. The appearance of these additional foci is mainly caused by slight imperfections of the surface relief [6].

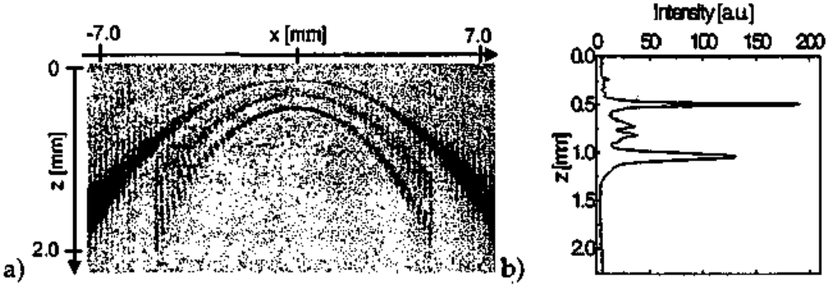

Figure 3. (a) Axial response of one lens row (at position $y = 0$ mm) of a cylindrical array. A dark colour corresponds to a high intensity. Additional to the main focal line, higher-order foci are present for the inner lenses. (b) Axial response $I(z)$ for lens at position $x = -3.0$ mm, $y = 0$ mm).

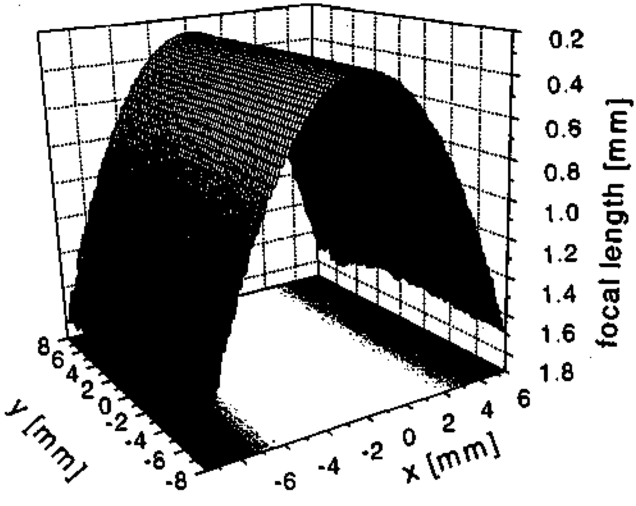

Figure 4. Measured focal length distribution of the lens array with a cylindrical focal point distribution.

In the measurement set-up the light passes twice through the lens array. Therefore, peaks in the axial response curve can be seen at the positions given by

$$z_{i,j} = \frac{f}{2} M \frac{m_i + m_j}{m_i m_j} \tag{4}$$

where f is the designed focal length and M is the phase-matching number of the lens or of the section of the lens. The $m_{i,j}$ are the diffraction orders of the first and second pass of the light through the lenslet, respectively. In the central part of figure 3 with $M = 2$, the peaks $z_{2,2}$ (designed), $z_{1,3}$, $z_{1,2}$ and $z_{1,1}$ can be seen, whereas in the outer part with $M = 1$, only the designed peak at $z_{1,1}$ and some very weak peaks for $i, j > 1$ are present. Due to the double pass through the lens array, the resulting intensity at the focal position is given by the square of the lens efficiency in the desired order. Depending upon the application, the effects of higher-order foci can be overcome by proper data or image analysis.

The centres of gravity of the axial response curves, as shown for one lenslet row in figure 3, are determined for the measurement of the focal length. The focal length variation of the whole array is shown in figure 4. A very smooth distribution is obtained. The discrete focal depth steps, resulting from the individual lenslets can be distinguished. The radius of curvature of the measured cylindrical focal length distribution fits well within the design value of $R = 20.0$ mm.

A distinct increase of the focal depth with the increase of the focal length is found in figure 3(*a*), as can be expected from the variation of the numerical aperture.

The lateral intensity distribution in the focal plane of a single lens was imaged onto a CCD chip using a 100× microscope objective (NA = 0.95). The image was stored on a PC with a framegrabber and is shown as an inset in figure 5(*a*). Figure 5(*a*) itself shows a line scan through the measured distribution (circles). These data values have been fitted with the theoretically expected sinc function (full curve), having its first minima at $x = \pm q$. In the diffraction-limited case, the spot size q for a quadratic aperture is given by $q = \lambda f / D$. This measurement has been repeated for different lenses in one row and the obtained spot sizes q are shown in figure 5(*b*) (circles). The comparison with the diffraction-limited values (full curve) proves the diffraction-limited performance over the whole parameter range.

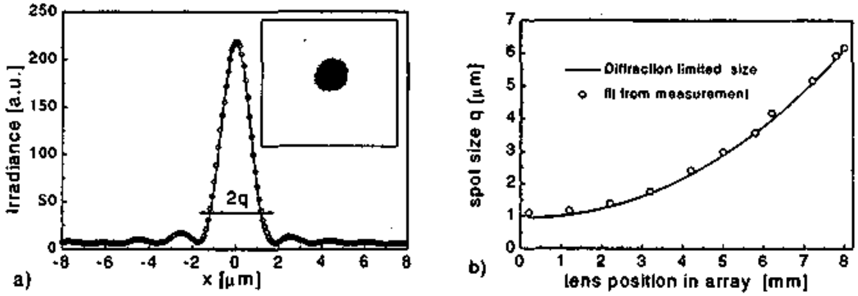

Figure 5. (*a*) Measured diffraction-limited PSF for a lens with $f = 542$ µm. The full curve shows the theoretical PSF and the circles denote the measurement. The inset shows the two-dimensional diffraction pattern in the focal plane, imaged onto the CCD. (*b*) Position q of the first minimum of the PSF for the different lenses in one row of the array.

5. Lens arrays for confocal microscopy on curved surfaces

As has been demonstrated previously [9], the use of microlens arrays with a constant focal length allows a parallel scanning technique in confocal microscopy. This results in an extended field size compared to a conventional confocal set-up using a single objective. The microlenses need to have a high numerical aperture and a symmetric on-axis intensity distribution in order to obtain the desired axial resolution. Lens arrays with continuous-relief diffractive lenslets, having an aperture of $150 \times 150\ \mu\mathrm{m}^2$, an NA of 0.28 and very low aberrations have been fabricated previously [3, 8] for confocal microscopy. The maximum object height variation to be measured with this kind of confocal microscope set-up is restricted to the focal length of the microlenses. Increasing the focal length of the lenslets will result in a decrease of either the axial or lateral resolution depending on whether the aperture or the numerical aperture are kept constant.

Lens arrays with spatially varying focal lengths are used on non-planar surfaces, the overall profile height of which exceeds the vertical measurement range of a microlens-array-based set-up, but is known to within a reasonable degree of accuracy. The lens array focal surface is shaped to fit the expected object shape. In the measurement, only the deviation of the object surface from the focal surface has to be detected, the maximum accessible profile depth is therefore considerably increased. Furthermore, it allows even faster measurements since the total vertical scan movement is reduced.

In the confocal condition, the light reflected from the object to be measured has to pass through the same microlens aperture on its way back to fulfil the measuring principle. This can be ensured by normal incidence of the light onto the curved surface. Arrays fulfilling this condition have been designed and fabricated for focusing onto a cylindrical ($R = 20$ mm) and a spherical surface ($R = 52.44$ mm) (see figure 2 and section 3 for the design algorithm). The normal incidence condition is fulfilled by a simultaneous variation

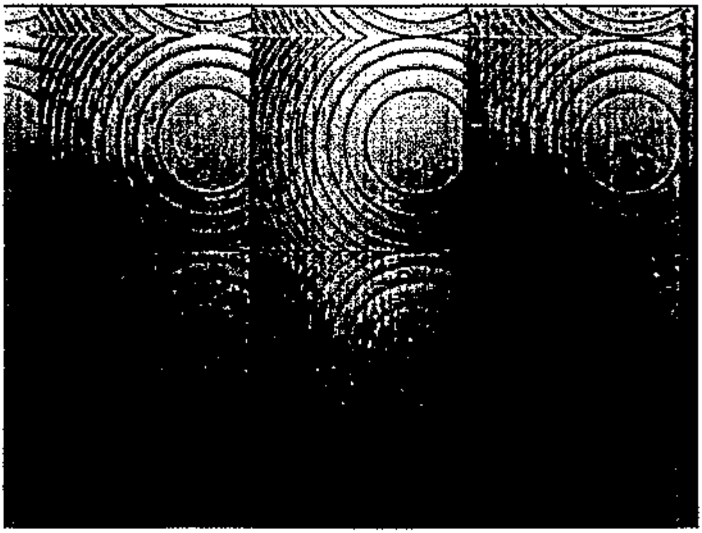

Figure 6. Optical microscope picture of a section of a lens array, focusing onto a sphere at normal incidence.

of the focal length and the beam deflection angle. Figure 6 shows an optical microscope picture of a small section of the off-axis lens array, focusing onto a spherical surface.

We present measurement results from the array with the spherical focal spot distribution. It consists of 60 × 60 lenses with a quadratic subaperture of $D = 200\ \mu\text{m}$ side length and a minimum focal length $f_0 = 400\ \mu\text{m}$. Adding the deflection function to the focusing function results in off-axis lenslets, having smaller grating periods than on-axis lenses with the same focal length and aperture. Therefore a phase-matching number of $M = 3$ was chosen for the whole array to reduce the spot size convolution effects in the laser writing process.

First results of confocal measurements of a spherical plano-convex lens, having a radius of curvature of $R = (52.44 \pm 1.0)$ mm are shown in figure 7. It shows the axial response of one row of the array. The flat horizontal line indicates the successful adaptation of the focal length distribution onto the measuring object shape. The peak intensity for the axial responses for the individual microlenses is nearly constant. This proves that the reflected light takes the correct path back through the same aperture, a consequence of the locally normal incidence onto the curved surface of the measured object. The additional curved line is due to additional foci, resulting from higher and lower diffraction orders. The topography obtained from the confocal measurement gives the difference between the focal spot distribution of the lens array and the object. For the plano-convex lens investigated, we found a residual deviation which lies within the manufacturing tolerances for this type of lens.

The axial resolution of the confocal measurements depends on the width of the axial response. This width does increase with decreasing numerical aperture as can be clearly seen in figures 3(*a*) and 7. Therefore, the vertical resolution varies with the lenslets numerical aperture over the array. If a constant vertical resolution is needed, constant numerical

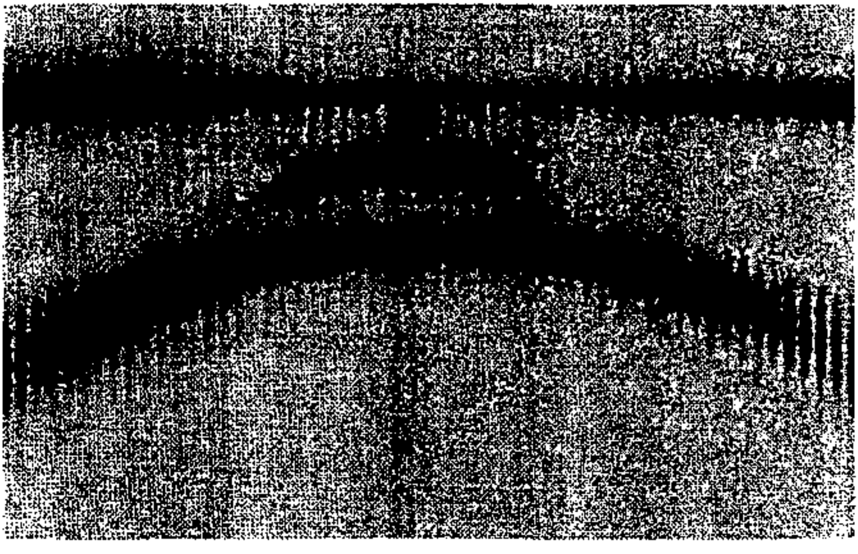

Figure 7. Axial response for one lenslet row at position $y = 0$ mm. The horizontal line indicates the successful focusing onto the measured spherical surface.
]

aperture lenslets are required, leading to larger lenses at the edges and therefore less dense packing. The choice to have a regular array of sampling points was made for convenience of data generation.

6. Conclusions

We have demonstrated optical systems that require or benefit from microlens arrays with spatially varying optical properties. When optical parameters such as focal length or deflection angle have to be varied over the individual array elements, the fabrication method has to fulfil several requirements. Direct laser beam writing has proven to be a flexible technology that guarantees high-accuracy fabrication of refractive as well as diffractive lenses covering a large parameter range on a single substrate. The variation of focal length alone and in combination with a varying deflection angle have been demonstrated for the application of confocal microscopy on curved surfaces. The confocal microscope has proven to be a very efficient tool for lens array characterization. A diffraction-limited imaging performance has been measured for elements with NAs ranging from 0.06 to 0.3 combined on one substrate.

The influence of small fabrication tolerances has been discussed with the example of confocal measurements on planar and curved surfaces.

Acknowledgments

The authors gratefully acknowledge the helpful discussions with R E Kunz and the contributions of H Schütz and H Teichmann of PSI in the development of the laser writing system. This work was supported in part by the Swiss Priority Programme OPTIQUE II.

References

[1] Völkel R, Nussbaum Ph, Herzig H P, Dändliker R and Hugle W B 1995 Microlens arrays for optical lithography *EOS Topical Meetings Digest Series* 5 100–5

[2] Gale M T 1997 Direct writing of continuous-relief elements *Micro-Optics—Elements, Systems, and Applications* ed H P Herzig (London: Taylor and Francis)

[3] Hessler Th, Gale M T, Rossi M and Kunz R E 1995 Fabrication of microlens arrays by direct writing in photoresist *EOS Topical Meetings Digest Series* 5 37–43

[4] Gale M T, Rossi M, Pedersen J and Schütz H 1994 Fabrication of continuous-relief micro-optical elements by direct laser writing in photoresist *Opt. Eng.* 33 3556–66

[5] Rossi M, Blough C G, Raguin D H, Popov E K and Maystre D 1996 Diffraction efficiency of high-NA continuous-relief diffractive lenses *Diffractive Optics and Micro-Optics* vol 5 (*OSA Technical Digest Series*) p 233

[6] Rossi M, Kunz R E, and Herzig H-P 1995 Refractive and diffractive properties of planar micro-optical elements *Appl. Opt.* 34 5996–6007

[7] Hessler Th and Kunz R E 1997 Relaxed fabrication tolerances for low Fresnel number lenses *J. Opt. Soc. Am.* A 14 1599–606

[8] Tiziani H J, Achi R, Krämer R N, Hessler Th, Gale M T, Rossi M and Kunz R E 1997 Microlens arrays for confocal microscopy *Opt. Laser Technol.* 29 85–91

[9] Tiziani H J and Uhde H M 1994 Three-dimensional analysis by a microlens-array confocal arrangement *Appl. Opt.* 33 567–72

Acknowledgments

This thesis was written during my employment as a research and teaching assistant and as Ph.D. student at the optics group of the Paul Scherrer Institute (PSI) in Zurich.

I would like to thank Prof. Dr. R. Dändliker, director of this thesis, for advising the thesis and for the helpful discussions.

Very special thanks belongs to my supervisors at PSI, Dr. R.E. Kunz and Dr. M. Rossi for introducing me into the field of diffractive optics. Their enthusiasm to discuss new ideas and their openness to share their profound knowledge was invaluable for my work.

My thanks belongs to Dr. K. Knop, who gave me the opportunity to join the applied solid state physics department of the PSI in Zurich. I'm very indebted to M.T. Gale, head of the optics group, who managed to ensure a lively and friendly atmosphere in the group.

I acknowledge PD Dr. H.P. Herzig for co-examining this thesis and the beneficial discussions we had. The discussions with him and all his colleagues of the micro-optics group at IMT Neuchâtel were very motivating and enjoyable. Particular thanks belongs here to Christoph Berger for the productive collaboration we had.

I would like to thank Prof. Dr. H. J. Tiziani from the Institute of Technical Optics (ITO) at Stuttgart University for accepting the co-referate of my thesis and for the fruitful collaboration on the microlens arrays for confocal microscopy. Special thanks belongs here to Michael Wegner, Daniela Steudle and René Achi from the ITO.

The colleagues at PSIZ deserve a special acknowledgment for the friendly and innovative atmosphere in the institute. The resulting work would not have been possible without the valuable support in fabrication and replication technology by Helmut Schütz, Richard Stutz, Susanne Westernhöfer and Jörn Pedersen. Jörn also was most helpful with his little and big programming hints. Thank you very much.
Also, all the other colleagues at PSI deserve great acknowledgment for creating and maintaining an atmosphere of innovation and for their helpfulness. Here, I would especially thank the other Ph.D. students and visiting guests at PSIZ, especially Dr. Claus Heine, Dr. Lothar U. Kempen, Dr. Jürg Dübendorfer and Dr. Fredrik Nikolajeff.

Not so obvious but very important was the support by my friends through the years and I would like to thank especially Dr. Frieder Mugele, Dr. Manfred Regula and Peter Pfahler for proofreading the manuscript.

Finally, I thank especially my parents who gave me all the necessary support during the years of study.

Thank you.